4

MINIMIZATION OF MECHANICAL ASPECTS OF FRICTION THROUGH SURFACE ENGINEERING

by

MOHSEN MOSLEH

B.S., Mechanical Engineering
Tehran Polytechnic
1986

M.S., Mechanical Engineering
Tehran Polytechnic
1988

Submitted to the Department of Mechanical Engineering
in Partial Fulfillment of the Requirements for the Degree of

DOCTOR OF PHILOSOPHY
IN MECHANICAL ENGINEERING

at the

MASSACHUSETTS INSTITUTE OF TECHNOLOGY

May 1994

Signature of Author ______________________________
Department of Mechanical Engineering
May 11, 1994

Certified by ______________________________
Professor Nam P. Suh
Ralph E. and Eloise F. Cross Professor and Department Head
Thesis Supervisor

Accepted by ______________________________
Professor Ain A. Sonin
Chairman, Department Graduate Committee

Minimization of Mechanical Aspects of Friction Through Surface Engineering

by

Mohsen Mosleh

Submitted to the Department of Mechanical Engineering May 11, 1994
in Partial Fulfillment of the Requirements for the Degree of
Doctor of Philosophy in Mechanical Engineering

Abstract

At present, mechanisms of friction in geometrically constrained sliding systems are poorly understood. It is hypothesized that in such systems the normal load increases due to the mechanical penetration of the surfaces by the entrapped wear particles which grow stronger through agglomeration. This phenomenon is accentuated in high vacuum and/or at high temperatures since wear particle agglomeration is augmented at the interface under a state of high compressive stresses. This hypothesis is tested by experiments on sliding contact mechanisms operating in the dry regime.

In this research, the role of wear particles in the dry friction of materials in the presence of geometrical constraints has been investigated. The increase in normal load as a result of wear particle entrapment at the interface is experimentally studied and its physical aspects are modeled. It has been shown that if the actual normal force is not considered, friction coefficients based on the externally imposed normal load is as high as 15 in a constrained system while its actual value, considering the increase in the normal load, is in fact less than one. The role of a high vacuum, high temperature environment in reducing the surface contamination and in promoting the consolidation of wear particles into an agglomerate is addressed. The surface engineering solution to achieve low friction is based on the idea of removal of wear particles from the interface soon after their formation. Undulated surfaces have been utilized toward this goal. Significant improvement in lowering the friction coefficient and in increasing the operating life of sliding bearings has been observed. Furthermore, these bearings satisfy the longer life and the high stiffness requirements of precision machine elements.

Finally, based on the identification of functional requirements of an ideal low friction surface, a model surface comprising a covalent solid coating on a smooth surface has been designed and developed. Experimental work conducted under an optimum normal load and coating thickness and with proper crosslinking density of the surface layer, has shown static friction coefficients of 0.025 and dynamic friction coefficients as low as 0.04 in dry sliding. Atomic force microscope examination of the surfaces has revealed that a low friction coefficient generally corresponds to least plastic damage to the surface layer. The application of such surfaces to practical sliding bearings has been experimentally examined and the impending problems are addressed.

Thesis Advisor: Professor Nam. P. Suh
Title: Ralph E. and Eloise F. Cross Professor of Manufacturing and
Head of the Department of Mechanical Engineering

Acknowledgments

Words cannot describe my heartfelt gratitude and respect for my advisor, Professor Nam P. Suh. He has given me a whole new perspective on life. A perspective which has provided me with self confidence, a willingness to learn, persistency in pursuit, and the desire to aim high. This is a perspective which was not shown to me through his lectures, but through his own actions. The values that he has instilled in me have had a tremendous impact on my life and I consider them to be the greatest gift of our relationship. I will certainly remember him throughout my entire life.

I would like to express my infinite gratitude to my thesis committee members. Of course, Professor Nam P. Suh, whose depth of knowledge in mechanics and manufacturing have had a profound impact on my doctoral research. He taught me how to start from basic scientific principals in order to solve real engineering problems. I am also indebted to Dr. Nannaji Saka, whose suggestions and critiques of my research were invaluable, especially for the many insightful discussions we had concerning the theoretical parts of my thesis. In addition, I would like to thank Professor Linn Hobbs for his comments on high temperature corrosion. And many thanks to Professor Alexander Slocum whose views on the application aspects of my research to precision engineering were very beneficial.

I would also like to thank other members of the faculty of the Mechanical Engineering Department whose lectures and discussions have been crucial to my work. Particularly, I would like to express my thanks to Professor Shahryar Motakef, who helped me tremendously, especially at the onset of my career. Many thanks go to Professors Rohan Abeyaratne, David Parks, and Lallit Anand for their time and comments on the modeling parts of my thesis. Professor Kamal Youcef-Toumi deserves a special thank you for all his advise and for offering me a teaching assistant position when my research fund was especially tight. I also owe many thanks to Professor Ernest Rabinowicz, who was always willing to listen to my problems and share his wisdom.

The sponsors of my research deserve a special thank you for making my work possible. I would like to thank Dr. Irving Stowers of the Lawrence Livermore National Laboratory who was always willing to provide me with the hardware needed for the high vacuum/ high temperature experiments. Thank you to Dr. Jorn Larsen-Basse of the National Science Foundation for his support of the ultra-low friction surfaces research. And finally, I would like to extend my thanks to the sponsors of the Brigham and Women's Hospital-MIT/Industry Consortium on Wear of Polyethylene. Particularly, my sincere gratitude to Dr. Myron Spector of the Harvard Medical School

A truly enjoyable part of my school life has been my friendship with students who came from a diverse mix of cultures and backgrounds. As each flower has its own unique smell, each friend has had his/her own special characteristics and I have learned from them all. I cannot name all of them, however, there are few that have to be mentioned. Dr. Farid Kaymaram, Dr. Hamid Salehizadeh, Dr. Ali Zolfaghari, Dr. Ali Kazeroonian and Babak Ayazifar have helped me whenever I have needed them. I have benefited from many wonderful discussions on various topics with Chahid Ghaddar, Haissam Haidar, Dr. Hisham Hasanein and Dr. Amr Mohamed. At the Laboratory for Manufacturing and Productivity, Dr. Turker Oktay, Dr. Dae Eun Kim, Dr. Chul Park, Dr. Sung Cha, Dr. Moshin Lee, Tae Kang, Phillip Howard, Ravi Patil, Derrick Tate, Daniel Walczyk, Heather Cole and Jorge Arinez have always been good friends. Many special thanks go to Jorge who spent much of his own time editing my thesis. I wish them all good luck.

I would also like to thank the technical and administrative staff at the Institute. Particularly, Fred Cote, Kevin Baron, Victor Lerman, and Gerry Wentworth whose technical assistance was greatly appreciated. To Fred, I owe an enormous debt for his patience teaching me machining skills necessary to make the hardware for my research. I am also grateful to Mike Frongillo of the Scanning Electron Microscopy Center for his instructions and to Elizabeth Shaw of the Atomic Force Microscopy Center for putting up with me. I am also indebted to Sally Stiffler, Kathy Larson and Dorothy Cavignano at the Laboratory for Manufacturing and Productivity as well as Doris Elsemiller, Ann Seman, Maggie Beucler, Joan Kravit, Susan Melillo, and Leslie Regan at the Mechanical Engineering Department for their administrative assistance over the past few years. To Leslie, I offer special thanks for all her kindness and her invaluable advise on many academic issues.

Lastly, I wish to thank my parents. I cannot thank them enough for raising me the way they did. They have trusted me all my life and have given me a freedom to make my own choices. I owe all my success to them. I thank them for their prayers. I am also indebted to my sister, Maryam, for her support and encouragement throughout my college education.

Table of Contents

List of Figures

List of Tables

Chapter 1

Introduction and Scope of Thesis

1.1 General Introduction

Man has always challenged nature as he wishes to minimize the energy dissipation in machines. Energy dissipation is the natural manifestation of the destructive interaction of different systems. One interaction is the one that occurs at the interface between two or more bodies in relative motion. Friction and wear of sliding elements are the visible consequences of the interfacial interaction and are not desirable in many applications. On the other hand, to escape from an undesired phenomenon forced by the nature is to find a design solution to go around the problem. This requires a fundamental understanding of the causes of the undesired phenomenon, innovation and creativity. Therefore, to control both friction and wear requires knowledge of surface interactions, knowledge of materials, and innovative designs.

Throughout history our understanding of interface phenomena during sliding has been improved empirically and theoretically. Early improvements were made through the trial and error. As the scientific approach toward the understanding of all phenomena began to be applied, it allowed scientists and engineers to see the interface interactions from a new perspective. Today, the interfacial interactions of surfaces during sliding and its consequences are treated in a multidisciplinary field of tribology. Tribology benefits from the advancements in many other branches of science and technology such as, mechanics of solids, materials, fluids, physics, and chemistry. However, many models and theories in tribology have dealt with tribological phenomena from a limited perspective. This narrow focus can be attributed to the high degree of complexity of tribological problems which ideally should be approached with a sound and thorough knowledge of surfaces before, during, and after contact. A knowledge which must be applied at the atomic, micro, and macroscopic levels.

The current understanding of friction, however, lacks a fundamental relationship between the known behavior at each of these three levels.

The study of surfaces before contact is relatively new and has raised many questions for tribologists. For example, given a certain material what is the optimum surface to achieve low friction? Or, given a certain surface what is the optimum material to achieve low friction? The study of surfaces during and after contact, however has been done for many years with friction tests, followed by examination of surfaces using light, scanning electron, atomic force and tunneling electron microscopes.

Based on the current understanding of tribology, friction mechanisms can be divided into two main categories. The first category includes mechanisms mechanical in nature and involves plastic deformation both at the surface and in the bulk. The second category includes chemical mechanisms and is commonly referred to as adhesion. Although these two mechanism may always co-exist, a fundamental question is to identify the role of each when one is minimized with respect to the other.

This goal of this thesis is to investigate the contribution of mechanical mechanisms to friction. The mechanical interactions can be the dominant contributors to friction in geometrically constrained sliding systems, especially in high vacuum and/or high temperature. Furthermore, based on the identification of functional requirements of an ideal surface, the contribution of mechanical interactions to friction can be indeed minimized leading to ultra low friction in dry sliding.

1.2 Goal of the Research

Although the importance of mechanical aspects of friction in tribology has received much attention, the geometrical and environmental effects have not been well investigated. Mechanical interactions at the interface manifest themselves in different forms depending on the sliding situations. Plowing by wear particles is an important form of the interactions at the macroscopic scale. It is a topic that has been the focus of much research which has helped the understanding of wear particle formation and the relationship between particle size and the friction coefficient and wear rate. Wear particle agglomeration in unconstrained sliding systems also has been studied and theoretical modeling as well as experimental evidence have been investigated in the past. In this thesis, the geometrical effects on the plowing component of friction, a key factor in the frictional behavior of geometrically constrained sliding systems compared to the unconstrained ones, is addressed.

When the geometrical constraints are combined with the environments in which adhesion augments the mechanical interactions, a severe sliding situation arises leading to seizure and extensive damage to the surfaces. High vacuum, high temperature is an environment in which dry sliding is unavoidable and therefore, the operating life of sliding contact bearings is short. The topographical design of sliding surfaces has been used to control friction and to increase the life.

Finally, in a systematic approach, the functional requirements for an ideal surface are identified and a surface model to satisfy such requirements has been developed. Friction coefficients as low as 0.04 with minimum damage to the interface is achieved. The outcome of this research is hoped to serve as a base for the development of long lasting surfaces without plastic deformation and with ultra-low friction coefficients.

1.3 Thesis Overview

Following this introductory chapter, the mechanisms of friction in dry sliding will be presented in Chapter 2. The chapter will serve to clarify the importance of mechanical components of friction. In particular, the role of wear particles in unconstrained will be reviewed. A friction model to explain the increase of the normal load due to the wear particle entrapment at the interface of geometrically constrained systems will be presented. This model demonstrates the strong dependence of the frictional resistance of such systems to the number and size of the entrapped wear particles.

In Chapter 3 the important role of plowing and agglomeration in the geometrically constrained sliding systems in the dry sliding regime will be experimentally investigated. The variation of normal load as a result wear particle entrapment at the interface will be experimentally verified and a model for two-point contact seizure will be presented. This chapter emphasizes that the increase in the frictional resistance of such systems is not due to the increase in the friction coefficient but instead is caused by an increase in the normal load. The removal of wear particles from the interface will be shown to make the friction of such sliding systems insensitive to the geometrical constraints.

Environmental dependence of mechanical mechanisms of friction is the main issue addressed in Chapter 4. In particular, the high vacuum and/or high temperature sliding requires the design of new bearing surfaces to compensate for the lack of a lubricant due to the unacceptability of the airborne contamination or due to a high operating temperature. Also included in Chapter 4, is a brief discussion on the augmentation of mechanical components of friction by higher adhesion due to the slow rate of oxidation in vacuum and thermal softening of materials at higher temperatures. Undulated surfaces will be employed in an attempt to develop a sliding bearing which can operate in such environments with a low friction coefficient and a long life.

Chapter 5 describes a systematic approach to design and development of covalent solids which can undergo large elastic deformations at the surface due to their high elasticity while the normal load is supported by their hard substrates. Such solids comprising a covalent solid coating on a smooth and hard surface only form secondary bonds with the counterface owing to the directional characteristics of their structural. Also a surface roughness of tens of angstroms is shown to minimize the asperity deformation component of friction; thus reducing friction coefficients by one order of magnitude compared to that of the boundary lubricated sliding. An emphasis is made to correlate the magnitude of the friction coefficients with the atomic force microscope images of the tested surfaces. A general conclusion is that a low friction coefficient corresponds to least plastic deformation of the surface layer. Furthermore, the optimum crosslinking density of the surface layer has been shown to provide the minimum friction coefficient for a certain load and surface layer thickness.

Finally, the application of low friction surfaces to the simple practical sliding bearings is studied in Chapter 6. The importance of the surface roughness of the counterface is stressed and the experimental results are provided. Also the durability of the surface film and the factors affecting it are briefly addressed.

The final results of this work along with the recommendations for future research are presented in Chapter 7 and conclude this thesis.

Chapter 2

Mechanical Aspects of Friction

2.1 Introduction

The phenomenon of friction has been investigated by numerous scientists and engineers, for it represents an attribute of matter which affects the operation of engineering systems. Compared with how long man has had to deal with friction phenomena, the scientific approach has only been recently applied towards better understanding the nature of friction and placing it on solid scientific grounds. The early practical applications of friction such as the rubbing of sticks together to kindle a flame by frictional heat generation, the use of the wheel, and the utilization of fatty acid-based lubricants date back thousands of years. These simple, yet effective methods of controlling friction between two solid surfaces were developed based on purely empirical observations and trial and error over centuries. As in all branches of science, these early observations laid the foundation for a scientific and systematic approach to analyzing the interactions of surfaces in contact. A fundamental understanding of the underlying causes of friction between two bodies in contact based on a systematic approach can obviously aid both designers and engineers in their desire to control friction.

The discovery of some of the basic laws of friction, such as the proportionality between the normal and limiting friction forces and the independence of friction force from the apparent area of contact, goes back to the observations made by Leonardo da Vinici [1,2] in the fifteenth century. Amonton and Coulomb[3] verified the same laws and hypothesized that the friction force of surfaces in contact is due to the resistance of asperities of surfaces in contact as they pass over one another. In this manner they were able to explain why the friction force is independent of the nominal contact area as well as the proportionality of normal and frictional forces. Early in the beginning of the twentieth century the adhesion theory of friction was introduced by Tomlinson [4] and was further developed by Bowden and Tabor [5]. The theory suggests that strong adhesive junctions are formed when two solids come into contact. The force required to shear the weaker material at those junctions is then the friction force which must be overcome to produce relative motion.

Since its introduction, the adhesion theory of friction has become the dominant picture of the friction mechanism in the minds of researchers. The theory has been modified to include such phenomena as surface energy and chemical compatibility of materials [6,7], the interdiffusion of atoms and molecules [8], and electromechanical and electromagnetic theories [9]. These modifications are mainly proposed to explain questions such as, why the friction coefficient predicted by the adhesion theory is much less than that observed in many experiments, or how the secondary bonds that form at a junction can be stronger than the shear strength of the softer material. Although these theories have advanced the understanding of adhesion phenomenon, they have neglected the contribution of other friction mechanisms.

In a more complete model, the friction force is attributed to the combined contribution of mechanical interactions such as, plowing and asperity deformation, as well as the contribution of adhesion. Shaw and Macks [10] proposed such an idea and expressed the friction coefficient as the sum of the two components which are individually predicted. One is due to the adhesion and roughness theories and another component is due to plowing by hard asperities. This model, though more complete, cannot describe the variation of friction coefficient in a particular sliding system with respect to time. Another theory of friction which explained the phenomenological sequence of friction in a more detailed manner was proposed by Suh and Sin [11] and called ɘfriction space . In the following sections this idea will be discussed and the controllability of friction in the light of the friction space concept will be addressed.

2.2 Friction Space

The friction space is a geometric illustration of the friction coefficient as a function of three mechanism: asperity deformation, plowing by hard asperities and/or wear particles, and adhesion. The total friction coefficient is the weighted sum of these three components, depending on the local friction condition that prevails at the sliding interface, i.e.

$$\mu = f_d\mu_d + f_p\mu_p + f_a\mu_a \tag{2.1}$$

where f_d, f_p and f_a are the weighting factors, which may vary as a function of time, and μ_d, μ_p and μ_a are the deformation, plowing and adhesion components of the friction coefficient, respectively. The concept is illustrated in Figure 2.1 in which the friction coefficients expressed in terms of the normalized interfacial shear strength, f , the slope of the surface asperities, θ , and the ratio of the width of wear particle penetration into the softer material to twice its radius, $w/2r$. The normalized interfacial shear strength is defined as the ratio of the shear stress at the interface to the shear flow stress of the softer material.

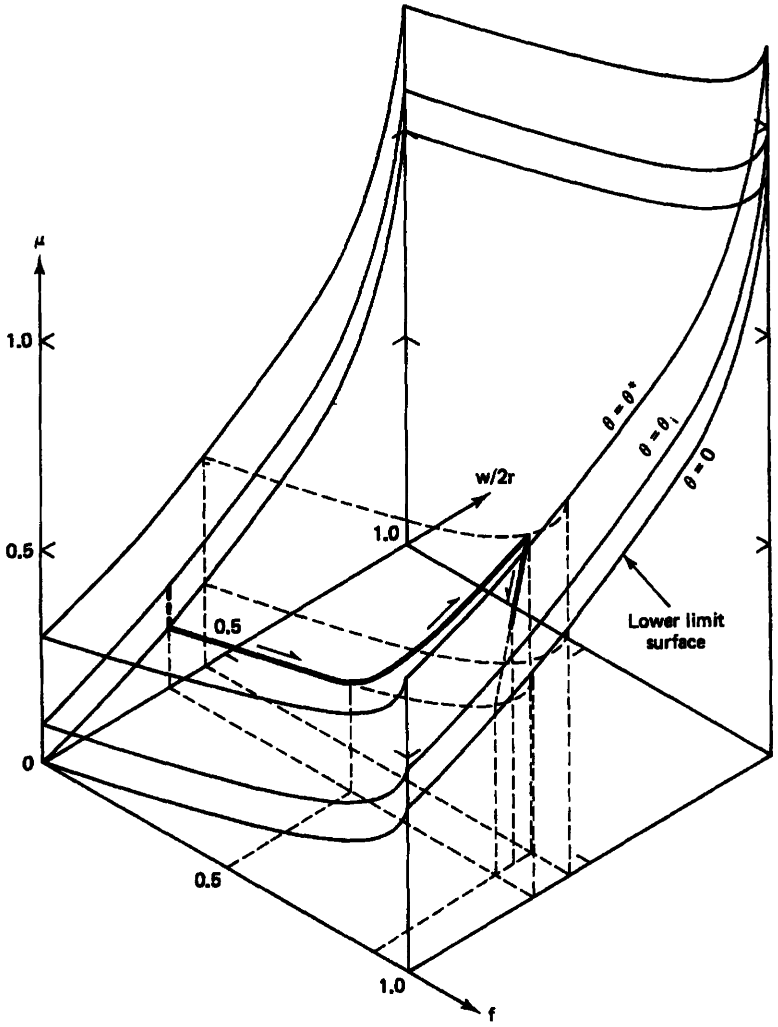

Figure 2.1 Friction space: a geometrical illustration of the friction coefficient as a function of surface roughness, wear particle penetration, and adhesion [12].

The frictional state of a typical engineering sliding pair defines a plane in the friction space. This plane in turn represents the asperity slope of the surfaces in contact and can move up from a lower bound where the asperity slope is zero ($\theta = 0$). Generally, the θ_i surface in the friction space can be referred to as the friction when it is affected by the initial roughness of the surfaces. At the steady state of sliding, however the roughness has changed and the θ^* surface correspond to that stage of sliding.

One of the frictional phenomenon which is commonly observed in sliding of metals is the transition from low friction coefficient values of about 0.2-0.25 to high values of about 0.6-0.8. This phenomenon can be well explained qualitatively with the friction space concept and is addressed in detail in reference [12]. At the onset of sliding, friction is mainly due to the deformation of the surface asperities. The adhesion and plowing components are negligible due to the contamination of surfaces in contact and the absence of wear particles. As sliding progresses, wear particles are produced and uncontaminated surfaces are exposed. Small wear particles begin to plow the interface and the friction coefficient increases. The increase in friction coefficient will continue due to the increase in both the number of entrapped wear particles as well as their size. The friction coefficient then reaches a steady state at which the number of newly formed wear particles at the interface is equal to the number of particles leaving it. The increase in the adhesion of freshly exposed surfaces will also tend to increase the size of wear particles at the steady state which in turn increases friction.

The frictional energy loss in a sliding system occurs either at the surface or in the bulk. The magnitudes of the three components of friction (i.e., asperity deformation, adhesion, and plowing by hard asperities and/or wear particles) indicate the severity of the destruction of the surfaces as well as the boundary conditions for the mode of deformation in the subsurface. The subsurface deformation, which is one of the sinks that dissipate energy in a sliding system, can be elastic, plastic or viscoelastic or the combination of each. In this sense, the hysteresis losses or the energy losses due to intensive plastic deformation such as crack propagation in the subsurface in some sliding situations are not independent friction mechanisms. Those energy loss mechanisms are dependent on the surface boundary conditions governed by the normal load and friction coefficient components.

2.3 Controllability of Friction Through Surface Engineering

It has been very common in the tribology field to suggest new materials or new lubricants to reduce friction and wear when low friction or wear has been desired. The idea behind this approach is that the experienced friction coefficients are material properties and can only be changed to desired level through the choice of material. However, it is not difficult to conclude from the friction space concept that the friction can indeed be controlled through the design of surfaces as well as the choice of materials. For example, based on the concept, the same materials with and without the existence of wear particles at the interface will have different frictional behavior. Also, smaller or larger penetration of wear particles into the interface for the same material provide different friction coefficients. The surface characteristics such as surface roughness and waviness can also determine the state of friction for a sliding systems. These issues can provide a means to control the friction by designing new surfaces and achieving the goal of low friction for engineering applications even without modifying the materials [13,14].

In addition, the strength of interfacial bonds between the surfaces in contact at the asperity level can also be controlled through the design of the texture and structure of the surface layer. The ideal situation is to provide surfaces which can only make secondary bonds such as Van der Waal s bonds to the atoms of the opposite surfaces. Then the breakage energy of such bonds is shown to be small and provides low friction.

2.4 Importance of Mechanical Components of Friction

It is important for a surface engineer to identify the dominant mechanisms of friction in a particular sliding system and find the solution or solutions to minimize such components. While most researchers in the tribology field were guided by the notion that friction is caused by adhesion, Suh et al. [12] showed that for most engineering applications, the contribution of mechanical components has been underestimated. In particular, the experimental investigation of the role of wear particles in dry sliding and boundary lubrication revealed that the friction coefficient can be decreased if wear particles are not present at the interface.

The plowing component of friction, either with full contact as in dry sliding or with partial contact as in boundary lubrication, is present in almost every sliding system. This component is a manifestation of a general irreversible mechanism of energy dissipation in friction, i.e. plastic deformation. The occurrence of plastic deformation either at the surface or in the substrate, using the existing materials and the surfaces seems to be unavoidable [15]. In the following sections such mechanical components will be described, and the solutions obtained in this research will briefly be presented.

2.5 Mechanical Interlocking of Asperities and Asperity Deformation

One of the earliest theories to explain the interaction of sliding surfaces was the roughness theory of friction. Based on this model, the surfaces of materials in contact, which consist of asperities at a microscopic level, interlock with each other and exhibit resistance to motion. Therefore a tangential force is required for the asperity of one surface to pass up and over the corresponding asperity with a slope of θ on the opposite surface. Assuming that all or majority of asperities have the same slope θ, the friction coefficient is given by

$$\mu = \tan\theta \tag{2.2}$$

The angle θ in this model is taken as a constant, and also the sliding up action is assumed to continue throughout sliding. These two assumptions, however, are not valid because of the plastic deformation of the asperities (Figure 2.2) and the kinematical constraints on the sliding surfaces. The plastic deformation of asperities under shear and compressive stress was first studied by Green [16] using a slip line analysis. Challen et al. [17] applied the slip line analysis to the situation in which a rigid surface slides over a soft material with an elastic-perfect plastic behavior. However, in both models the friction coefficient depends on the adhesion between the contacting surfaces of the asperities and is not merely a result of the kinematical constraints of the sliding surfaces. In a model similar to that of Green s, Suh and Sin [11] showed that the asperity deformation can be analyzed by kinematic considerations regardless of the nature of the bonding between the contacting asperities. The corresponding friction coefficient ranges from a minimum value of 0.39 to a maximum of 1.

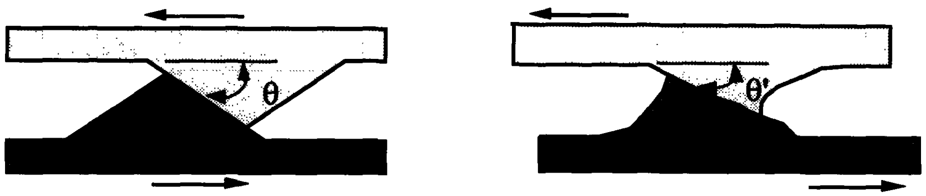

(a) (b)

Figure 2.2 Asperity deformation showing a decrease in the initial slope of the asperity θ (a) to a smaller slop of θ (b).

2.6 Plowing By Hard Asperities and/or Wear Particles

An examination of almost all surfaces after dry or boundary lubricated sliding shows plowing grooves on the sliding surfaces. The plowing of the interface can originate from two sources. First, the hard asperities of one of the sliding surfaces penetrate into the other surface and therefore cause plowing of the softer material. Second, wear particles at the interface penetrate into one or both surfaces and produce plowing grooves. The analysis of plowing by hard asperities with a spherical or a cylindrical shape was first performed by Bowden [18]. It was found that the plowing component based on a simple model could be about one third of the total friction coefficient. Other shapes for the asperities such as cones, pyramids have also been investigated and similar expressions have been obtained [19]. The experimental results of many researchers are in good agreement with the predictions of such models.

Despite the attention that has been paid to the mechanism of plowing by hard asperities, Suh et al. [11] showed that plowing by wear particles is the dominant mechanism of friction in typical engineering surfaces. Wear particles in a sliding system are originally generated through asperity deformation, and plowing by hard asperities. Small wear particles then are compacted at the interface and form larger wear particles which severely plow the interface.

The analysis of plowing by wear particles was performed for different shapes of particles. For a spherical wear particle, the effect of plowing by wear particles on friction was found to be very sensitive to the ratio of the penetration width to the diameter of the wear particle (Figure 2.3). The friction coefficient was found to be [11]:

$$\mu = \frac{2}{\pi}\left(\frac{2r}{w}\right)^2\left\{\sin^{-1}\frac{w}{2r} - \frac{w}{2r}\left[1-\left(\frac{w}{2r}\right)^2\right]^{1/2}\right\} + \frac{2}{\pi}\left(\frac{2r}{w}\right)^2\frac{1}{3}\frac{s}{s_m}\left\{1-\left[1-\left(\frac{w}{2r}\right)^2\right]^{1/2}\right\} \quad (2.3)$$

where s and s_m are the shear strength of the interface and of the softer material, respectively. Also w is the width of the penetration of particles, and r is the radius of particles. The maximum friction coefficient occurs when the ratio of penetration width to the particle diameter is equal to one. Also, as the ratio of the shear strength of the interface to the shear strength of the bulk increases so does the friction coefficient.

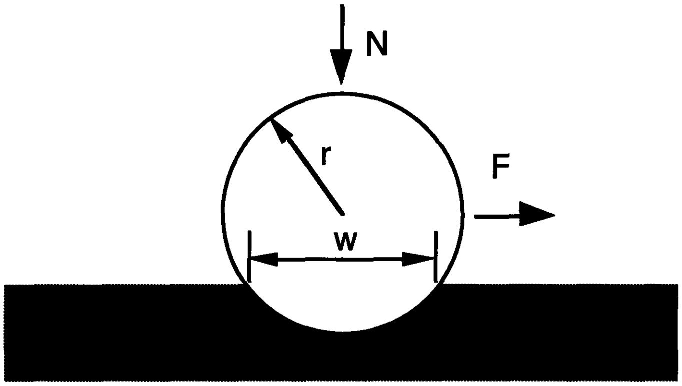

Figure 2.3 A spherical wear particle with a radius of r and a penetration width of w plowing the softer surface.

2.7 Generation of Large Wear Particles

Much has been published on how wear particle formation occurs. Many researchers have described the process using the theory of adhesion which is based on the formation and subsequent fracture of the junctions at the interface. Among these are the Prow formation model [20], shearing off model [21], and the film transfer model [22]. Similarly, the abrasion of surfaces by the hard asperities also has been extensively addressed by many investigators. The process of abrasion is based on the plowing and microcutting of the softer surface by the hard asperities of the counterface.

The fact that the surface of most materials are covered by contamination such as physisorded and/or chemisorbed layers reduce the possibility of the formation of adhesive junctions at the onset of sliding. In addition, the formation of submicron wear particles in boundary lubricated sliding in which such adhesive junctions can hardly form justifies the mechanical nature of the wear particle generation process [23,24]. Therefore the formation of submicron to a few micron-sized wear particles during the running-in stage of sliding must be due to asperity deformation and plowing by the hard asperities. As sliding proceeds, the formation of larger wear particles is more likely due to the agglomeration and delamination as will be described next.

2.7.1 Agglomeration of wear debris

Often in dry sliding of metals wear particles as large as tens of micrometers has been observed in the steady state. The micrographs of the sliding interface of a variety of metallic pairs rubbing against each other showed that the entrapped particles at the interface have an agglomerate structure [25]. This observation along with the measurement of separation distance between the pin and the disks in the same experiments led to the conclusion that larger wear particles in the range of a few micrometers to a few tens of micrometers can be formed through the agglomeration of smaller particles.

The agglomeration of wear particles produces larger wear particles which are entrapped at the interface and amplify the plowing component of friction. The separation of sliding surfaces caused by agglomeration is naturally allowed in an unconstrained system and therefore the normal load will remain constant and the increase in the frictional force will be due to the more severe plowing compared with the case in which smaller particles are present at the interface.

When a sliding system is constrained, the agglomeration will cause a sharp increase in the normal load which in turn results in higher frictional resistance of the surface to motion. This case will be studied in detail in the next sections and experimental results will be provided in the next chapter.

2.7.2 Delamination of Large Wear Sheets

Friction phenomenon involves a cyclic loading of the surface layer in almost all sliding systems. This cyclic nature of loading promotes the cyclic deformation of the surface layer as a result of the moving of asperities of one surface over the asperities of another. One of the recent theories of wear which was introduced by Suh [26] to account for the formation of particles as a result of such cyclic loading is the delamination theory of wear. The cyclic deformation of the surface layer, based on this theory, causes cracks to nucleate at a certain depth below the surface. Crack nucleation at the surface is not favored because the large hydrostatic pressure at the contact region suppresses void formation. The pre-existing or newly-nucleated cracks are then propagated parallel to the surface under cyclic loading and join neighboring cracks. Long, thin wear sheets delaminate when these cracks propagate to the surface through weak points in the material.

The size of wear particles generated through delamination depends on the normal load and the friction coefficient [27]. Wear sheets as small as a few micrometers and as large as a few hundred micrometers can be produced through this wear mechanism [28].

2.8 Agglomeration of Wear Particles in Geometrically Constrained Systems

The wear particle agglomerate can be assumed to be a cylinder with a hemispherical tip which plows the softer surface. As the sliding proceeds, new particles will form as a result of plowing and asperity deformation or delamination. The newly formed particles are assumed to attach to the agglomerate and cause it to grow. This assumption is based on the fact that the real contact area is the sum of some very small regions on the hemispherical tip of the agglomerate. Therefore, as the softer material is wearing away in some areas, the material agglomerates in the others. The agglomeration growth due to sliding, an amount dx, is schematically shown in Figure 2.4 in which the constraint on the vertical motion of agglomerate is shown by a spring. It will be assumed that the wear rate will not be affected by the increase in the normal load due to the geometrical constraints. The increase in the volume of wear generated due to sliding an amount of dx is given by

$$\frac{dV}{dx} = K\frac{N_0}{H} \tag{2.4}$$

where K is the wear coefficient, H is the hardness of the material being plowed and N_0 is the initial normal load. The effect of variation of the normal load will be neglected in this analysis.

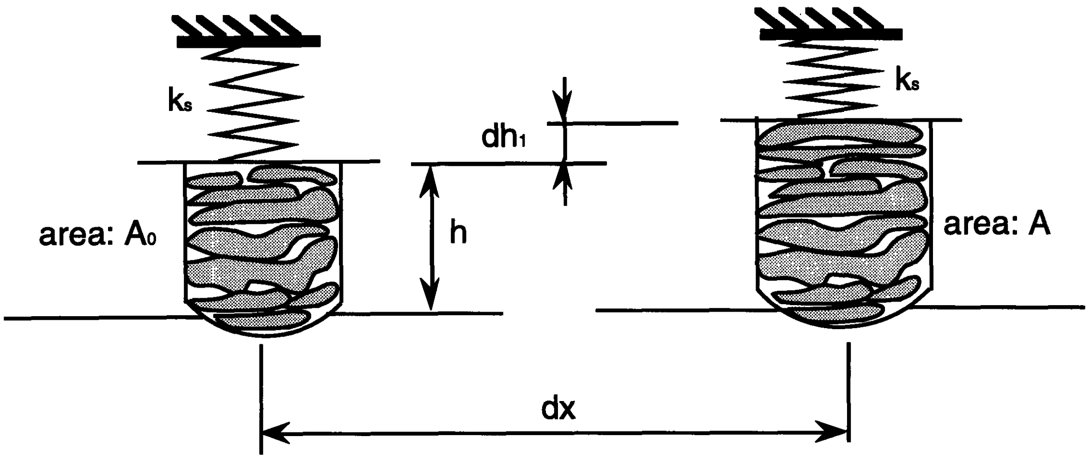

Figure 2.4 A cylindrical wear particle agglomerate with a hemispherical tip plowing the softer material in a constrained system with a stiffness of k_s.

Now suppose that the constraint on the agglomerate is removed. The increase in the height of the agglomerate dh, can be related to the variables in the wear equation.

$$\frac{dh}{dx} = K\frac{N_0}{HA_0} \tag{2.5}$$

where A_0 is the initial area of the agglomerate which is assumed to remain unchanged when there is no constraint on the system. The force which is needed to elastically compress the agglomerate an amount dh_2 can be calculated from the elastic axial deformation of a beam (Figure 2.5). This yields

$$\frac{dh_2/dx}{dh_1/dx} = \frac{k_s h}{EA} \tag{2.6}$$

where A is the true area of the agglomerate, which changes with respect to the sliding distance, h is the height of the agglomerate and k_s is the spring constant. In addition from the geometry shown in figure 2.5 one can write

$$\frac{dh}{dx} = \frac{dh_1}{dx} + \frac{dh_2}{dx} \tag{2.7}$$

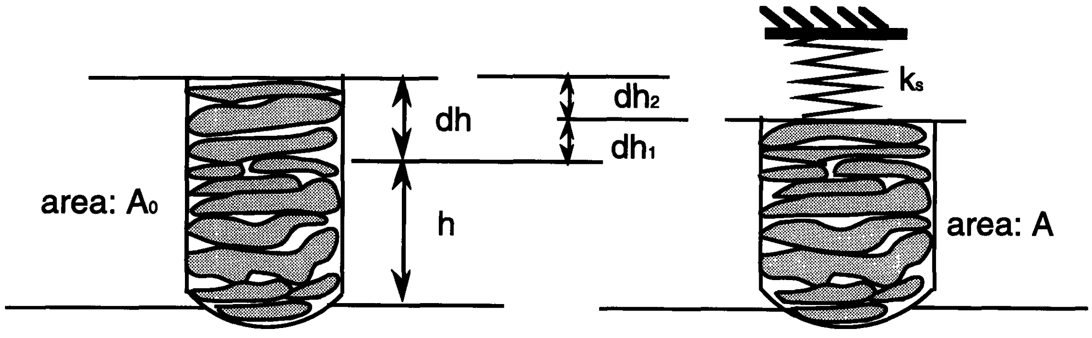

(a) (b)

Figure 2.5 Global elastic compression of the agglomerate by the geometrical constraint modeled as a spring.

Using eqs. (2.5-2.7) the expression for the normal load as a function of the distance slid is

$$N(x) = N_0 + \frac{Kk_sN_0}{A_0}\int_0^{x_f} \frac{EA}{(EA + k_sh)H}dx \tag{2.8}$$

The above analysis is based on an elastic compressive deformation of the agglomerate under the normal load. This limits the amount of deformation in the system to a certain value. Although it is true that the agglomerate will undergo plastic deformation, this is only valid for the very last cycles of seizure in geometrically constrained systems. As the experimental results on the seizure of such systems will be presented in the following chapters, the sharp increases in the frictional torque of sliding contact bearing can be related to this phenomenon. There are two limiting cases for the above analysis.

Case 1

The stiffness of the spring is zero. This is the situation for an open sliding system in which the slider is allowed to move up to accommodate the agglomeration of wear particles. Almost all pin-on-disk experiments can be categorized as open sliding systems because of the unconstrained motion of the pin in the direction of agglomeration. In this case from eq. (2.8) one can find that the normal load will not increase as the sliding proceeds. Also from eq(2.5), the agglomeration rate with respect to time is

$$\overset{\circ}{h} = K \frac{N_0}{HA_0} \overset{\circ}{x} \tag{2.9}$$

The agglomerate, however cannot grow indefinitely and will reach a maximum size after which it will break off. The maximum height of the agglomerate ($h_{\max}$) depends on the normal load and the friction coefficient. The distance at which the agglomerate reaches to its maximum height then can be found as

$$x_f = \frac{HA_0}{KN_0} h_{\max} \tag{2.10}$$

This distance was also determined for unconstrained sliding systems based on a cutting model in which the hemispherical tip of the agglomerate with a radius of r penetrates into the softer material with a penetration width of w [25]. The agglomeration rate and the distance slid required for the agglomerate to reach its height were given as:

$$\overset{\circ}{h} = \frac{\overset{\circ}{x}}{\pi}\left[\arcsin\left(\frac{w}{2r}\right) - \left(\frac{w}{2r}\right)\right] \tag{2.11}$$

$$x_f = \frac{\pi h_{\max}}{\left[\arcsin\left(\frac{w}{2r}\right) - \left(\frac{w}{2r}\right)\right]} \tag{2.12}$$

Case 2

The spring has an infinite stiffness. In this case, if the maximum height of the agglomerate before the break is greater than the gap in the system, the normal load will increase and by using eq. (2.8) the following expression can be determined for the normal load.

$$N(x) = N_0 + \frac{KN_0}{A_0 h_0} \int_0^{x_f} \frac{EA}{H} dx \tag{2.13}$$

2.9 Influence of Wear Particle Agglomeration on Friction

a) Unconstrained Sliding Systems

A consequence of wear particle agglomeration is the decrease in the number of wear particles which carry the normal load. This decrease is the result of formation of larger wear particles. Figure 2.6 shows two sliding systems with the same normal load but different size wear particles. The ratio of the width of indentation to the diameter of wear particle was given as [25]:

$$\frac{w}{2r} = \sqrt{2/\pi}\left(\frac{N}{Hr^2}\right)^{½} n^{-½} \tag{2.14}$$

where n is the number of wear particles which are all assumed to have the same size. It can be concluded from eq. (2.14) that as the number of wear particles decreases the ratio of the width of penetration of particles to their diameter decreases which in turn results in a lower friction coefficient as can be seen from eq. (2.3). This conclusion was found to be in agreement with the experimental results.

The above conclusion may be derived if the conservation of mass between the two systems is applied. From conservation of volume, assuming a constant density, the relation between the radius of a n-wear particle system and a single-wear particle system can be written as:

$$r = \left(\frac{3V}{4\pi}\right)^{⅓} n^{-⅓} \tag{2.15}$$

where V is the total volume of wear particles at the interface. Therefore, the relation between the ratio of penetration width to the wear particle diameter and the number of wear particles at the interface is:

$$\frac{w}{2r} = \sqrt{2/\pi}\left(\frac{N}{H}\right)^{½}\left(\frac{3V}{4\pi}\right)^{-⅓} n^{-⅙} \tag{2.16}$$

which suggests that as the number of wear particles increases, i.e. smaller particles at the interface, the penetration width to diameter ratio decreases which in turn results in lower friction coefficient. One the other hand, large wear particle agglomerates will have a higher ratio of penetration width to the particle diameter which results in higher friction coefficient.

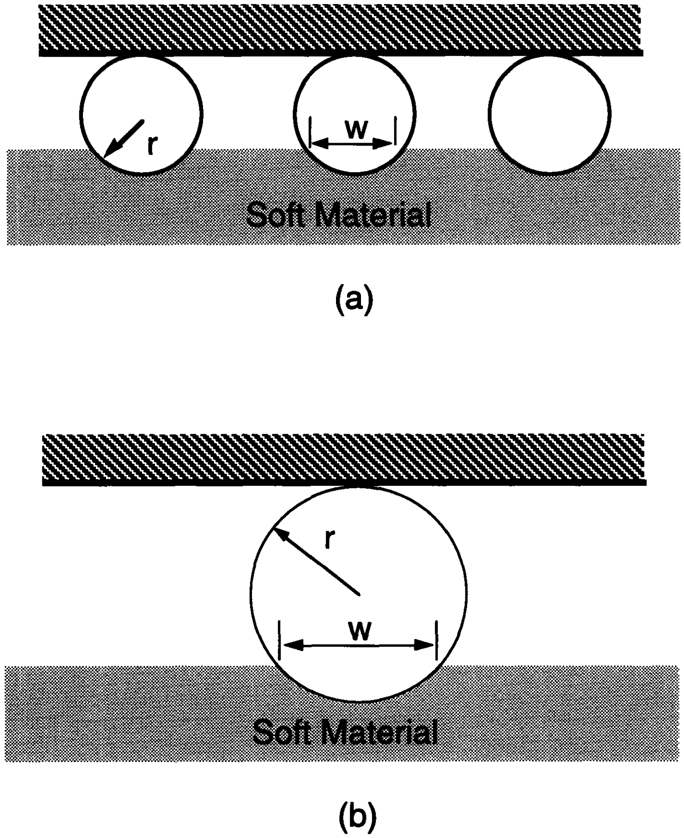

Figure 2.6 Plowing by wear particles in a sliding system consisting of "n" number of spherical particles (a) and one single spherical particle of the same volume.

b) Constrained Sliding Systems

When there is a constraint in a sliding system normal to the sliding direction the normal force will increase as a function of sliding distance. For instance, consider a simple sliding bearing in which a rod is rotating inside a bushing. Wear particle agglomeration can occur in different locations at the same time. This multi-contact situation is shown in Figure 2.7. At each contact point the growth of the particle is constrained by the system and as a result the normal force will increase as sliding proceeds.

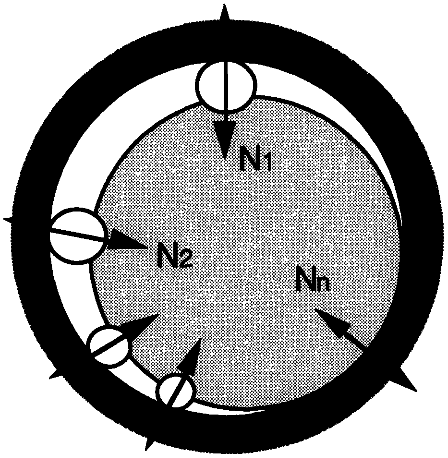

Figure 2.7 Compressive normal forces developed at the multi-point agglomeration locations in a geometrically constrained system

The analysis of such problems is complicated by the random nature of agglomeration in various locations around the circumference. However, it is easy to show that the frictional torque τ will indeed increase as:

$$\tau = R(\mu_1 N_1 + \mu_2 N_2 + \cdots + \mu_n N_n) \qquad (2.17)$$

where N_i and μ_i are the normal force and the friction coefficient at each agglomeration location and R is the radius of the shaft. A two-point contact model will be presented in chapter 3 to determine the magnitude of each normal loads and the corresponding friction coefficients.

The same analysis performed to show that a larger wear particle in an unconstrained sliding system causes higher friction compared with smaller particles can be demonstrated for the constrained systems. Consider the two sliding systems shown in Figure 2.8. It will be assumed that the stiffness of the system represented by the spring constant will be the same for the both configurations. Furthermore, the volume of the hemispherical part of the agglomerate will be considered negligible compared to the cylindrical part.

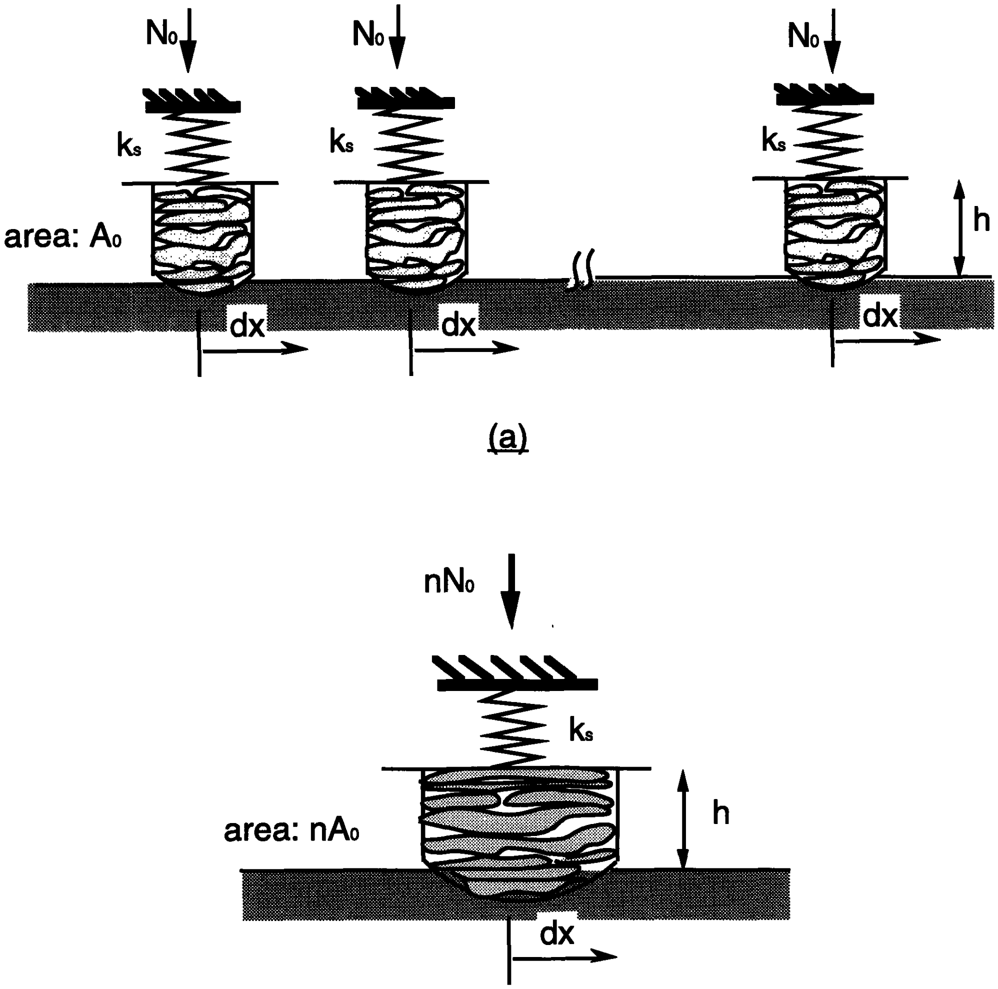

(a)

(b)

Figure 2.8 Plowing by multiple wear particle agglomerates (a) and by a single agglomerate of the same volume (b) sliding a differential distance of dx.

The variation of normal load with respect to the distance slid dx is given by eq. (2.8) in which the cross section area of the agglomerate can be expressed as

$$A = \frac{V}{nh} = \frac{V_p^i + V_W^s}{nh} \tag{2.18}$$

where V_p^i and V_W^s are the volume of wear particles before sliding and the volume of wear due to sliding a distance dx respectively. The sum of these two volumes is represented by V which is conserved in both configurations. Also, the initial stress on the agglomerates in both configurations is given as:

$$\sigma_0 = \frac{N_0}{A_0} = \frac{nN_0}{nA_0} \tag{2.19}$$

Therefore the change of normal load with respect to a differential distance slid is

$$\frac{dN}{dx} = \frac{Kk_s\sigma_0}{H}\frac{EV}{EV + k_s h^2 n} \tag{2.20}$$

The upper and lower bounds of this solution correspond to the spring constant equal to zero or infinity, respectively. These two cases are shown in Figure 2.9 and the intermediate curves correspond to the intermediate values of the stiffness of the system. When the spring constant is zero, the system is unconstrained and no increase in the normal load is expected. On the other hand, a rigid system (a system with an infinite stiffness) shows the sharpest increase in the normal load as the number of wear particles decreases. From eq. (2.20) the increase in the normal load in this case can be determined by taking the limit of the right hand side of the equation as k_s increase to infinity. This yields

$$\frac{dN}{dx} = \frac{K\sigma_0 EV}{Hh^2}\left(\frac{1}{n}\right) \tag{2.21}$$

The above discussion indicates that for a geometrically constrained sliding system, such as that shown in Figure 2.7, a single agglomerate situation will increase the normal load the most, provided that the volume of wear generated during the sliding is solely accumulated at one location. This of course will give an upper limit on the effect of agglomeration on the friction of geometrically constrained sliding systems.

2.10 Augment of Mechanical Components of Friction by Adhesion

Besides the direct effect of adhesion in the formation of secondary bonds at the interface which must be broken in order to allow relative motion, adhesion can also reinforce the mechanical components of friction such as asperity

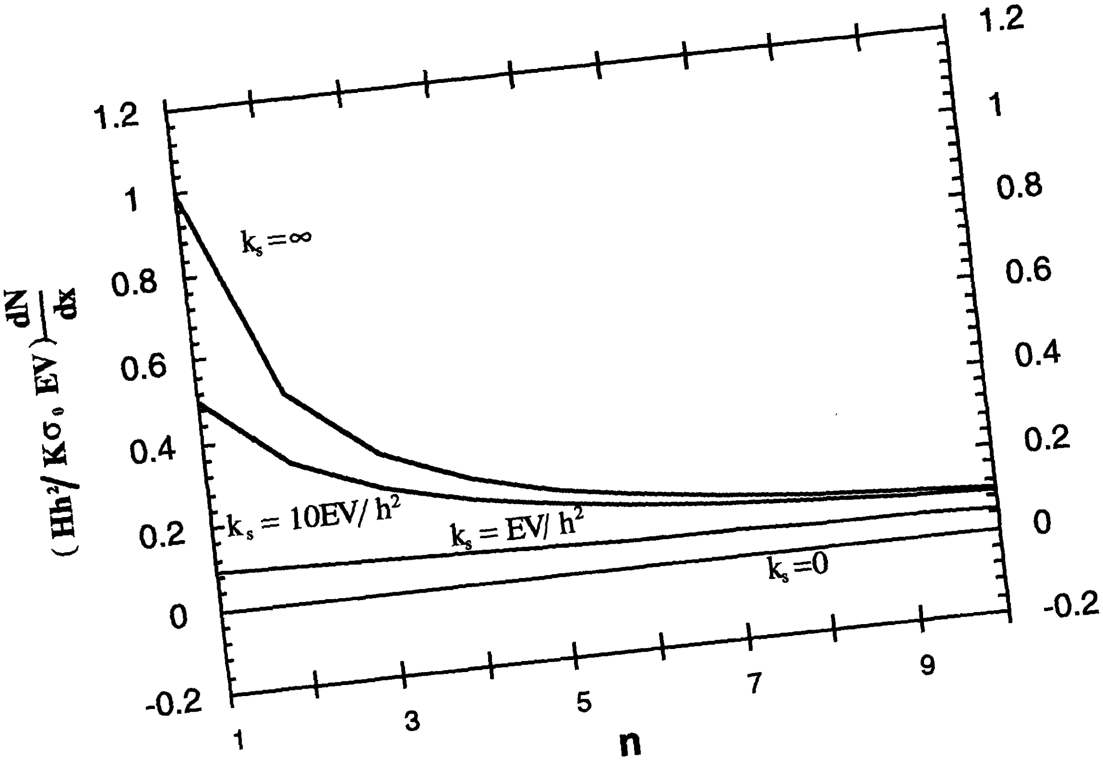

Figure 2.9 Increase in the normal load as a function of the number of entrapped wear particles and the stiffness of the system.

deformation, plowing by hard asperities and/or wear particles, and formation of large wear particle agglomerate. In particular, the process of wear particle agglomeration which is much like the cold compaction of metal powders can be greatly affected by the strength of the interfacial bonds between the small particles under compressive stresses.

There are situations which promote such interfacial bonds between wear particles such as in high vacuum and/or high temperature environments. The nonoxidized surfaces of newly formed particles in such environments can accelerate the agglomeration process which in turn adds to the severity of plowing. penetrate to either of the sliding surfaces and plow the softer material or

2.11 Friction in the Absence of Mechanical Interactions

The question of what would be the friction coefficient if all mechanical aspects of friction were eliminated is an important one which has inspired the goal of this research. In order to answer this question one must note that if friction were due to the break of the secondary Van der Waal s forces at the interface the friction coefficient would have been very low. This is the ideal sliding situation in dry sliding and the functional requirements to achieve such situation must first be identified.

2.11.1 Elimination of Gross Plowing by Removal of Wear Particles from Interface

The first step toward this goal is to reduce or eliminate the gross plowing of the interface by the hard asperities and/or wear particles. A means to reduce such damage to the surface has been shown to be the removal of wear particles from the interface either by wiping them out or designing surfaces with undulations [12].

Undulated surfaces consist of a series of parallel (or an orthogonal set of) microgrooves oriented perpendicular to the direction of sliding as shown in Figure 2.10 [13]. As wear particles are created they become trapped in the grooves, removing them from the sliding interface. Undulated surfaces serve the same purpose as liquid lubricants; they reduce the wear particle generation by plowing and delamination, remove wear particles from the sliding interface, and prevent wear particle agglomeration. This idea was originally created to demonstrate that the large friction force between identical materials is not due to greater adhesion between them compared with dissimilar materials.

Over the past decade, much research has been done to study the effectiveness of undulated surfaces. Both in dry and boundary lubricated sliding, undulated surfaces have been shown to lower friction down to the values of 0.1-0.2 and to reduce wear through the reduction of plowing [13]. In dry sliding, the friction coefficient of undulated surfaces was also found to be insensitive to the chemical compatibility of surfaces, which affirms the notion that adhesion is not the primary mechanism by which frictional forces are created at typical engineering sliding surfaces. Undulated surfaces were also found to significantly reduce friction in cases where liquid lubricants are ineffective, such as in the case of boundary lubricated sliding of titanium on titanium [29,30].

Undulation geometry is important to the effectiveness of these surfaces. The undulation geometry shown in Figure 2.11 is characterized by three parameters: pad length, l_p, gap length, l_g, and pad height, h_p. In general, an

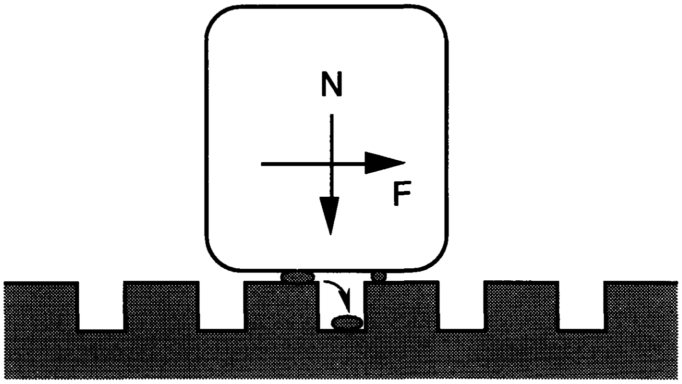

Fig. 2.10 Removal of wear particles from the interface to minimize the plowing component of friction

undulated surface will not operate effectively under the following conditions [14]:

$$\frac{l_g}{l_p} << 1 \tag{2.22a}$$

$$\frac{l_p}{l_g} << 1 \tag{2.22b}$$

$$\frac{l_p}{h_p} << 1 \tag{2.22c}$$

If the ratio of gap length to pad length is much less than unity, the pad length will be long enough to allow plowing and agglomeration. However, as shown in eq. (2.22b), the reciprocal of this ratio also cannot be much less than one or else plastic deformation of the pads may occur as there is insufficient pad area to carry the normal load. Finally, plastic deformation may also occur if the ratio of pad length to pad height is much less than unity. Furthermore the geometry must be such that the largest wear particle at the interface can be entrapped in the grooves.

2.11.2 Lowering Friction Through the Use of Smooth and Hard Covalent Surfaces

Although undulated surfaces showed significant improvement in the

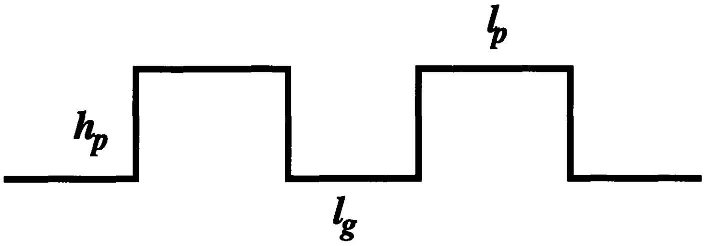

Figure 2.11 Geometry of undulations with a rectangular pad and groove cross-section

friction coefficient of many tested material, the damage to the surface of the undulations in the microscale was found [12]. This means that the micro plowing and local plastic deformation of the surface layer as a result of stress concentration at the asperity contact were not avoided. Therefore the second step toward elimination of plastic deformation of the surface to decrease the surface roughness to atomic level. The idea was that if the real area of contact is large enough the deformation of surface layer will be elastic and therefore the asperity deformation component of friction will be absent.

Kim and Suh [31] investigated the friction between extremely hard, smooth, and lightly loaded surfaces of silicon sliding against borosilicate glass and found the validity of the this idea. Friction coefficients as low as 0.09 were obtained and the surfaces seemed to have survived the test without any sign of permanent damage, as was revealed by examining in a scanning electron microscope. However, chemical etching of the silicon revealed the presence of dislocations created along the sliding direction. One conclusion was that even atomically smooth surface have atomic scale asperities which exert such high stress field in the substrate that can induce plastic deformation.

The subsurface plastic deformation detected in etching of the silicon and the possible nanoscale damage at the surface which was not detected in the SEM led to the design of a composite which is hard in bulk and extremely elastic at the surface and its molecules are covalently bonded together.

References

[1] MacCurdy, E., "The notebooks of Leonardo da Vinci", George Braziller, New York, 1958, PP. 601-607.

[2] Palmer, F., "What about friction", American Journal of Physics, 1949, pp. 181-187.

[3] Kragelski, Friction and Wear, Butterworth, Washington, 1965.

[4] Tomlinson, G.A., "A molecular theory of friction", Phil. Mag., Vol. 7, No. 46, 1929, pp. 905-939.

[5] Bowden, F.P., and Tabor, D., Friction and Lubrication of Solids, Clarendon Press, Oxford, Part I, 1950, Part II, 1964, pp. 90-121, pp. 52-86.

[6] Rabinowicz, E., Friction and Wear of Materials, John Wiley and Sons, New York, NY, 1965, pp. 32-40.

[7] Rabinowicz, E., "The role of surface energy in adhesion in metal working", J. Inst. Metals, Vol. 95, 1967, pp. 321-326.

[8] Voyutskii, S.S., Autoadhesion and Adhesion of High Polymer, Interscience, NY, 1963.

[9] Postnikov, S.N., Electrophysical and Electrochemical Phenomena in Friction, Cutting, and Lubrication, Van Nostrand Reinhold, 1978.

[10] Shaw, M.C., and Macks, E.F., "Analysis and lubrication of bearings", McGraw-Hill, New York, 1949.

[11] Suh, N.P., and Sin, H.-C., "The genesis of friction", Wear, Vol. 69, 1981, pp. 91-114.

[12] Suh, N.P., Tribophysics, Prentice-Hall, Inc., New Jersy, 1989.

[13] Suh, N.P., and Saka, N., "Surface Engineering", Annals of the CIRP, Vol. 36, 1987, pp. 403-408.

[14] Suh, N.P., Mosleh, M., and Howard, P.S., "Control of Friction", Wear, To appear, 1994.

[15] Kim, D. E., and Suh, N.P, "Plastic deformation of silicon during contact sliding at ambient temperature", Journal of Materials Science, Vol. 28, No. 10, 1993, pp. 3895-3899.

[16] Green, A.P., "Friction between unlubricated metals: A theoretical analysis of the junction model", Proceeding of the Royal Society of London, Series A, Vol. 228, 1955, pp. 191-204.

[17] Challen, J.M., and Oxley, P.L.B., "An explanation of the different regimes of Friction and wear using asperity deformation models", Wear, Vol. 53, 1979, pp. 229-243.

[18] Bowden, F.P., Moore, A.J.W., and Tabor, D., "The ploughing and adhesion of sliding metals", Journal of Applied Physics, Vol. 14, 1943, pp. 80-91.

[19] Goddard, J., and Wilman, H., "A theory of friction and wear during the abrasion of metals, Wear, Vol. 5, 1962, pp. 114-135.

[20] Antler, M., "Stages in the wear of a prow-forming metal", ASLE Trans., Vol. 13, No. 2, 1970, pp. 79-85.

[21] Cocks, M., "Shearing of junctions between metal surfaces", Wear, Vol. 9, 1966, pp. 320-328.

[22] Chang, Y.J., and Kuhlmann-Wilsdorf, D., "A case of wear particle formation through shearing-off at the contact spots interlocked through microroughness in adhesive wear", Wear, Vol. 120, 1987, pp. 175-181.

[23] Komvopoulos, K., Suh, N.P., and Saka, N., "Wear of boundary-lubricated metal surfaces", Wear, Vol. 107, No. 2, 1986, pp. 107-116.

[24] Ko, P.L., Robertson, M., and Magel, E.E., "Wear particle formation in lubricated sliding between a hardened sphere and a flat surface", Proc. of the 18th Leeds-Lyon Sump. on Tribology, Vol. 21, 1991, pp. 81-90

[25] Oktay, S.T., and Suh, N.P., "Wear debris formation and agglomeration" Journal of Tribology, Vol. 114, No. 2, 1992, pp. 379-393.

[26] Suh, N.P., "The delamination theory of wear", Wear, Vol. 25, 1973, pp. 111-124.

[27] Jahanmir, S., and Suh, N.P., "Mechanics of subsurface void nucleation in delamination wear", Wear, Vol. 44, 1977, pp. 17-38.

[28] Blunn, G.W., Walker, P.S., Joshi, A., Hardinge, K., "The dominance of the cyclic sliding in producing wear in total knee replacements", Clinical orthopedic and related Research", Vol. 273, 1992, pp. 253-260.

[29] Tian, H., Saka, N., and Suh, N.P., "Boundary lubrication studies on undulated titanium surfaces", Tribology Trans., Vol. 32, 1989, pp. 289-296.

[30] Saka, N. , Tian , H. , and Suh, N.P., "Boundary lubrication of undulated metal surfaces at elevated temperatures", Tribology Trans., Vol. 32, 1989, PP. 389-395.

[31] Kim, D. E., and Suh, N.P., "Frictional Behavior of extremely smooth and hard solids", Wear, Vol. 162-164, 1993, pp. 873-879.

Chapter 3

The Role of Wear Particles in Dry Friction of Geometrically Constrained Sliding Systems

3.1 Introduction

The conventional definition of the friction coefficient, the ratio of the frictional force to the normal load, might often not be meaningful. This situation arises when complete mechanical interlocking between two surfaces occurs or when strong primary bonds form between the atoms or molecules of the surfaces in contact. In theses situations, even when the normal load is released, the frictional resistance of the surfaces to the relative motion remains and the magnitude of the friction coefficient, by conventional definition, is basically infinity. In particular, when complete mechanical interlocking of the surfaces occurs, the highest frictional force is limited by the shear strength of the weaker of the two sliding materials as shown in Figure 3.1a [1]. Similarly, such complete mechanical interlocking can also be caused by a third-body at the interface, such as a growing wear particle agglomerate, in a constrained system, as shown in Figure 3.1b [2].

The formation of primary bonds between the atoms or molecules of the contacting surfaces is another cause for the frictional force to be independent of the normal load. Friction coefficients much higher than the one reported between clean surfaces in ultra high vacuum [3] can be considered as a case to which the conventional definition of friction coefficient does not seem applicable. Although the investigation of such a case satisfies scientific curiosity, its engineering applications are not many. This case will be studied in chapter 4 which describes the role of environment and in particular high vacuum and/or high temperature on friction of geometrically constrained sliding systems.

A typical example of such a situation of great engineering importance is the seizure of sliding surfaces in common engineering environments. It occurs when the operation of a mechanism suddenly comes to a stop due to a large increase in the resistance of surfaces to relative motion. This phenomena was first explained in terms of an increase in the real area of contact at the interface, followed by cold welding [4]. This explanation is based on the adhesion theory of friction which describes the frictional resistance of surfaces as the force required to shear the junctions at the interface. When such resistance is increased the only possible explanation will be the increase in the real area of contact. Another explanation was based on the a large deformation of rubbing surfaces at the interface which results in an interlocking of the moving bodies in contact [5]. The role of wear particles in seizure, especially when the sliding system does not allow the their removal, was addressed later [2,6]. In a solution presented for galling seizure, it was proposed that the clearance of the system must be larger than the maximum size of generated wear particles [7]. However, wear particles were assumed to be the individual particles and the effect of agglomeration of wear particles was neglected. Therefore, the solution does not satisfy the requirements of a precision sliding element. The formation of large wear particles through agglomeration [8] or delamination under cyclic loading [9] was addressed later and solutions for unconstrained systems were examined.

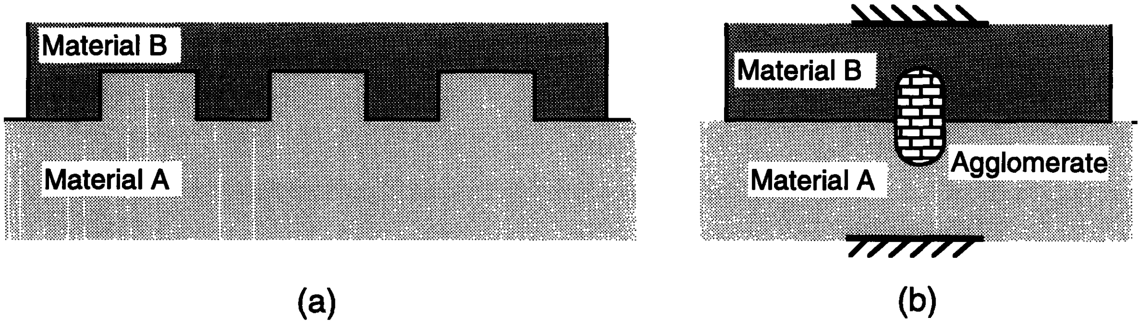

Figure 3.1 Complete mechanical interlocking of sliding surfaces due to the topography of the surfaces in contact (a) or due to an entrapped wear particle agglomerate in a geometrically constrained system(b).

Although, by using a lubricant the seizure might be prevented or delayed in many practical applications, there are other applications in which the use of a liquid lubricant is not tolerated or it is not possible. Therefore, a basic understanding of the phenomenon along with a surface engineering solution is sought in this study. In this chapter the experimental results and modeling of friction of constrained sliding contact bearings operating without a lubricant will be presented. These sliding systems are believed to be the examples of situations in which the mechanical interlocking due to the agglomeration of wear particles occurs and results in catastrophic failure.

3.2 Sliding Contact Bearings

Bearings are essential components of machines having moving elements. They allow the relative motion of engaged parts in certain directions, while constrain them from moving in the direction of the applied load. Sliding contact bearings are the simplest, least expensive, and the most commonly used type of bearings which can provide high stiffness and precision for engineering applications [10].

The geometric constraints of sliding bearings arise the possibility of entrapment of wear particles which can result in a sudden increase of the normal and tangential loads. The likelihood is especially high when sliding bearings are operating dry or in a poorly lubricated sliding regimes. The increase in the normal and tangential forces in turn leads to a catastrophic failure of the bearings. Even in many applications involving hydrodynamic lubrication, the sliding conditions may range from dry or boundary lubricated sliding to a full-film sliding regimes. A good example of such varying lubrication conditions is the sliding condition at the piston ring/cylinder interface in the internal combustion engines [11].

A typical Stribeck diagram which shows the different modes of lubrication experienced by piston rings during a single stroke of operation is presented Figure 3.2. The friction coefficient and the lubrication regime is qualitatively plotted versus the Sommerfeld number which is defined as:

$$S=\left(\frac{\xi N}{P}\right)\left(\frac{D}{C}\right)^2 \tag{3.1}$$

where ξ : lubricant viscosity

N : rotational Speed

P : pressure
D : typical bearing length
C : diametral clearance

At low values of the Sommerfeld number, which is the situation for the start up of operation of journal bearings or at the end of strokes in an engine, the friction coefficient is high and leads to high wear. Direct metallic contact at some spots at the interface generates wear particles and the subsequent problems of such particles in a geometrically constrained systems arises. Of course, the existence of a lubricant will prevent agglomeration but will not remove the chance of plowing damage of the surface due to the particles themselves.

Besides developing new lubricants to provide more effective lubrication, the problem can be tackled by the design of the profile geometry of sliding surfaces. For instance, undulated surfaces can be employed to remove the particles from the interface and satisfy the precision requirements.

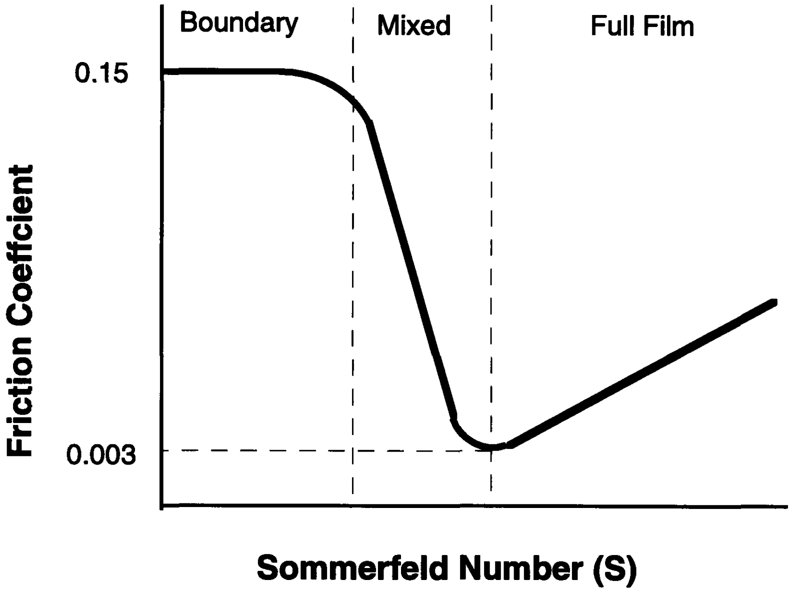

Figure 3.2 Stribeck diagram showing friction in different regimes of lubrication.

In the following sections it will be shown that agglomeration of wear particles in the dry sliding of constrained systems results in catastrophic failure.

Scanning electron microscopy of the seized interfaces will be used to verify this hypothesis. Also, a theoretical model will be developed to explain how the frictional resistance of constrained systems can suddenly increase to extremely high values. Finally, the effectiveness of undulated surfaces will be experimentally investigated. Such surfaces have been shown to reduce the friction coefficient and prevent from gross plowing of the interface by wear particles mostly in unconstrained system. Their effectiveness in real practical bearings is tremendous.

3.3 Experimental Overview

The experimental studies of friction of sliding bearings were performed in two phases. The first phase investigates whether the hypothesis of mechanical interlocking due to wear particles in geometrically constrained sliding systems is valid. In the second phase the experimental data will be used to develop a model which shows the increase in the normal load as a result of wear particle agglomeration in geometrically constrained systems.

3.3.1 Accumulation of Wear Particles at the Interface of Geometrically Constrained Sliding Systems

3.3.1.1 Apparatus and Procedure

Figure 3.3 schematically shows the rotary sliding bearing tester used in the experiments. The driving torque to the shaft was supplied by a lathe chuck. The extended arm connected to the bushing was constrained from the rotation by a string which was connected to a load cell. At the top of the bushing the normal load was applied by dead weights. The load cell continuously monitors the force applied to the string and calculates the frictional torque (τ) as

$$\tau = Tb \tag{3.2}$$

where T and b are the force on the string and the distance from the string to the center of the shaft, respectively. If the frictional resistance of the bearing increases beyond a certain value, the string will rupture and the shaft/bushing assembly will rotate together. This assures that the frictional resistance at the seizure point will remain the same for all tests.

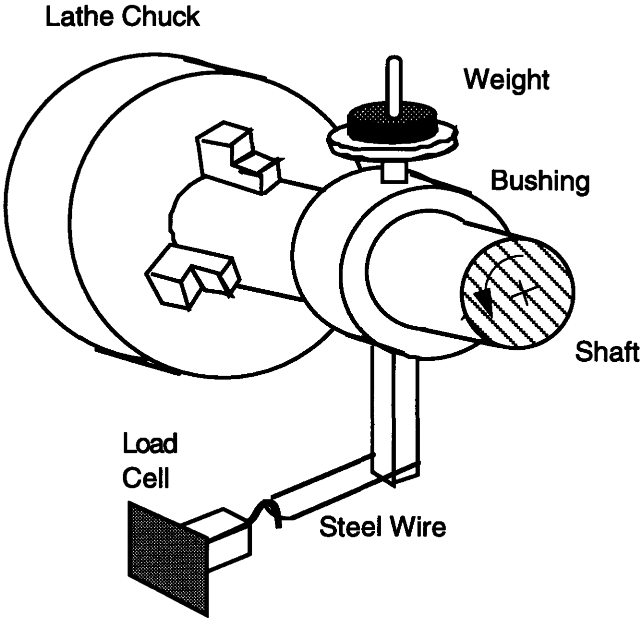

Figure 3.3 Schematic of friction tester for rotary sliding bearings.

3.3.1.2 Materials and Experimental Conditions

The combination of stainless steel 304 and a boride dispersion strengthened copper supplied by Sutek Co. were used throughout the experiments. The boride dispersion strengthened copper, commercially named MXT3 by the manufacturer, consists of a pure copper matrix dispersed with nanoscale particles of titanium diboride (TiB_2). The submicron titanium diboride particles have remarkably high thermal stability and serve to pin subgrain boundaries and dislocations, thus preventing recrystallization. This gives high thermal conductivity and high hardness properties to the copper. The hardness of MXT3 as a function of the annealing temperature is given in Figure 3.4 compared with two other precipitation hardened copper alloys, namely Cu-Cr and Cu-Zr.

A summary of mechanical properties of the materials used in the experimental study is given in Table 3.1. The mean surface roughness of both copper shafts and stainless steel bushing were approximately 100 μm.

All experiments were performed at a sliding speed of 5.25 cm/s. The load varied between 11.25 and 45 N. The distance slid for one rotation of the shaft was about 9.75 cm. A summary of the experimental conditions common to all tests are given in Table 3.2.

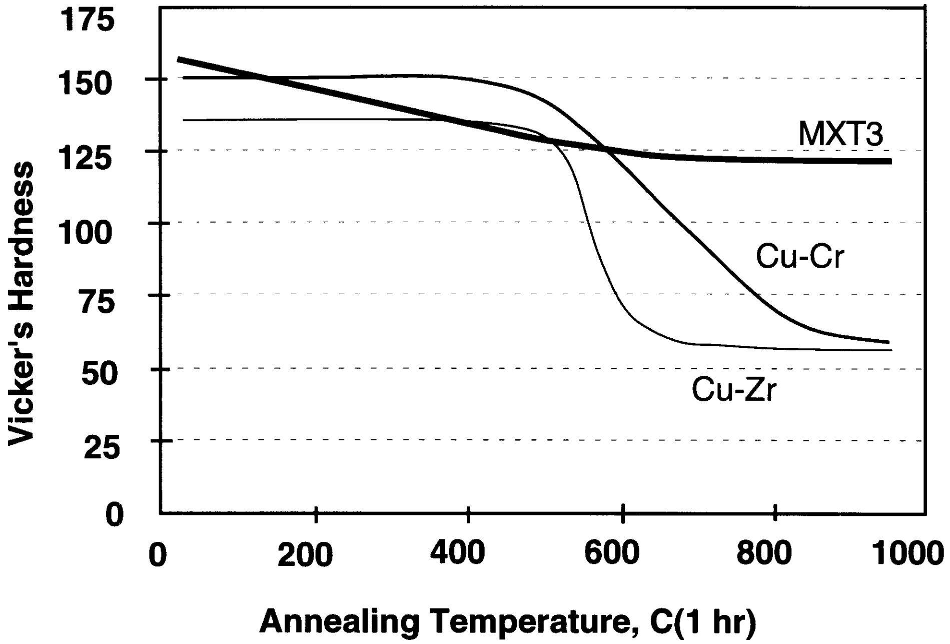

Figure 3.4 Hardness of MXT3 vs. the annealing temperature.

Table 3.1 Mechanical properties of materials used to perform dry friction tests of rotary sliding bearings.

Property	**MXT3**	**Stainless Steel 304**
Hardness (MPa)	1100	1430
Tensile Stress (MPa)	378	750
Modulus (GPa)	115	190
Thermal Expansion Coefficient (m/m C) $\times 10^{-6}$	17.7	15

Table 3.2 Experimental conditions in dry shaft-in-bushing experiments.

Normal Load (N)	11.25, 22.5 and 45
Speed (cm/s)	5.25
Temperature (C)	25
Environment	Laboratory Air
Lubricant	None

3.3.1.3 Fabrication of Undulated Bearings

Figure 3.5 shows the experimental configuration and nominal size of undulations on the shaft. There are two important factors that must be considered while using undulated surfaces. First, undulations must be put on the softer material; otherwise, the sharp edges of the undulations on the harder surface will cause severe plowing and abrasion of the softer material. Second, in order to avoid rapid localized wear of undulations, they must be present on the rotary part.

The undulated shafts were fabricated using a thin cutter on a CNC milling machine. The shafts were held on a rotary table and a groove was cut by axial motion of the cutter. After each cut, the rotary table was rotated by an assigned rotation and a new cut was made. Burrs produced during the cutting process were removed by grinding each shaft lightly to the final size. Other techniques such as molding or photolithographic etching could also be used to create such surface profiles especially when extremely small pads and grooves in the range of a few micrometers or less is desired. An SEM micrograph of the undulations made by the machining technique is shown in Figure 3.6.

3.3.1.4 Results

Dry sliding tests were performed under three different normal loads, i.e. 11.25, 22.5, and 45 N. Also the diametral clearance was varied form 12.5 μm to 50 μm. All tests were terminated when the frictional torque reached 2.2 N-m. The frictional torque of the tested bearings is shown in Figure 3.7 through Figure 3.9.

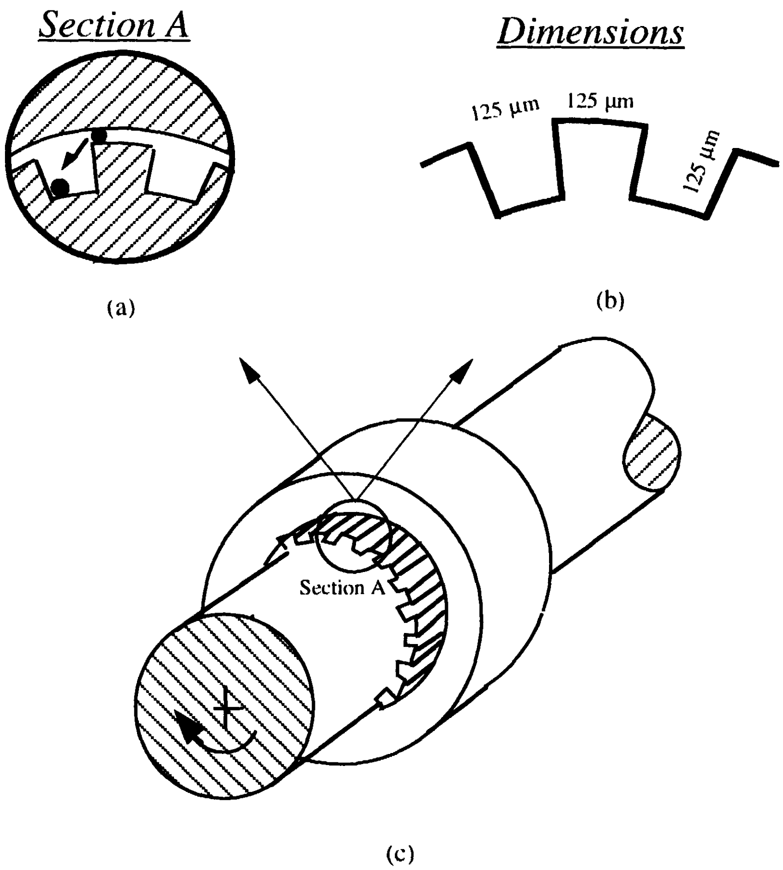

Figure 3.5 Illustration of entrapment of wear particles in undulations (a), nominal size of undulations (b), and the configuration of an undulated shaft in a bushing (c).

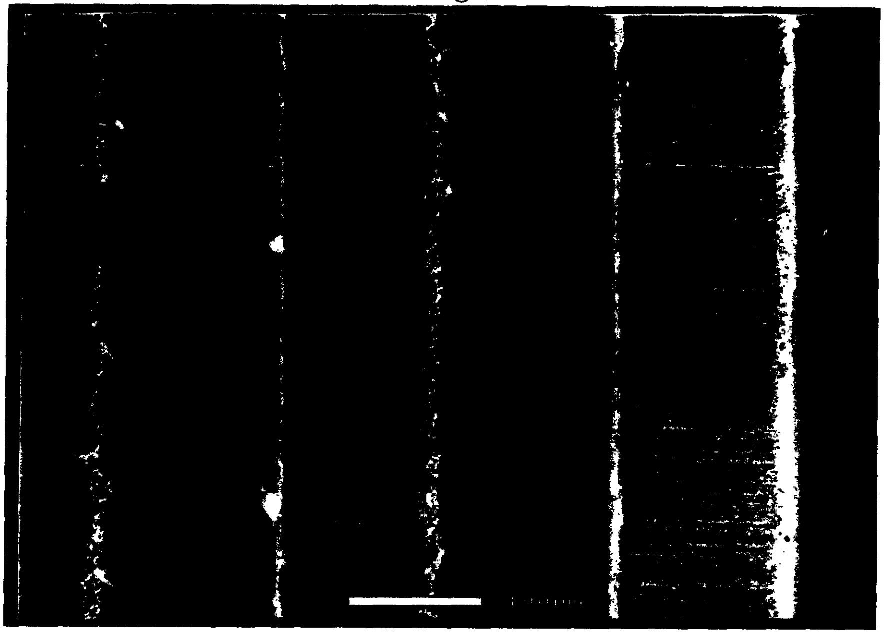

Figure 3.6 Micrograph of machined undulations.

Figure 3.7 is the frictional torque of bearings with a diametral clearance of 50 μm. The same plots for the bearings with 25 μm and 12.5 μm clearance are shown in Figure 3.8 and Figure 3.9, respectively. There are three major observations from the seizure experiments. First, for a certain diametral clearance, as the normal load increases, the number of the cycles before seizure decreases. Second, for a certain load, the number of cycles before seizure exponentially increases as the diametral clearance becomes larger. Third, when the diametral clearance of the bearing was larger than about 50 μm, the bearings operated without any sudden increase in the frictional torque for more than 10,000 cycles.

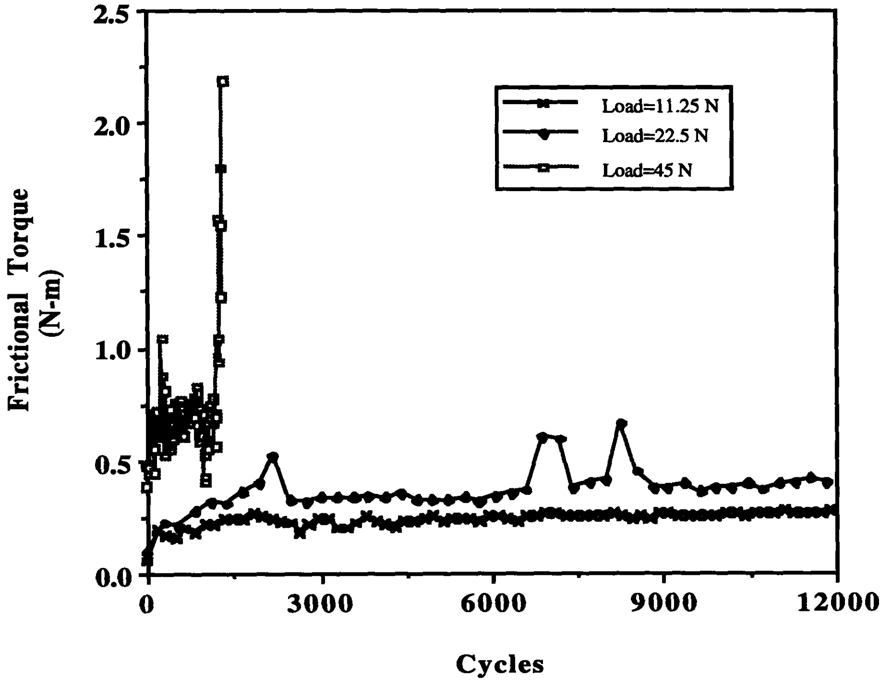

Figure 3.7 Frictional torque of smooth bearings with 50 μm diametral clearance.

Another feature of the dry tests was the abrupt increase in the frictional resistance of the bearing which experienced seizure. This sudden increase becomes sharper as the diametral clearance of the system gets smaller. This phenomenon can be well explained by the hypothesis that wear particle

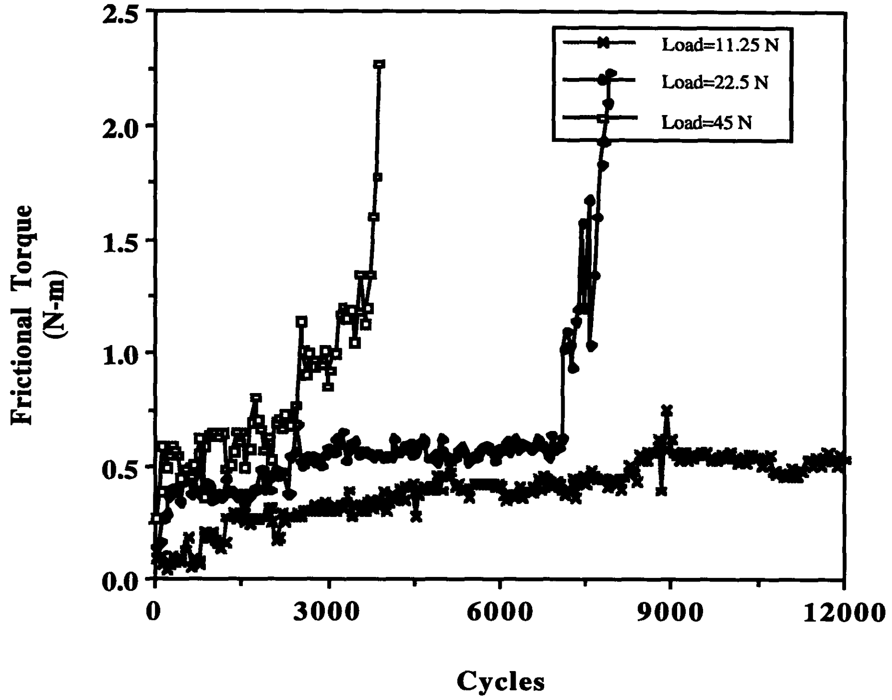

Figure 3.8 Frictional torque of smooth bearings with 25 μm diametral clearance.

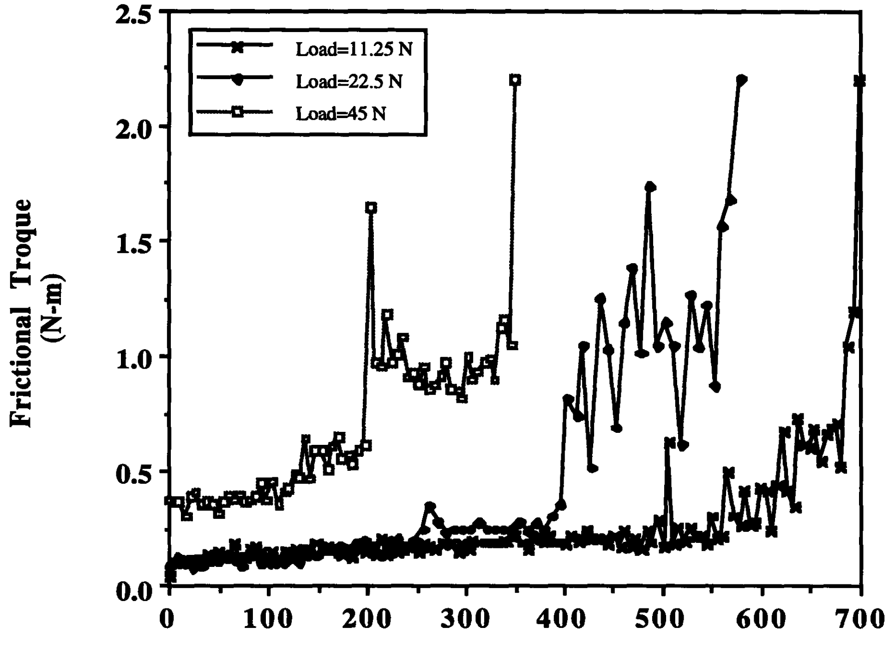

Figure 3.9 Frictional torque of smooth bearings with 12.5 μm diametral clearance.

entrapment at the interface is the cause of such increase.

The interface of the seized samples were examined in ESEM after the following preparations. First, the seized shaft/bushing assembly was sliced at several places along its length because the exact position of the wear particle entrapment between the shaft and the bushing was not known. Each slice then was ground with a fine stone and lapped with a silicon carbide compound. The size of the silicon carbide particles in the compound was less than 0.5 μm. Generally, the size of the loose wear particles in the lapping process tend to be about twice of the size of the abrasive particles. Therefore, the loose wear particles of about 1 μm will not clog the clearance and can be removed. The samples were ultrasonically cleaned in acetone. They were then etched in a nitric acid-water solution of 50% concentration for 15 seconds. They were again cleaned ultrasonically to remove any loose particles and examined with an ESEM.

Figure 3.10 shows two micrographs of the interface of a seized bearing at two different locations. These two points are the maximum and minimum separations between the shaft and the bushing. The bearing was tested under 45 N normal load and the diametral clearance initially was approximately 50 μm. From Figure 3.10 it seems that the gap size has increased due to the delamination of wear sheets from the copper shaft. The interface of a seized bearing with a diametral clearance of 25 μm tested under 22.5 N normal load is shown in Figure 3.11. Finally, for the bearings with a diametral clearance of 25 μm tested under the normal load of 11.25 N, the interface is shown in Figure 3.12.

In taking the SEM micrographs, care was taken to identify the angular location at which the highest wear particle at the interface was entrapped. Also the position where the minimum separation between the two surfaces occurred was measured. Figure 3.13 schematically shows the two positions where the micrographs in the scanning electron microscope were taken. The numerical values of such angles are given in Table 3.3.

3.3.2 Variation of Normal Load Due to Entrapment of Wear Particles at Interface

The purpose of this phase of experimentation was to show that wear particles in geometrically constrained sliding systems contribute to the increase in the normal load, which subsequently results in higher friction and possibly in seizure. This was verified by measuring the hoop strain in a bushing which had

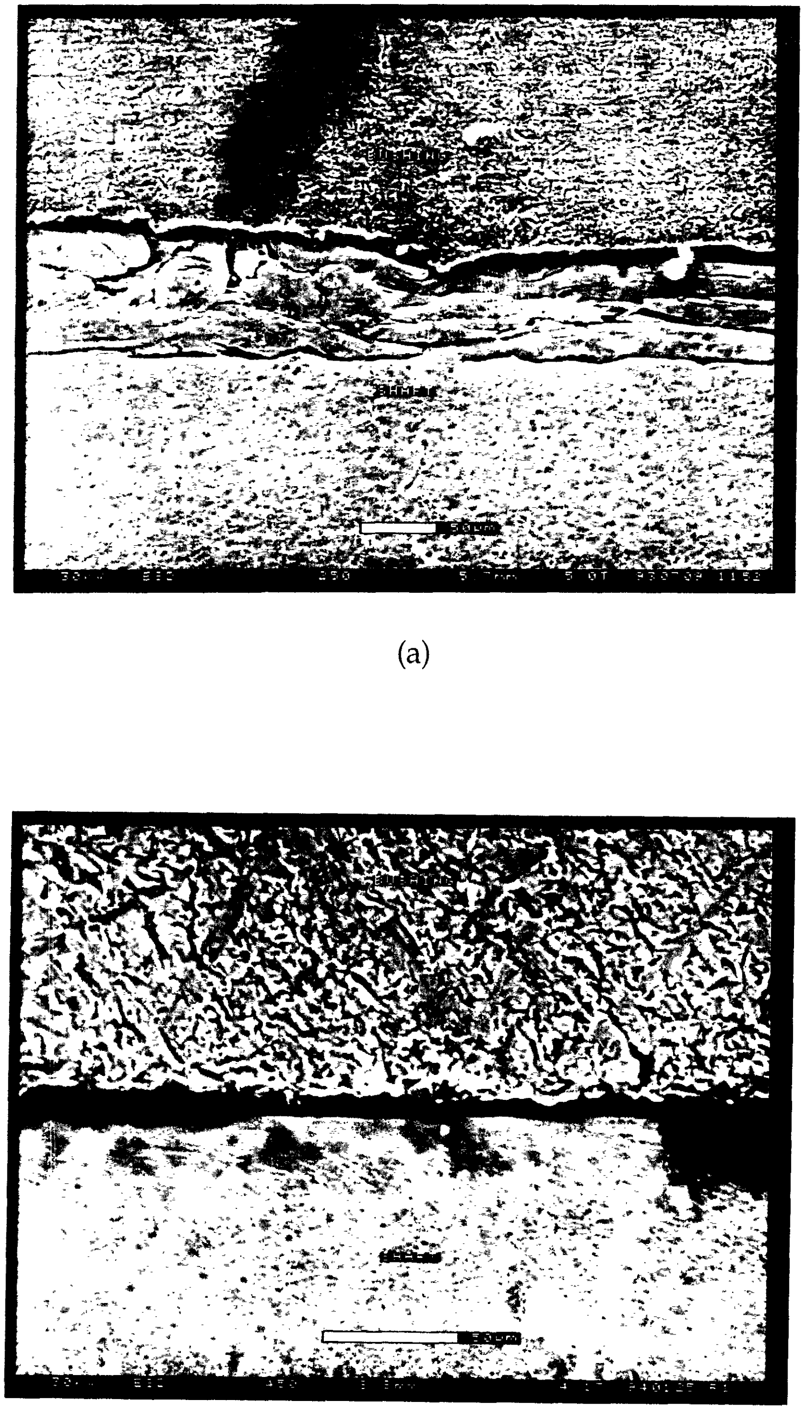

(a)

(b)

Figure 3.10 Micrograph of the interface of a seized smooth bearing with a diametral clearance of 50 μm showing the maximum (a) and the minimum separation locations (b). Normal Load= 45 N.

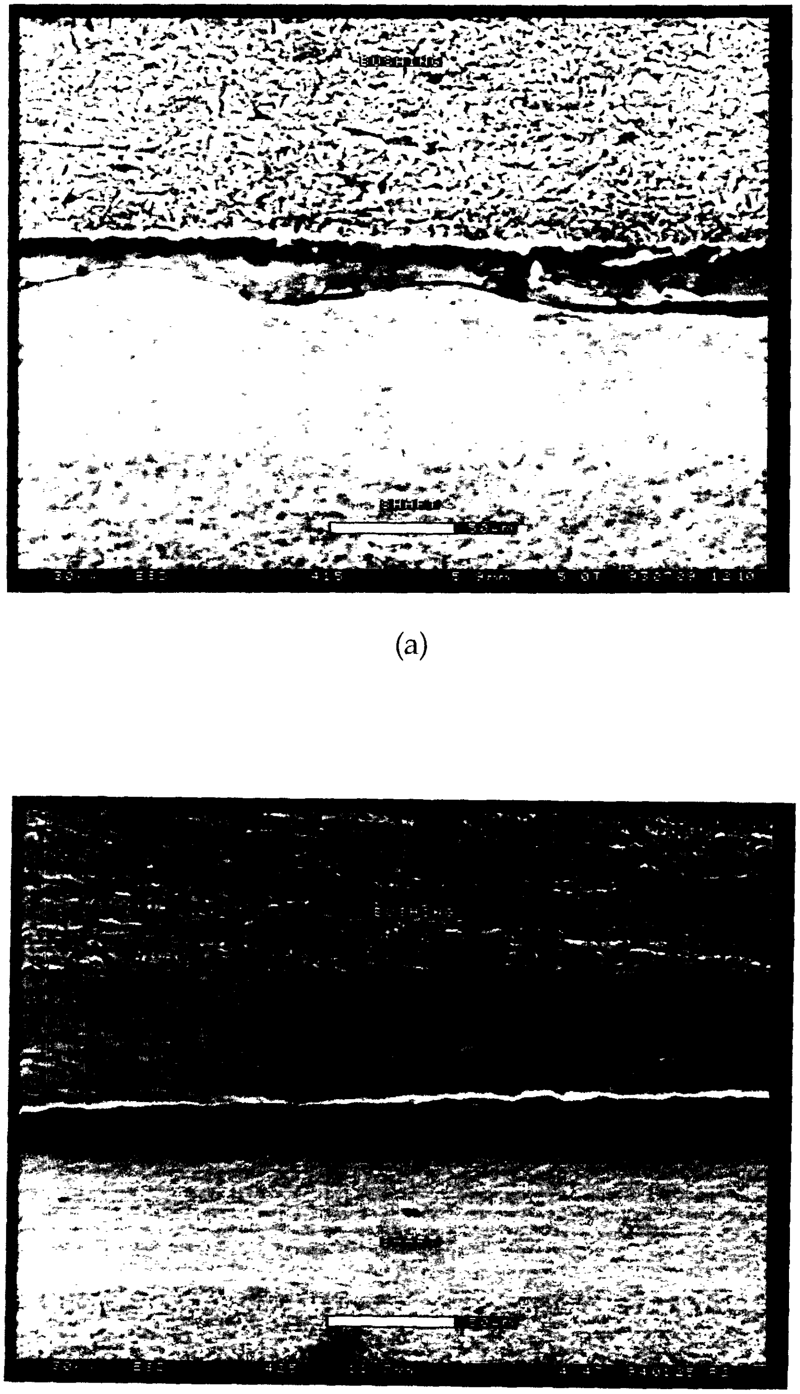

(a)

(b)

Figure 3.11 Micrograph of the interface of a seized smooth bearing with a diametral clearance of 25 μm showing the maximum (a) and minimum separation locations (b). Normal Load= 22.5 N.

(a)

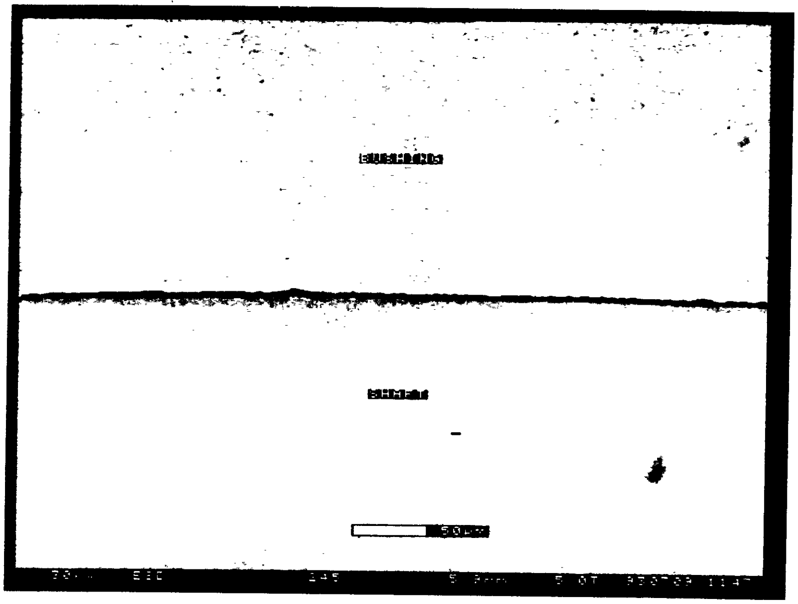

(b)

Figure 3.12 Micrograph of the interface of a seized smooth bearing with a diametral clearance of 12.5 μm showing the maximum (a) and minimum separation locations (b). Normal Load= 11.25 N.

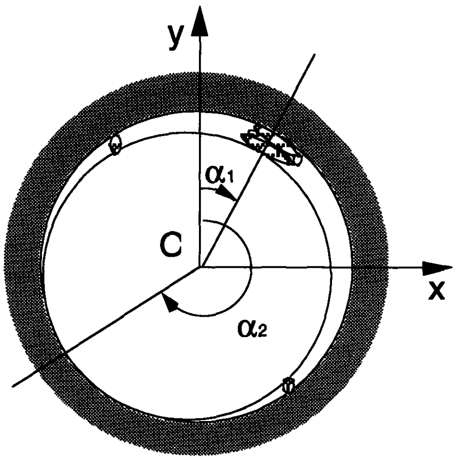

Figure 3.13 The angular position of maximum and minimum separation points between the sliding surfaces.

Table 3.3 The angular location of the maximum and minimum separation points of the seized interface measured from the y axis corresponding to the SEM micrographs.

Normal Load (N)	**Angle of Maximum Separation α_1 (deg.)**	**Angle of Minimum Separation α_2 (deg.)**
11.25	48	225
22.5	33	153
45	20	162

been slid dry against a shaft with the frictional torque measured simultaneously.

3.3.2.1 Experimental Setup and Procedure

The same apparatus shown in Figure 3.3 was used except that strain gages were installed on the bushing and the bushing was held inside a housing as shown in Figure 3.14. The angle between the line connecting the strain gages on the bushing and the vertical line (η) could be changed by rotation of the ring inside the housing. To get consistent results different values of η was tested, but the following results obtained with η=90 degrees. Also, around the housing tapped holes were made for the connection to the extended arm and the dead weight plate.

The same materials and experimental conditions stated in section 3.3.1.2 were used in this phase of experimentation.

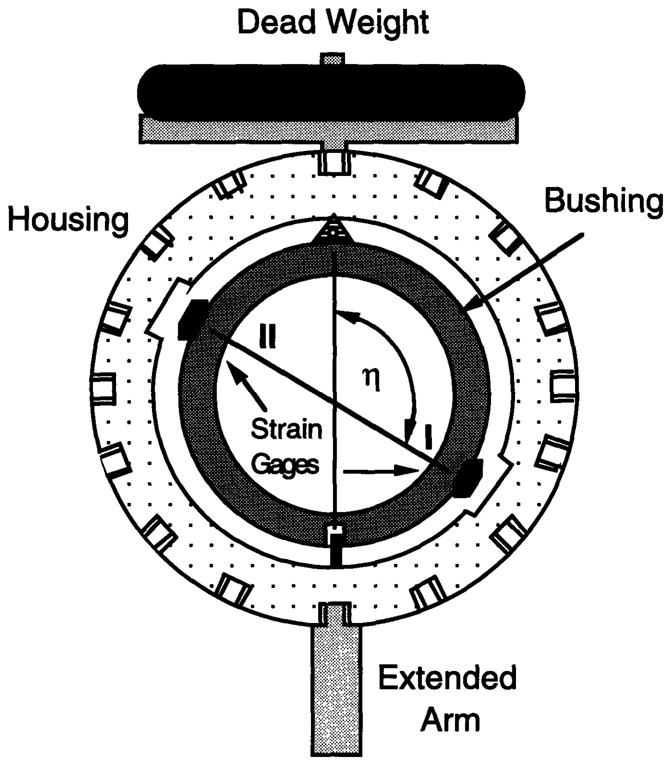

Figure 3.14 The housing support of the bushing showing the location of the strain gages.

3.3.2.2 Smooth Bearings Results

A plot of the frictional torque and the differential output voltage of the strain gages, which is proportional to the hoop strain of the ring is shown in Figure 3.15 for 11.25 N normal load. A sudden increase in the frictional torque and the output voltage can be observed after about 400 cycles. When the normal load was 22.5 N the sudden increase occurred after 350 cycles as shown in Figure 3.16. The frictional torque and the output voltage versus the number of cycles for a test with 45 N normal load is presented in Figure 3.17. The transition from low to high friction has occurred after 100 cycles

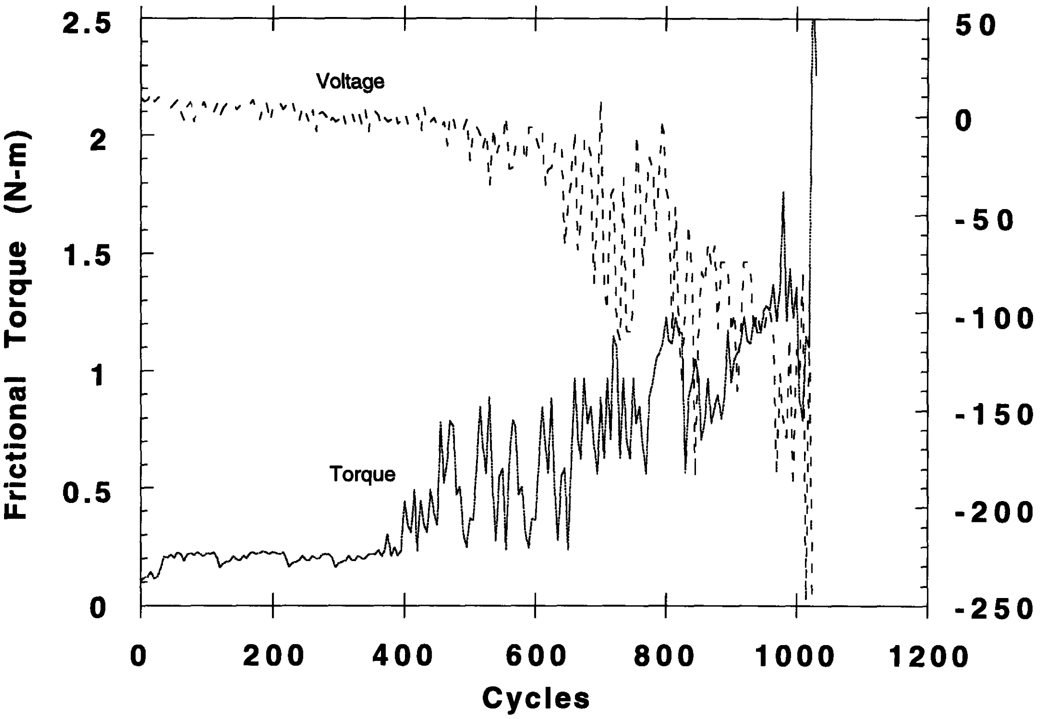

Figure 3.15 Frictional Torque and the output voltage from strain gages of a smooth bearing with 15 µm diametral clearance. Normal Load= 11.25 N

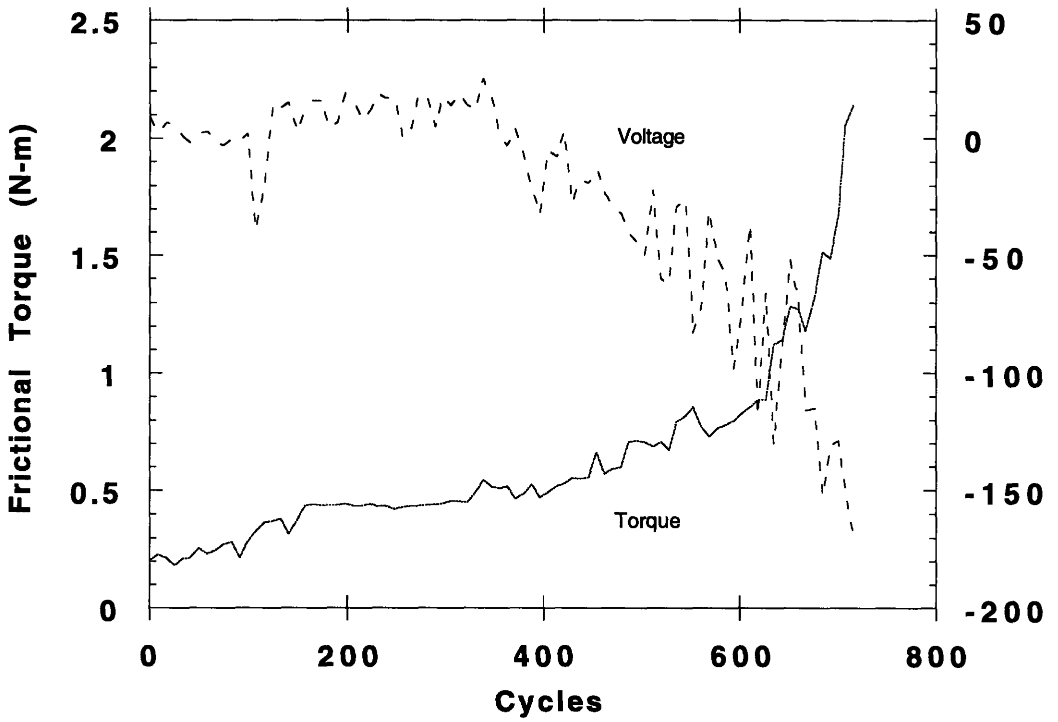

Figure 3.16 Frictional Torque and the output voltage from strain gages of a smooth bearing with 15 µm diametral clearance. Normal Load= 22.5 N

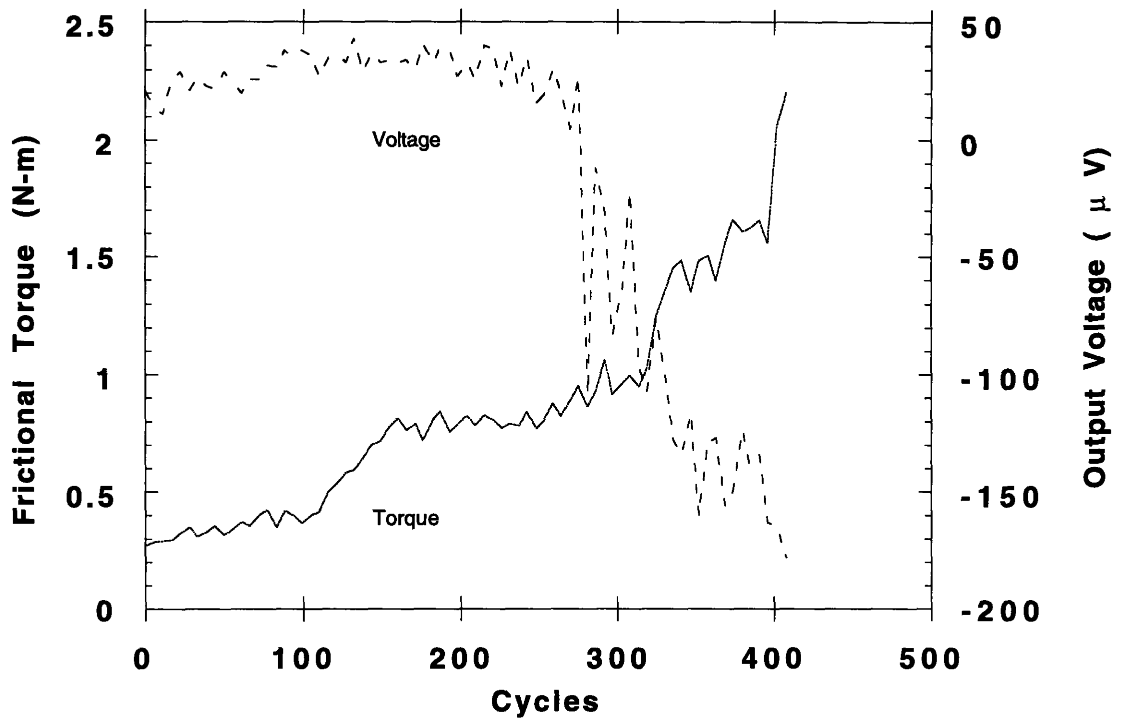

Figure 3.17 Frictional Torque and the output voltage from strain gages of a smooth bearing with 15 μm diametral clearance. Normal Load= 45 N

in the frictional torque. However, the transition in the output voltage did not occur until 250 cycles were reached.

The two variables shown in the plots, i.e. the frictional torque and the output voltage, are generally synchronized. The transition from a low friction to a high friction regime is assumed to be the starting point of a multiple contact situation, which will be analyzed later.

3.3.2.3 Undulated Bearings Results

Undulated bearings were friction tested under the same experimental conditions as of the smooth bearings given in Table 3.2. The diametral clearance of all bearings was 15 μm and the normal load was varied. The frictional torque and the output voltage of an undulated bearing with a normal load of 11.25 N is shown in Figure 3.18. When the normal load was 22.5 N, the results obtained are

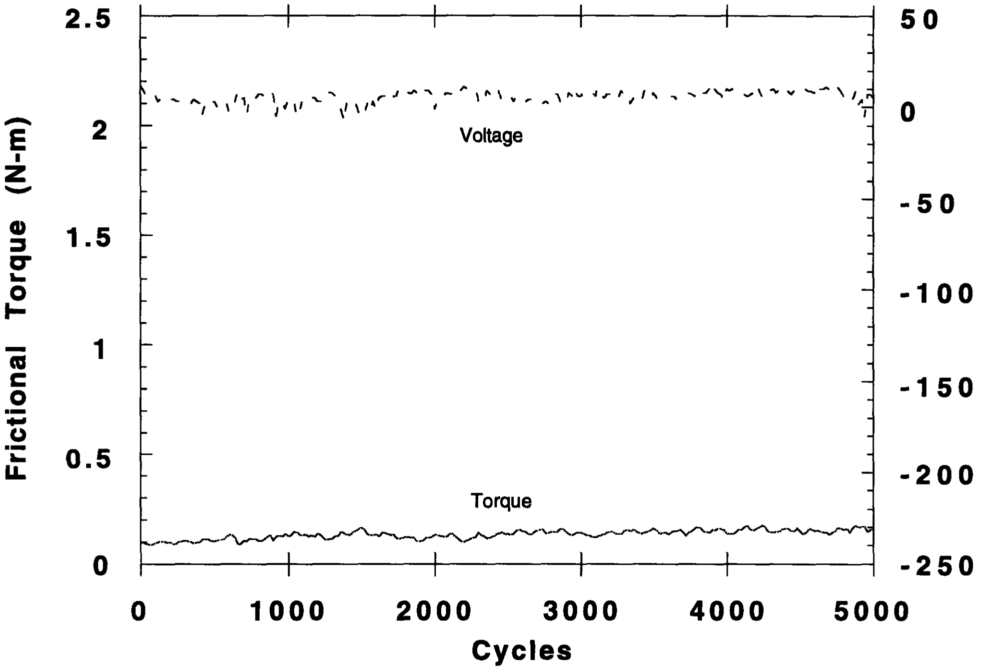

Figure 3.18 Frictional torque and the output voltage from the strain ring for an undulated bearing with 15 μm diametral clearance. Normal Load= 11.25 N

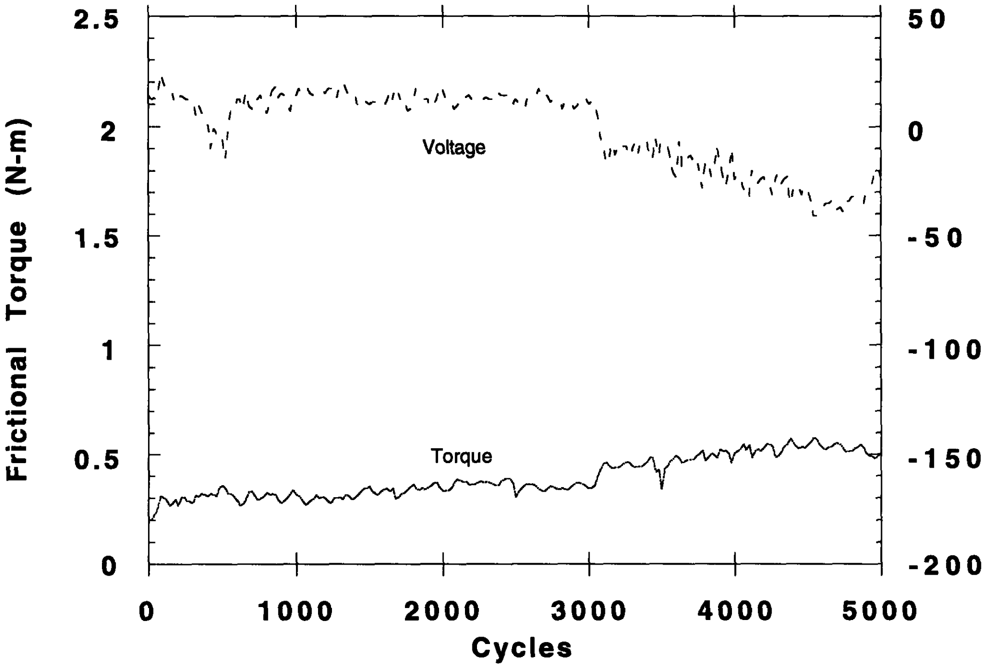

Figure 3.19 Frictional torque and the output voltage from the strain ring for an undulated bearing with 15 μm diametral clearance. Normal Load= 22.5 N

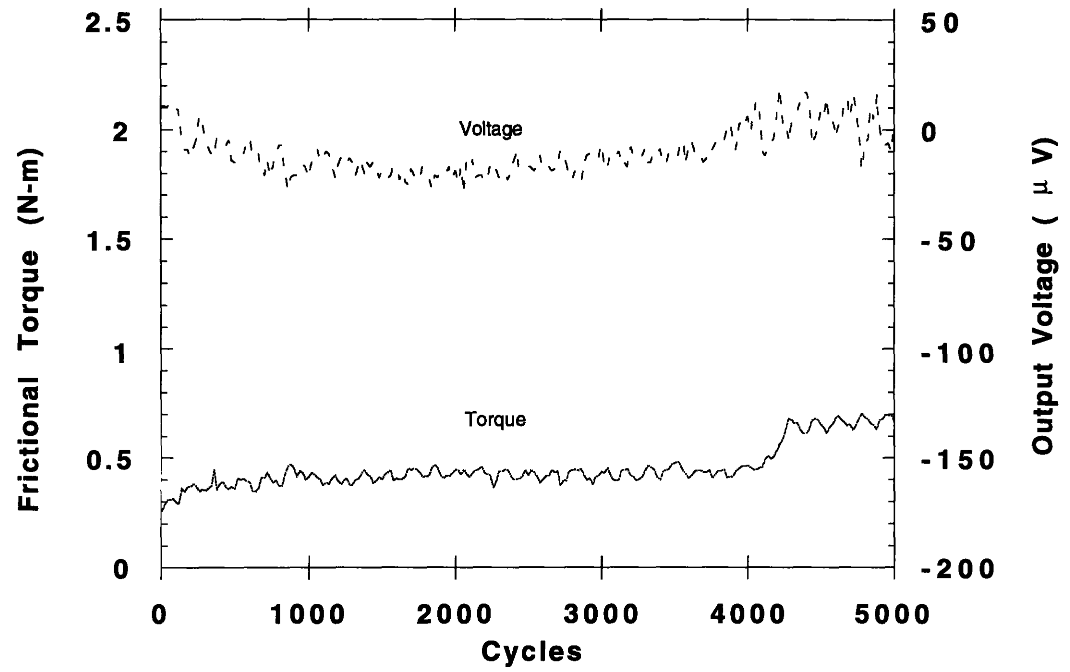

Figure 3.20 Frictional torque and the output voltage from the strain ring for an undulated bearing with 15 μm diametral clearance. Normal Load= 33.75 N

shown in Figure 3.19. Finally, Figure 3.20 shows the frictional torque and the output voltage of the strain ring for a normal load of 33.75 N. Analyzing the performance of undulated bearing, one must first notice the difference in the number of cycles between the undulated and smooth bearings. The life of undulated bearings with a low frictional torque is an order of magnitude greater than that of smooth bearings. Also, there is no sudden increase in the frictional torque of any of the undulated bearings, and no corresponding increase in the output voltage of the strain ring. However, if the undulations are filled with the wear particles due to a long operation of undulated bearing, their effectiveness may vanish and extensive plowing and/or plastic deformation of undulation pads might occur, resulting in high friction.

3.3.2.4 Removal of Wear Particles from the interface by Undulated Surfaces

The performance of undulation bearings depends on how effectively removal of wear particles before their agglomeration takes place. Therefore, when undulated surfaces are used and low friction coefficients are obtained, the entrapment of small wear particles must be seen in the grooves of undulations. Using a scanning electron microscopy an examination of undulated shafts tested under different normal load in confirmed that submicron to a few microns sized wear particles were trapped in the grooves. Figure 3.21 shows the undulations of a shaft tested under 11.25 N for 5000 cycles. When the normal load was 33.75 N, large amount of wear particles were observed in the grooves of undulations as shown in Figure 3.22a. In some regions even complete filling of the undulations was observed as shown in Figure 3. 22b. The plowing of the undulation pads can be seen in all these micrographs indicating that even wear particles in undulated surfaces plow the surface before they become entrapped.

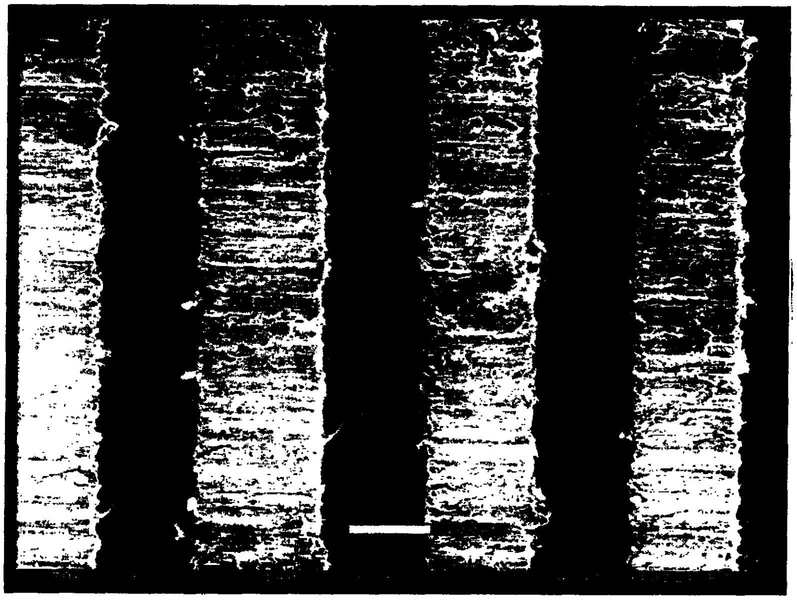

Figure 3.21 Trapping of wear particles in the grooves of an undulated shaft.
Normal Load= 11.25 N

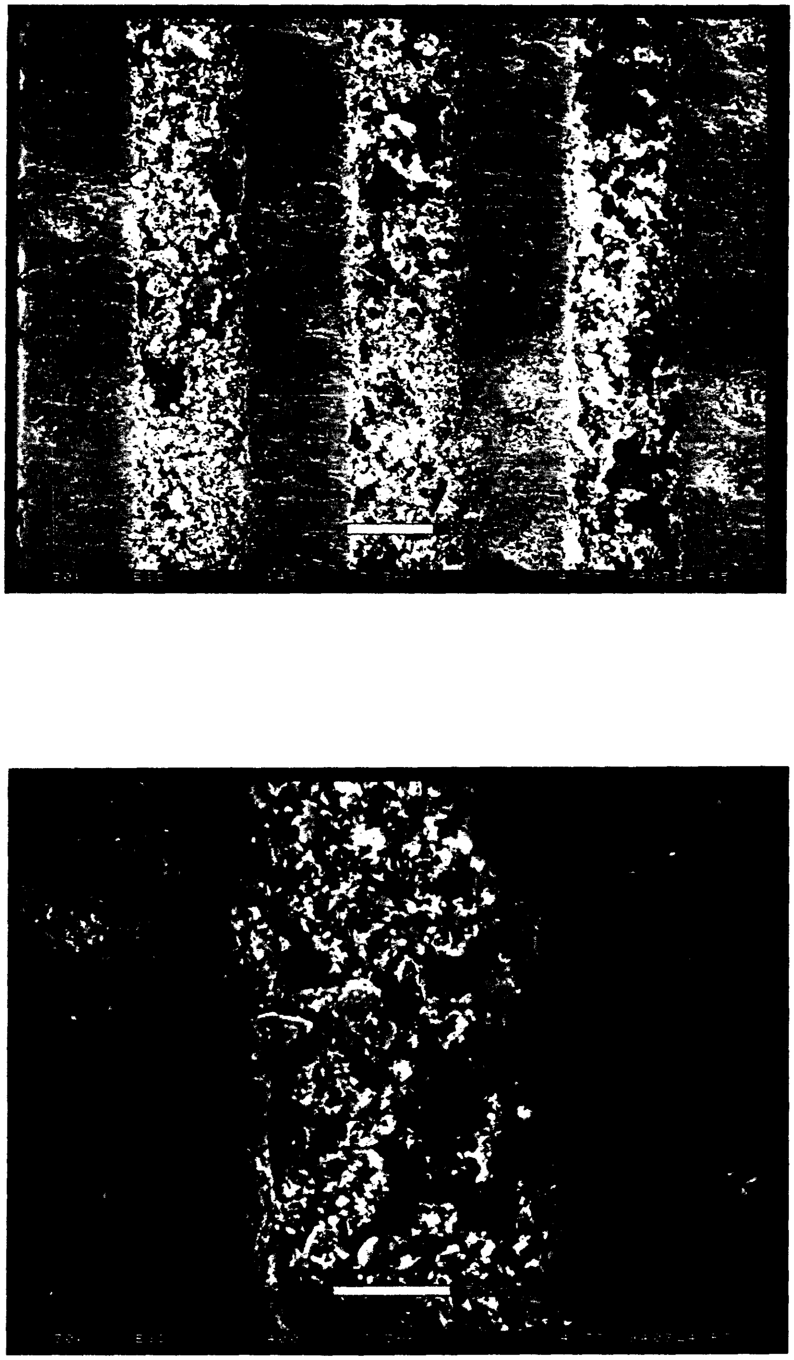

Figure 3.22 SEM micrographs with two different magnifications showing wear particles trapped in the grooves of an undulated shaft.
Normal Load=33.75N.

3.4 Analysis of Normal Load Variation

The wear particle agglomeration in a geometrically constrained system is a random phenomena whose exact location and the number of wear agglomerate at a certain time is not known. In a given system, at a certain time, many wear particles might become entrapped at the interface at the same time which results in a multiple contact situation. Also, the initial contact angle will change over the course of the test. However, to simplify the problem, the following assumptions were made to develop an expression which describes the contact forces based on the experimental data obtained from the strain gages on the bushing during the tests:

- The bushing is modeled as a thin ring whose thickness-to-diameter ratio is less than 0.1. Therefore, the elastic energy is calculated solely due to the bending moment at each cross section.
- The primary angle of contact α is calculated from the frictional torque data whenever a sudden increase in its magnitude was experienced. Furthermore, from that instant the value of α is assumed to remain constant.
- A two-point contact situation is assumed from transition to the end of the experiment, one at an angle of α and the other at $\pi + \alpha$.

3.4.1 Equilibrium Conditions

The equilibrium conditions can be derived from the free body diagram of the ring and the housing as shown in Figure. 3.23. It is assumed that the two contact points are 180 degrees apart from each other and the connecting line between them make an angle of α with the vertical line. The equilibrium equations for the bushing are:

$$\begin{aligned} &(N_1 - N_2)\sin\alpha - (F_1 - F_2)\cos\alpha + P_1 - P_2 = 0 \\ &(N_1 - N_2)\cos\alpha + (F_1 - F_2)\sin\alpha - W = 0 \\ &(F_1 + F_2)R = (P_1 + P_2)R \end{aligned} \tag{3.3}$$

and for the equilibrium conditions considering they are automatically satisfied in the free body diagram of Figure 3.24 b given as:

$$P_2 - P_1 - T = 0$$
$$(P_2 + P_1)R - Tb = 0 \tag{3.4}$$

By substituting eqs. (3.4) in eqs. (3.3)., the following expression for the tangential and the normal forces under a two-point contact situation is obtained.

$$F_1 = \frac{1}{2}\left(\frac{b}{R}T + W\sin\alpha - T\cos\alpha\right) \tag{3.5a}$$
$$F_2 = \frac{1}{2}\left(\frac{b}{R}T - W\sin\alpha + T\cos\alpha\right) \tag{3.5b}$$
$$N_1 - N_2 = W\cos\alpha + T\sin\alpha \tag{3.5c}$$

The above set of equations involves four unknowns (N_1, N_2, F_1, F_2) and only three equations. Therefore, another equation is needed in order to find the forces at a two point-contact situation arising from the entrapment of the wear particle agglomerate at the interface of the smooth bearing. This equation can be

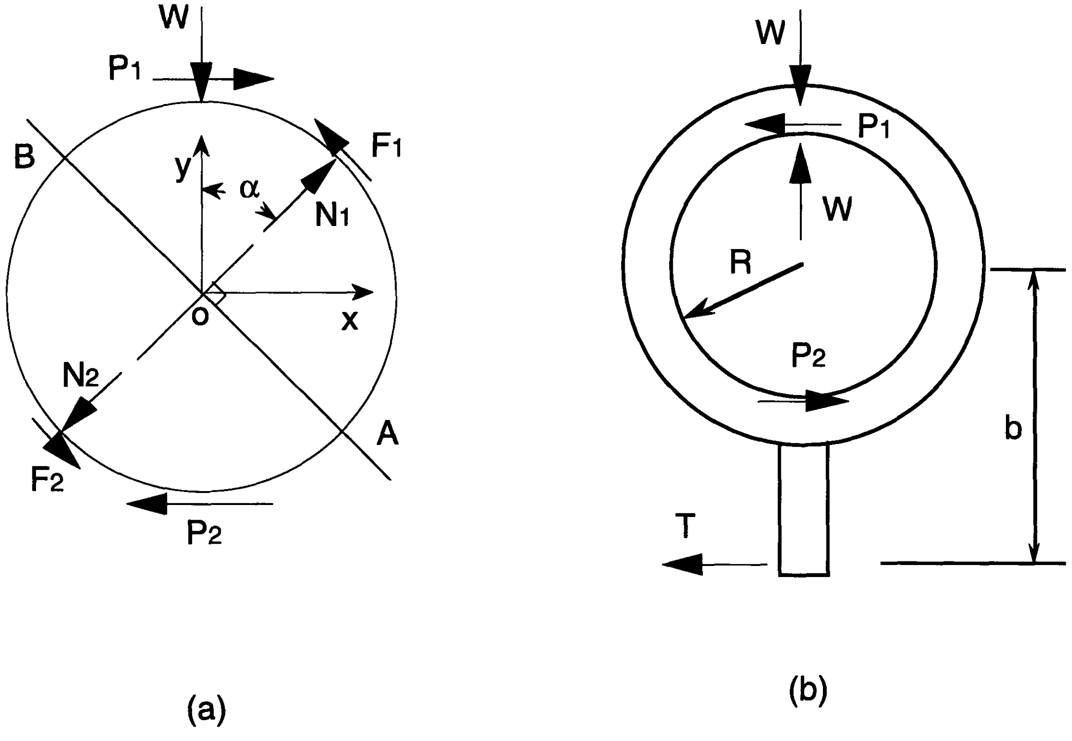

Figure 3.23 Free body diagram of the bushing and the housing.

found from the output voltage data obtained from the strain gages during the dry sliding tests. The output voltage is proportional to the hoop strain of the ring and their relationship will be analyzed in the following section.

3.4.2 Hoop Strain Analysis In Asymmetrically Loaded Thin Rings

A detailed analysis of the hoop strain under axisymmetric loading conditions is given in Appendix A. Energy methods were used to determine the internal bending moment at each section of the ring [12,13]. Only the elastic bending energy was considered and the contribution of shear and normal forces at each section to the elastic energy was considered negligible. At each section of the ring, the magnitude of the maximum strain (ε) is related to the bending moment (M) as

$$\varepsilon = \frac{6M}{Elt^2} \tag{3.6}$$

where l and t are the width and the thickness of the ring and E is the elastic modulus of the ring material.

In Appendix A, the magnitude of the bending moment in a cross-section located at any arbitrary angle is determined as a function of the loads on the ring and the magnitude of the hoop strain measured at two angles of 90 and 270 degrees from the y axis (i.e. $\eta = 90°$ in Fig. 3.14). Therefore, the total magnitude of the strains at points I and II can be related to the loads on the ring as:

$$\varepsilon_t = \varepsilon_I + \varepsilon_{II} = \frac{6}{Ebt^2}\left[\frac{1}{\pi}C_1 + N_2 R\cos\alpha - F_2 R(1-\sin\alpha)\right] \tag{3.7}$$

where C_1 is defined as

$$C_1 = -N_1 R(1-\cos\alpha) - N_2 R(1+\cos\alpha) - F_1 R(\alpha - \sin\alpha) + F_2 R(\pi - \alpha - \sin\alpha) \tag{3.8}$$

By substituting eq(3.8) in eq(3.7) one can find another equation between the tangential and the normal forces at the two contact points. However, the magnitude of total hoop strain (ε_t) must first be calculated based on the differential output voltage data obtained from the strain gages on the ring.

3.4.3 Relationship Between Differential Output Voltage of Strain Gages and Total Hoop Strain

The full-bridge configuration used to measure the strain consisted of two strain gages to measure the hoop strain and two dummy strain gages to compensate for temperature variation. The dummy gages were perpendicular to the direction of hoop strain and as a result only experienced the hoop strain multiplied by the Poisson's ratio [14].

Consider the full bridge shown in Figure 3.24 , which is initially balanced, i. e. the output voltage is initially set to zero by the use of potentiometers or by choosing correct values for the resistance of the strain gages. When the gages are subjected to strain, the incremental bridge output (δE) is determined by the expression [15]

$$\delta E = V\frac{a}{(1+a)^2}1\left[\frac{\delta R_1}{R_1}-\frac{\delta R_2}{R_2}+\frac{\delta R_3}{R_3}-\frac{\delta R_4}{R_4}\right](1-n) \tag{3.9}$$

Where n is the nonlinearity term, which will be considered negligible, V is the excitation voltage, and a is defined as $a = R_1/R_2 = R_4/R_3$. Since all the strain gages had the same resistance, the magnitude of a is one. The incremental change of the resistance of the each strain gage is related to the strain (ε) as:

$$\frac{\delta R}{R} = K\varepsilon \tag{3.10}$$

Where K is the gage factor. Therefore, the incremental output from the strain ring due to the hoop strains can be expressed as:

$$\frac{\delta E}{V} = \frac{K}{4}\left[(1+\nu)(\varepsilon_I+\varepsilon_{II})\right] \tag{3.11}$$

where ν is the Poisson ratio of the ring material.

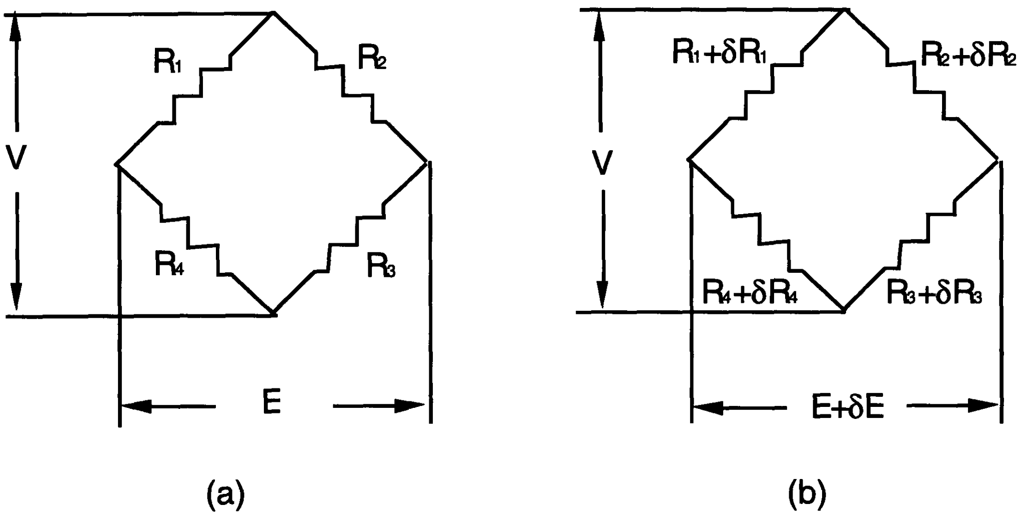

(a) (b)

Figure 3.24 Full-bridge strain gages circuit in equilibrium (a) and with an incremental output voltage due to the change in resistance.

Substituting eq. (3.11) in eq. (3.7) one can find the following expression which relates the measured differential voltage output of the strain gages to the loads, the primary contact angle, and the system parameters.

$$-N_1(1-\cos\alpha)+N_2(\pi\cos\alpha-1-\cos\alpha)=(F_1+F_2)\alpha-(F_1-F_2)\sin\alpha-F_2\pi\sin\alpha + \frac{\pi}{R}\frac{Ebt^2}{6}\frac{4}{K(1+\nu)}\left(\frac{\delta E}{V}\right) \tag{3.12}$$

Finally, by solving the set of equations given in eqs. (3.5) with eq. (3.12) one can find the following expressions for the normal forces developed in a two-point contact situation.

$$N_1=\frac{1}{\pi\cos\alpha-2}\left\{\left[\left(\alpha-\frac{\pi}{2}\sin\alpha\right)\frac{b}{R}-\frac{\pi}{2}\cos\alpha\sin\alpha+\sin\alpha+\sin\alpha(\pi\cos\alpha-2)\right]T+\left[\frac{\pi}{2}\sin^2\alpha-1+\cos\alpha+\cos\alpha(\pi\cos\alpha-2)\right]W+\left(\frac{\pi}{R}\frac{Ebt^2}{6}\frac{4}{K(1+\nu)}\right)\frac{\delta E}{V}\right\} \tag{3.13}$$

$$N_2 = \frac{1}{\pi\cos\alpha - 2}\left\{\left[\left(\alpha - \frac{\pi}{2}\sin\alpha\right)\frac{b}{R} - \frac{\pi}{2}\cos\alpha\sin\alpha + \sin\alpha\right]T + \left[\frac{\pi}{2}\sin^2\alpha - 1 + \cos\alpha\right]W \right.$$
$$\left. + \left(\frac{\pi}{R}\frac{Ebt^2}{6}\frac{4}{K(1+\nu)}\right)\frac{\delta E}{V}\right\} \tag{3.14}$$

By setting N_2 and F_2 equal to zero, the primary contact angle can be calculated at the transition from a one-point contact to a two-point contact situation from equilibrium given in eqs. (3.5). This yields

$$W\sin\alpha - T\cos\alpha = \frac{b}{R}T \tag{3.15}$$

The above analysis of normal load variation was used to calculate the forces developed at the two contact points after the transition point for 11.25 N and 45 N normal loads. Before transition, the calculation of normal force, frictional force, and the friction coefficient is made by equilibrium considerations. Figure 3.25a shows the forces developed at the primary contact point and corresponding coefficient of friction for 11.25 N normal load. The normal force after the transition (400 cycles) keeps increasing and at seizure reaches a value of about 72 N. The frictional force also has a steady increase and its maximum value is about 55 N. The friction coefficient, however, starts at a value of 0.4 and increase to a value of about 0.9 before the transition point. At the transition point, the coefficient of friction shows high fluctuations up to about 600 cycles and finally reaches a value of about 0.75 at the seizure point. At the secondary point, the normal load initially has unmeaningfull negative values. This is approximately the case from 400 to 560 cycles; after 560 cycles the model provides a realistic prediction of the normal load. At the seizure point the normal load at the secondary contact point is about 20 N.

The normal and frictional forces at the primary and secondary contact-points are shown in Figure 3.26 when the normal load was 45 N The transition occurred after 275 cycles. The normal load at the primary contact point which was originally 45 N decreased after the transition and then increased to a high value of about 85 N. The friction coefficient begins at a value of 0.3 and reaches a value of about 1 before the transition and undergoes high fluctuations at the transition and finally reaches a value of about 0.75. At the secondary contact point, as shown in Figure 3.26b, the normal force has virtually negative values between 275 and 320 cycles and subsequently increases to a high value of about 25 N.

3.5 Evaluation of Two-Point Contact Seizure Model

One important conclusion obtained from the two-point contact seizure model is that the increase in the frictional resistance of a geometrically constrained bearing operating in dry sliding is due to the increase in the normal load and not due to the friction coefficient. If point-contact equilibrium equations were used to calculate the friction coefficient, it would reach a value as high as 13 in the case of 11.25 N normal load and a value of 3.25 in the case of 45 N normal load. The reason is that the increase in the normal load will not be considered while the frictional force at the single contact point keeps increasing. In this sense, the model which has utilized the experimental results of the hoop strain on the bushing is successful.

On the other hand, the prediction of the model for the normal force at the secondary contact point yields negative values right after the transition but eventually reaches realistic positive values. This was the case for both 11.25 N and 45 N normal loads. To explain this behavior one must note the assumptions made while developing the model. First, it was assumed that from the transition point onwards the contact angle does not change. This assumption was made to simplify the problem but there is no control on this value of during the test. Its real value is known after the transition due to the complexity of a multiple contact situation. Second, it was assumed that the contacts are at two points which 180 degrees apart. However, in real situations, the contact might occur at several points instead of at two.

In order to show how close the two assumptions stated above are to reality, the initial (α)and secondary angle ($\pi + \alpha$)of contact calculated based on the model along with angle at which the maximum and minimum separation angels, i.e. α_1 and α_2 respectively, observed in the SEM of the seized bearing given in Table 3.3 are in Table 3.4 for 11.25 N and 45 N normal load. Although the diametral clearance of those bearings used in the SEM analysis was different from the bearings used in analysis of the variation of normal load, it seems that

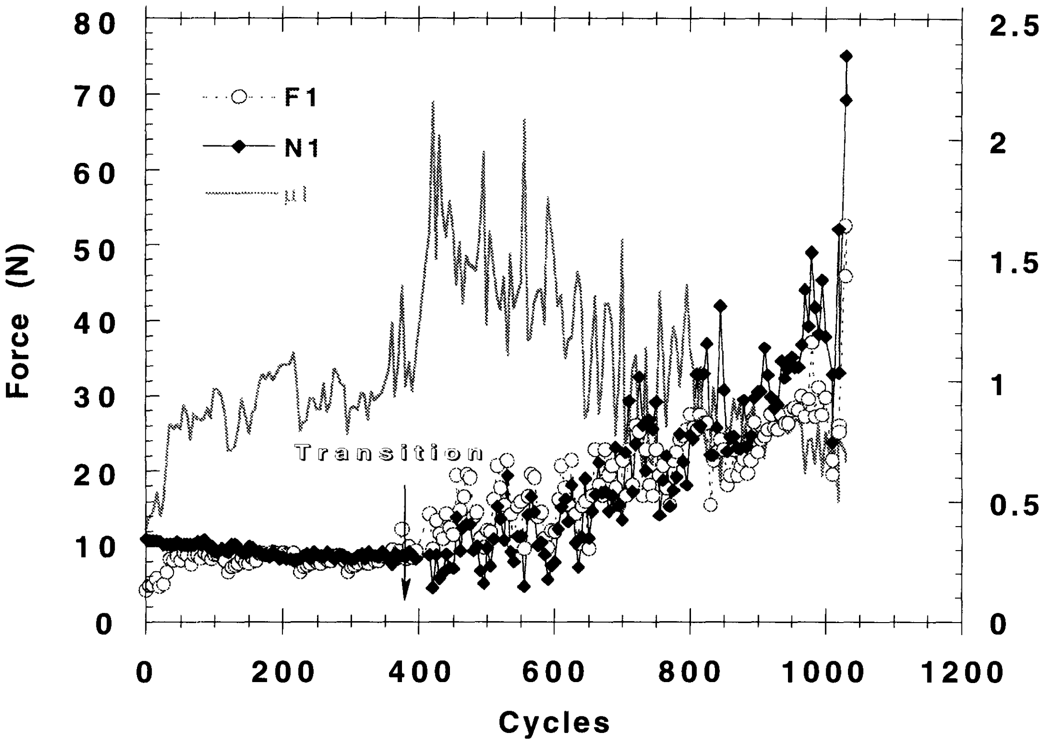

(a)

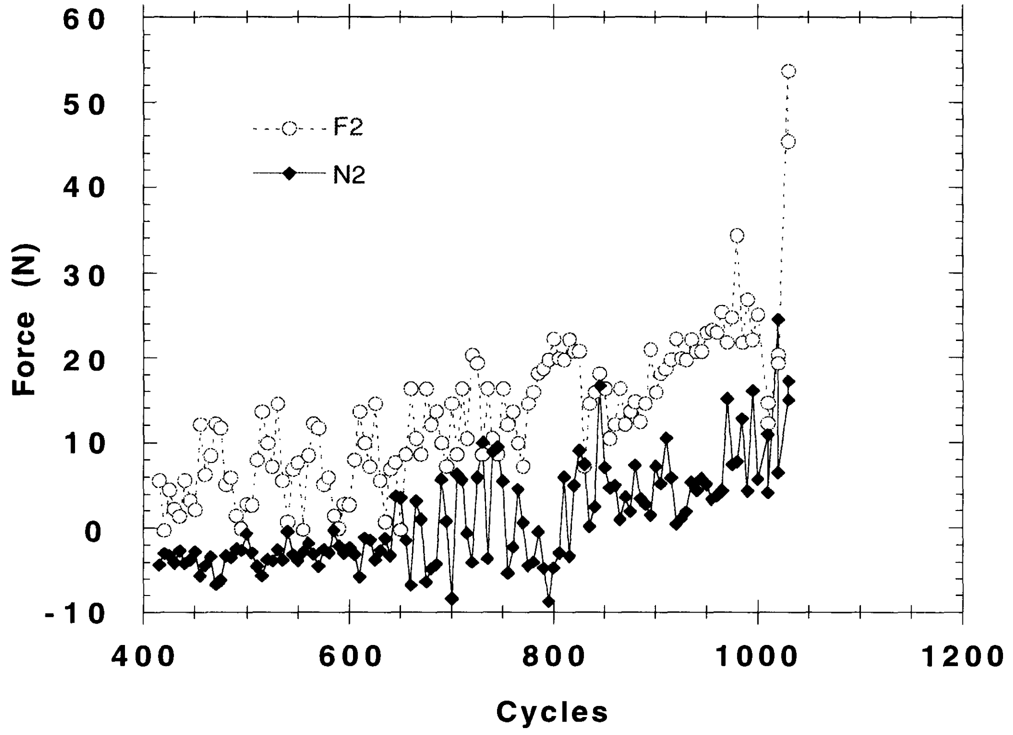

(b)

Fig 3.25 Normal and Frictional forces and friction coefficient at the primary contact point (a) and at the secondary contact (b). Normal Load= 11.25

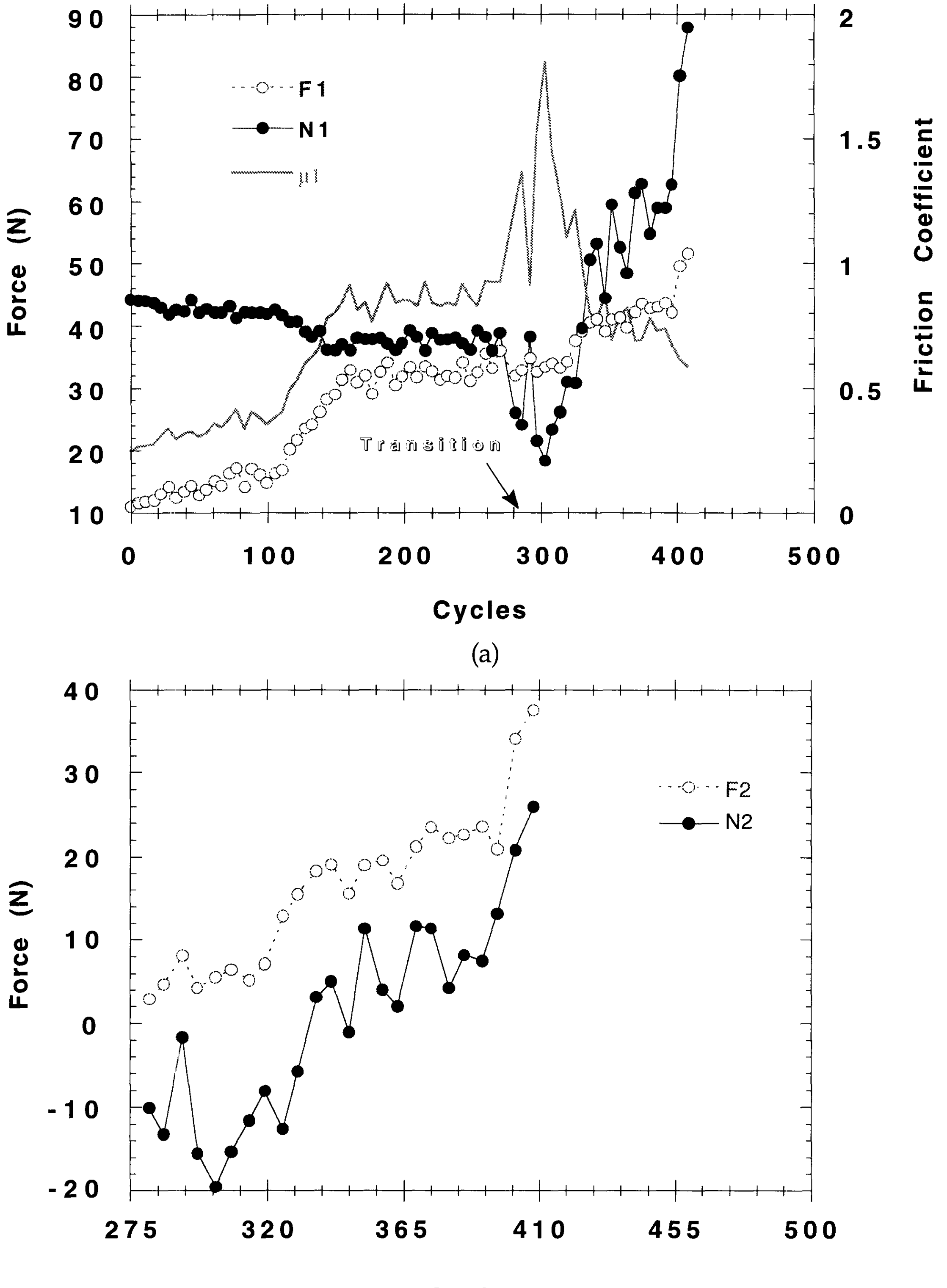

(a)

(b)

Figure 3.26 Normal and Frictional forces and friction coefficient at the primary contact point (a) and at the secondary contact (b). Normal Load= 45 N.

the angles measured in SEM fairly justify the two important assumptions made in the modeling.

Table 3.4 Comparison of the initial and secondary contact angles used in the model and the maximum and minimum separation angles obtained in SEM.

Normal Load (N)	α	$\alpha+\pi$	α_1	α_2
11.25	72	252	48	225
25	48	228	20	162

Another attempt to verify the magnitude of the secondary contact normal load was to measure the output of the strain gages after the completion of tests and the release of the seized shaft and bushing from the housing as shown in Figure 3.14. It was observed that due to the entrapment of the wear p[articles at the interface, the bushing expanded. Using the magnitude of the initial and secondary contact angles predicted by the model, the ring was calibrated to measure the loads at the two contact points. This revealed that the expansion of the bushing corresponds to 28 N and 32 N for the normal loads of 11.25 N and 45 N, respectively. The model, however, predicts an increase of 20 and 25 N in the normal load at the secondary contact point which seems to be in good agreement.

3.6 Mechanism of Normal Load Increase in Geometrically Constrained Systems and Operating Life Estimation

The model developed in the previous section enables the determination of the magnitude of the normal load at the initial and secondary contact points. However, it does not describe the tribological phenomena which cause such an increase. This phenomena can be explained based on the model developed in chapter 2 in which the geometrical constraint of the sliding systems is considered as a spring acting on the top of the agglomerate. Based on that model, the agglomeration process is assumed to involve local plastic flow of the newly formed particles which are attached to the agglomerate and global elastic deformation of the agglomerate due to the geometrical constraints. The normal load is given by

$$N(x) = N_0 + \frac{Kk_s N_0}{A_0} \int_0^{x_f} \frac{EA}{(EA + k_s h)H} dx \tag{3.16}$$

Using a wear coefficient of 1×10^{-4}, the material properties given in Table 3.1, and a spring constant of about 1×10^6 N/m, the above equation can be simplified. Also, the initial area of the agglomerate is assumed to be a circle with radius on the order of 50 μm, and its height will be the same as the bearing gap. The second term in the denominator is much smaller than the first one and can be neglected. Therefore;

$$\frac{N(x_f)}{N_0} \cong 1 + 40x_f \tag{3.17}$$

where the loads are in Newtons and the distance slid is in meters. The distance slid required to increase the normal load from 11.25 N to 72 N , as was the case shown in Figure 3.25a, is about 13.5 cm. This distance for the case of the normal load increase from 45 N to 85 N is only 2 cm, a small value.

The very small sliding distances calculated above cannot clearly be considered as the life of the bearing before seizure. Instead, enough wear particles must be produced to provide the possibility of wear particle agglomeration and their entrapment at the interface. Therefore, it can be assumed that the gap of the bearing is initially filled by wear particles and then agglomeration occurs. The distance slid required to fill the gap of a bearing, assuming that the wear particles are distributed over a width equal to its diametral clearance can be found as

$$x_i = \frac{2H\pi R}{KN_0}(C_d)^2 \tag{3.18}$$

where C_d is the diametral clearance and R is the radius of the shaft. The total distance slid before seizure will then be the sum of:

$$x_{seizure} = x_i + x_f \tag{3.19}$$

For instance, for the case of a copper bearing whose frictional torque given in Figure 3.26 with a normal load of 11.25 and a diametral clearance of 15 μm, the total distance slid will be 45 m. This translates to 470 cycles of rotations. However, the experimental value was approximately 1200 cycles. This discrepancy exists because the models presented for the increase in the normal load in a two-point contact situation give the upper bounds of the solution. Therefore, it is expected to have a much shorter life based on these predictions.

References

[1] Suh, N.P., "In pursuit of the lower limit of friction coefficient in dry sliding", ASME winter annual meeting, 1993, New Orleans.

[2] Suh, N.P. and Nagoa, T., "Implications of wear theories on surface quality and functional requirements", CIRP Annals, Vol. 25, No. 2, 1976, pp. 513-519.

[3] DeKoven, B.M., and Hagans, P.L., "Friction studies of clean and oxygen exposed Fe surfaces in Ultrahigh vacuum", Journal of vacuum Science and Technology, A, Vol. 3, No. 3, 1990, pp. 2393-2400.

[4] Bowden, F.P., and Tabor, D., "The seizure of metals", Proceeding of the Institution of Mechanical Engineers, Vol. 160, 1949, pp. 380-389.

[5] Semonov, A.P., "The phenomenon of seizure and its investigation", Wear, Vol. 4, 1961, pp. 1-9

[6] Mishina, H., Sasada, T., "Mechanism of seizure in sliding surfaces", Proceedings of the 26th Japan Congress on Materials research, 1983, pp. 154-159.

[7] Rabinowicz, E., "Friction seizure and galling seizure", Wear, Vol. 25, 1973, pp. 357-363.

[8] Oktay, S.T., The Role of Wear Particles in Dry and Boundary Lubricated Sliding, Ph.D Thesis, Mechanical Engineering Department, MIT, 1990.

[9] Suh, N.P., "The delamination theory of wear", Wear, Vol. 25. 1973, pp. 11-124.

[10] Slocum, Alexander H., Precision Machine Design, Prentice Hall, Englewood Cliffs, New Jersey, 1992, pp. 421-444.

[11] Thring, R.H., "Piston skirt friction in internal combustion engines", Proceeding of the Institution of Mechanical Engineers, London, 1989, pp. 7-11.

[12] Popov, Introduction to Mechanics of Solids, Prentice-Hall, Inc., Englewood Cliffs, N.J., 1968.

[13] Crandall, S., Dahl, N., and Lardner T, An Introduction to the Mechanicas of Solids, McGraw-Hill Publishing Company, New York, N.Y., 1978.

[14] Cook, N.H, and Rabinowicz, E., "Physical Measurement and Analysis", Addison-Wesley Publishing Company, Inc., 1963.

[15] Perry, C.C., and Lissner, H.R., "The Strain Gage Primer" , Second Edition MacGraw-Hill, Inc. New York, 1955.

Chapter 4

Dry Friction of Geometrically Constrained Systems in High Vacuum and High Temperature Environments

4.1 Introduction

Friction as a surface phenomenon is sensitive to any environmental conditions which alter the state, properties and characteristics of the surface layer. The surfaces of most materials studied in tribology have physically and chemically adsorbed films resulting from exposure to the atmosphere. The properties and characteristics of such films depend on their exposure to the environment which affects the tribological behavior of surfaces in contact. In particular, high vacuum and high temperature, especially when combined, greatly change the adsorption of surface contaminants and the thermodynamics and kinetics of oxidation. Furthermore such environments limit the possibility of using a lubricant due to the volatility of liquid lubricants. On the other hand, the development in the field of space engineering and plasma engineering requires the design of durable sliding mechanisms which can operate effectively in high vacuum and/or high temperature. The importance of the successful operation of such sliding mechanisms might be better appreciated if one thinks of the consequences of the failure of a simple bearing in an spacecraft which cannot be retrieved for repair. This was the case for the spacecraft Gallileo whose antenna opening mechanism failed to operate due to the seizure of a simple bearing.

The development of liquid lubricants for space applications has been the focus of research as a means to provide low friction, long lasting bearings which can operate in high vacuum [1,2]. The performance of these lubricants largely depends on the temperature at which they operate. An important property is the lubricant volatility in vacuum, a property which has a strong temperature dependence. Many currently used liquid lubricants such as paraffinic mineral oil (PMO) and Silahydrocarbon (SiHC) have been shown to be highly volatile at temperatures beyond $300\,^{\circ}C$ even at a relatively high pressure of 60 Pa [3]. The evaporation of such lubricants causes an increase in the viscosity and subsequently higher friction.

Another focus of research in aerospace bearing development has been the tribological behavior of soft and thin films as solid lubricants. Polymer-based self lubricating composites tested against smooth alumina have shown improvement in friction and wear and are considered candidates for high vacuum application [4]. Molybdenum disulfide (MoS_2) is also used as a solid lubricant in aeronautical and space applications because of its low friction coefficient and high environmental stability in dry and vacuum conditions [5-8]. The low friction coefficient and low wear of MoS_2 is believed to be a result of its layered structure which allows the orientation of the closed-packed planes parallel to the interface. Metal based hot-pressed composites such as a composite made of MoS2 , molybdenum oxide and refractory metals have shown friction coefficients as low as 0.1 and a low wear rate in vacuum of 10^{-4} Pa up to temperature of $450\,^{\circ}C$ [9].

In this study, the approach taken toward the development of a low friction and long-life sliding mechanism for high temperature and high vacuum is one of surface engineering design. This approach can be used in parallel with other solutions and designs to introduce a new generation of sliding bearings which can be used in regular as well as special environments. Initially the effects of high vacuum/high temperature on friction of geometrically constrained systems are investigated. The emphasis is on the augmented role of mechanical interactions such as agglomeration and plowing by wear particles caused by the environment. Then the effectiveness of undulated surfaces in removing wear particles from the interface will be addressed.

4.2 Tribological Effects of Adsorbed Films

When a gas is allowed to come into equilibrium with a solid surface, the concentration of gas molecules near the surface is always higher than in the free gas phase. The process by which this surface excess forms is known as adsorption [10,11]. Depending on the nature of the driving forces involved, adsorption can be physical or chemical. The former is caused by molecular interaction forces and occurs in any gas-solid system provided that the conditions of temperature and pressure are suitable. The later, however, involves a transfer of electrons between the adsorbent and the adsorbate which leads to the formation of chemical compounds such as oxide layers at the outermost layer of the solid surface. The removal of the physisorbed films from the surface of a solid can be achieved by reducing the pressure and/or increasing the temperature. The desorption rate is generally fast except when the diffusion of impurities from within the substrate occurs. The removal of a chemisorbed layer especially on metal surfaces, however, often requires more harsh conditions such as very high temperatures. The removal can also be accomplished through ion or electron bombardment under low pressure.

In recent years much effort has been devoted towards obtaining clean metal surfaces. The objective of many of these attempts has been to gain a better understanding of the effect of various surface properties of metals on the mechanical behavior. The tribological and electrical behavior of surface films have been studied in areas such as: prevention of damage to magnetic head/disk systems caused by stiction [12,13], the effects of surface films on scanning tunneling microscopes (STM) and atomic force microscopes (AFM) [14,15], and the optimization of sliding conditions for high-current-density collectors [16]. Among all adsorbed films, the most common films, water vapor and oxygen, have been the focus of research in tribology because of their effect on friction and wear. Other surface films such as nitrogen, carbon dioxide, hydrogen generally have not shown a significant change in the friction coefficient even in well controlled environments [17]. Oxygen and its chemical reaction with surfaces in formation of oxide layers has been known to alter the friction and wear of metals. This will be discussed later in section 4.3.

The effects of water vapor films on friction has been addressed in the literature, especially with respect to stiction phenomenon [18]. In general, higher humidity has been shown to reduce the mean friction coefficient [17]. The necessary environmental conditions to evaporate water vapor films from sliding surfaces has been shown to be a vacuum of about 5×10^{-7} Pa at room temperature [19]. At higher temperatures and at the same or lower vacuum levels, such films cannot be adsorbed to provide lubrication.

The high vacuum and/or high temperature conditions, i.e. vacuum of 5×10^{-8} Torr in room temperature and that of 10^{-6} Torr at higher temperature experiments in this study, will eliminate much of the weak physisorbed films from the interface. The removal of such films might allow better bonding of the wear particles as they agglomerate and cause increased friction from the plowing point of view.

4.3 Oxidation and its Influence on Friction and Wear

Oxidation of materials is among the simplest chemical reactions; however, they are of great engineering importance. From the tribology point of view, the existence of oxide layers on almost all metals and their removal during sliding has been widely investigated. The emphasis of this research is to characterize the effects of such films on the formation of large wear particle agglomerates. This includes examining the effects of localized removal of the film and how it changes the frictional behavior of geometrically constrained sliding systems. Since the experimental work in this chapter is performed at high temperature and in high vacuum, the effects of each will be reviewed.

The chemical reaction of a metal M with oxygen to form the oxide M_aO_b can be written as [20]:

$$aM + \frac{b}{2}O_2 \rightarrow M_aO_b \tag{4-1}$$

The driving energy of the reaction is the free energy change associated with the formation of the oxide from the reactants. The change in the Gibb's free energy for the above reaction can be written as:

$$\Delta G = \Delta G^\circ + RT\ln\frac{r_{M_aO_b}}{r_M^a r_{O_2}^{b/2}} \tag{4.2}$$

where ΔG° is the change in Gibb's free energy with species in standard states and r the activity of species. Also R is the gas constant and T is the temperature in K. Thermodynamically, the formation of oxide will occur if the change in the Gibb's free energy of the reaction is negative $(\Delta G\langle 0)$. In another words, the oxide will be formed if the ambient oxygen pressure is larger than the dissociation pressure of the oxide in equilibrium with the metal:

$$p(O_2)\rangle \exp\left(\frac{2\Delta G^{\circ}(M_aO_b)}{bRT}\right) \tag{4-3}$$

Such free energy data and the dissociation pressures of oxides as a function of temperatures are conveniently summarized in the Ellingham-Richardson diagram shown in Figure 4.1. In this diagram, constant partial pressures of oxygen are given by straight lines connecting the origin at the top left such as the line corresponding to $p(O_2) = 10^{-20}$ atm. For instance at 750 $^{\circ}C$ the dissociation pressure of Fe_2O_3 is 10^{-10} atm (7.6×10^{-8} Torr) while that of FeO is 10^{-20} atm (7.6×10^{-18} Torr). For copper oxides using eq. (4.2) it can be shown that the corresponding partial pressures of oxygen at 750 C for the formation of CuO is 6.5×10^{-11} atm (5×10^{-8} Torr) while that of Cu_2O is 2.5×10^{-14} atm (1.9×10^{-11} Torr). These pressures are much lower than the level of vacuum used in this study. Therefore, the oxidation of both materials in the following experimental work is unavoidable. However, the rate of oxidation needs to be compared to the wear rate in order to find out whether or not the formation of an oxide layer will continue during sliding.

A comparison between the wear rate and the rate of growth of the oxide layer can be made assuming that a slider moves over a disk in a circular path whose passage time is t^*. The depth of removal of the material as a result of wear (h_w) can be determined using the wear equation:

$$h_w = \frac{KLv}{\pi DlH} t^* \tag{4-4}$$

where K is the wear coefficient, H is the hardness, L is the normal load, and v is the sliding speed. Also l is the characteristic dimension of the real area of contact. The rate of growth of the oxide scale based on the Wagner theory of oxide growth [20] can be expressed as a parabolic function of time. The oxide thickness (h_o) will then be:

$$h_o = \left(k_p t^* + C\right)^{1/2} \tag{4-5}$$

where k_p and C are the parabolic and the integration constants. The competition between the rate of removal of the material and the rate of oxidation will determine if at the steady state of sliding, pure metal-to-metal contact will occur. This condition occurs when $h_w \rangle h_o$.

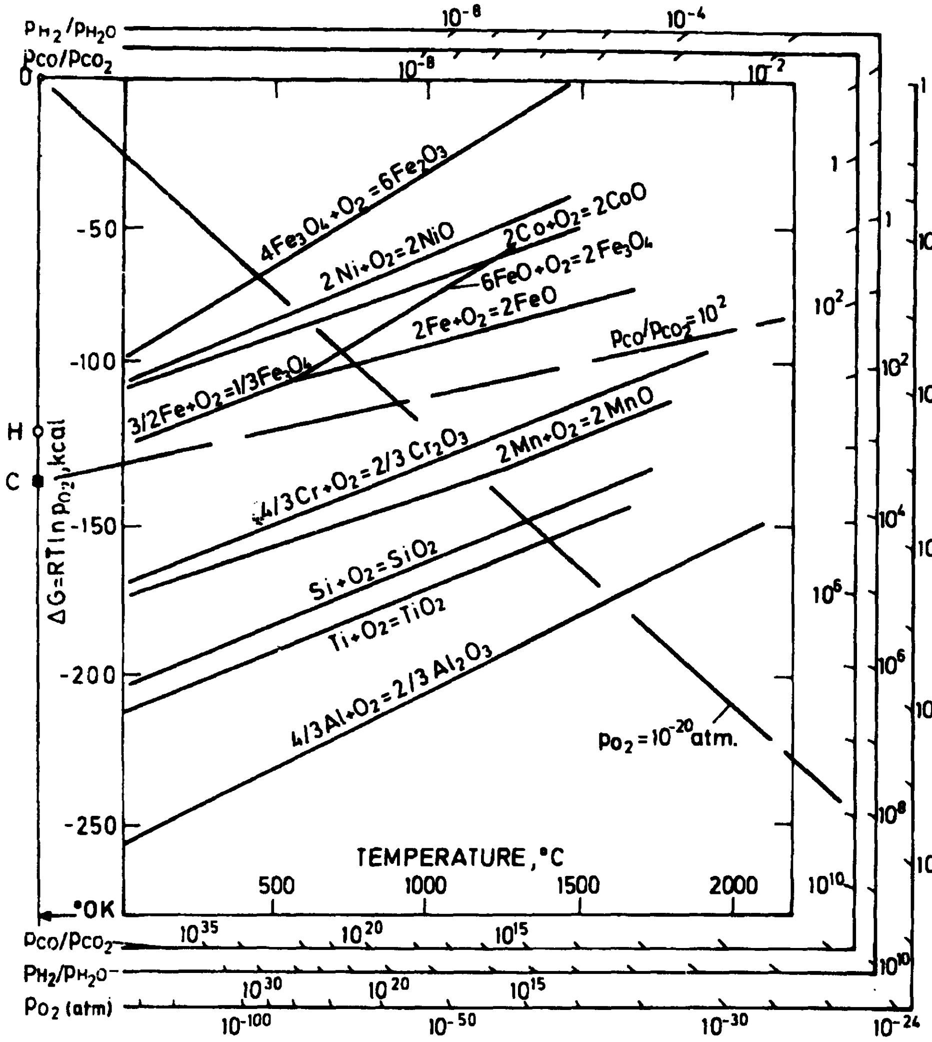

Figure 4.1 Ellingham-Richardson diagram illustrating the stability of various binary metal oxides as a function of temperature.

The effect of the presence of an oxide layer on friction and especially on wear has been studied by numerous researchers [21-24]. The general conclusion of research is that the existence of such a film reduces friction and wear. This is true provided that the oxide layer is not removed during sliding or its formation rate is higher than its removal rate due to the wear process. However, in a typical engineering application where the normal load is not extremely low such films have been shown to break and the wear rate is consequently much higher than the oxidation rate [25,26]. This is the case for many sliding situations even in atmospheric conditions in which the supply of oxygen from the environment is unlimited. When the supply of oxygen is limited due to its low pressure, partial or complete metallic contact is unavoidable.

The explanation of the frictional behavior of metals having oxide layers is inconsistent in the description of the transition that takes place from low to high friction regimes. This transition has been explained by some researchers in terms of the removal of oxide layers and the occurrence of direct metal-to-metal contact [27]. This was shown to be invalid and the mechanism for such transition was instead shown to be plowing by wear particles [28]. Since wear particles at the interface agglomerate and form larger particles it is plausible that when environmental conditions promote the formation of "clean" wear particles (i.e., free from oxide layers), the agglomeration process will be accelerated. Furthermore, the strength of a wear particle agglomerate in the absence of physisorbed and chemisorbed films will increase. In fact, pressure welding studies have shown that the existence of surface films, especially oxide films reduce the strength of pressure welded parts significantly [29].

4.4 Augment of Consolidation of Wear Particles by High Vacuum, High Temperature Environment and Geometrical Constraints

The agglomeration of wear particles at the interface of a sliding system is affected by the surface film on the individual wear particles. Furthermore, the compressive force on the agglomerate which carries the normal is the driving force for agglomeration. Therefore, a geometrically constrained sliding system operating in a high vacuum and high temperature can be considered as the most desirable system for agglomeration. On one hand the normal force is increased because of the constraints, while on the other hand, the consolidation of wear particles is increased due to higher adhesion as a result of the removal of surface films. In the following model the second condition will be termed the "sticky" condition.

The consolidation of newly formed wear particles into the existing agglomerate can be considered the mechanism by which wear particles are entrapped at the interface. The process is analogous to the cold compression of metal powders. Similar to a model proposed for the coining process of metal working [30], asperities on newly exposed surfaces on wear particles plastically deform and conform to the surface asperities of the growing agglomerate as shown in Figure 4.2. Due to the work hardening of the agglomerate as a result of continued sliding the deformation of the agglomerate asperities is much less than those of the newly formed wear particles. The penetration depth of the asperities into each other which cause an increased contact area between particles determines the strength of the entire agglomerate. A sufficient binding strength must be reached so that newly formed particles joining the agglomerate can resist the shear stresses which tend to break up the agglomerate. This process of agglomeration was proposed for open sliding systems [31]. The binding strength boundary conditions assumed in the model might apply well to high vacuum and high temperature agglomeration.

Assuming that the interparticle strength σ_a is proportional to the amount of penetration between asperities, σ_a, is given by:

$$\sigma_a = \sigma_{ys}\left\{1 - \exp\left[\frac{\left(-\sqrt{3\pi/4}\right)\dfrac{p_{ave}}{\sigma_f} + \left(b_1\dfrac{R\tan\alpha}{t} + c_1\right)}{3a_1}\right]\right\} \tag{4.6}$$

where p_{ave} is the average compacting pressure, σ_{ys} the yield strength of the bulk, σ_f the average flow strength, α the half-asperity angle t the wear particle thickness, R the peak-to-valley roughness, L the distance between two asperities. The other constants, i.e. a_1, b_1, c_1, ϕ are given by:

$$a_1 = \pi/4 - 0.5\arcsin\phi + \phi\left(1 - 0.5\sqrt{1-\phi^2}\right) \tag{4.7a}$$

$$b_1 = -\pi/2 + \arcsin\phi + \frac{1}{3}\left(2\phi^{-1} + \phi\right)\sqrt{1-\phi^2} \tag{4.7b}$$

$$c_1 = \pi - 2\arcsin\phi - 2\phi\sqrt{1-\phi^2} \tag{4.7c}$$

$$\phi = (R/L)\tan\alpha \tag{4.7d}$$

The compacting pressure on the agglomerate in a constrained sliding system will not remain constant as in an unconstrained system. Instead, it can be shown by an analysis similar to that used in Chapter 3 that the pressure on the agglomerate will increase when the growth of the agglomerate at the interface is constrained. Assuming a global elastic analysis of the agglomerate one can find that the average pressure of the agglomerate will be:

$$p_{ave}(x) = p_0\left(1 + Kk_s\int_0^{x_f}\frac{E}{(EA+k_sh)H}dx\right) \tag{4.8}$$

where p_0 is the average pressure if the system were unconstrained is equal to the external normal load divided by the agglomerate cross section.

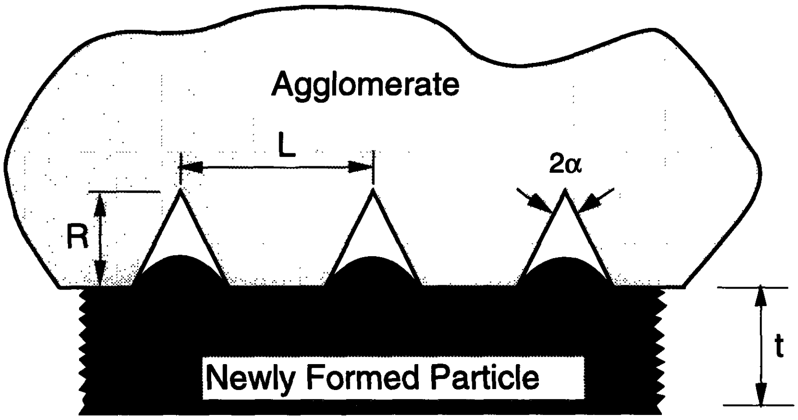

Figure 4.2 Consolidation of newly formed particles into the existing agglomerate using a coining model.

To make a comparison between the constrained and unconstrained systems we can use the experimental numerical values obtained in Chapter 3 for the increase in the normal load in the bearing tested under a 11.25 N normal load. Assuming that the increase in pressure in the constrained system was about five times that of the unconstrained system and using eq. (4.6) we see that:

$$\frac{\sigma_{a_{constrained}}}{\sigma_{a_{unconstrained}}} = 8.5 \tag{4.9}$$

The values used in calculating the above ratio are $\alpha = 60^{\circ}$ for the asperity half angle, $R/t = 0.01$ for the groove depth-to-wear particle thickness ratio, $\phi = 0.5$ for the ratio between the groove width and its pitch, and $\sigma_f = 200$ MPa for the average flow stress at 300 C. The values of constants a_1, b_1, and c_1 from eqs. (4.7) are 0.8071, 0.2518, and 1.2284 respectively.

4.5 Experimental Apparatus and Procedure

4.5.1 Friction tester and Vacuum system

The bearing tester used to carry out experiment results is shown schematically in Figure 4.3. This tester is designed to study the friction of sliding bearings when a counterweight is applied to the system. A counterweight tends to tilt the bushing with respect to the shaft, resulting in two-point contact between the shaft and bushing.

The main part of the friction tester is a single piece housing and extended arm. The test bushing is secured to the housing, which is then placed on a gimbal. The gimbal allows free rotation about any of the three orthogonal axes that pass through its center. The housing can be moved vertically by use of a rack and pinion mechanism. The test shaft is connected to the main spindle, which is precisely aligned with the center of the gimbal. When the housing and test bushing are moved upward, the shaft and the bushing engage each other, limiting the motion of the housing to rotation about the vertical axis. A band heater, surrounded by a molybdenum sheet to prevent radiation to the environment, is installed around the housing which can raise the temperature of the shaft up to $400\,^{\circ}C$. The temperature of the shafts is monitored using a thermocouple installed on the oscillating shafts.

A balancing arm with a movable weight is located along the axis of the extended arm on the side opposite the housing. The balancing arm and weight are used to balance the housing/bushing system with respect to the center of the bushing. After balancing, a counterweight is applied on the extended arm at a fixed distance from the center of the bushing.

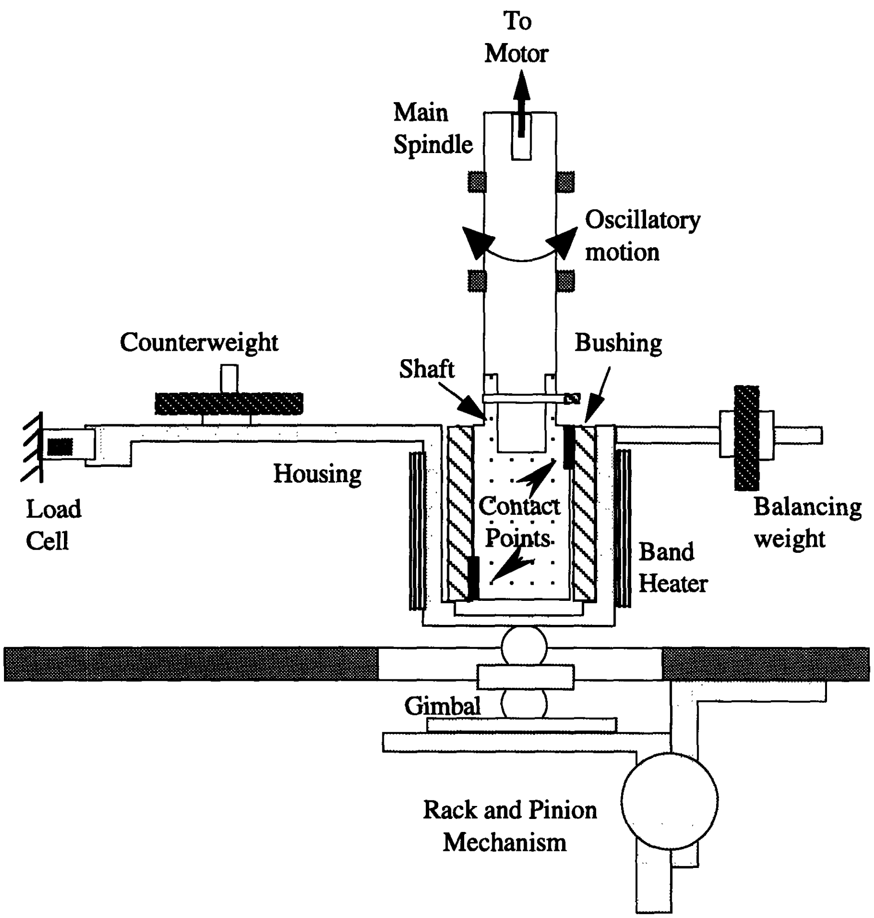

Figure 4.3 Schematic of the friction tester for sliding bearings under two-point contact loading.

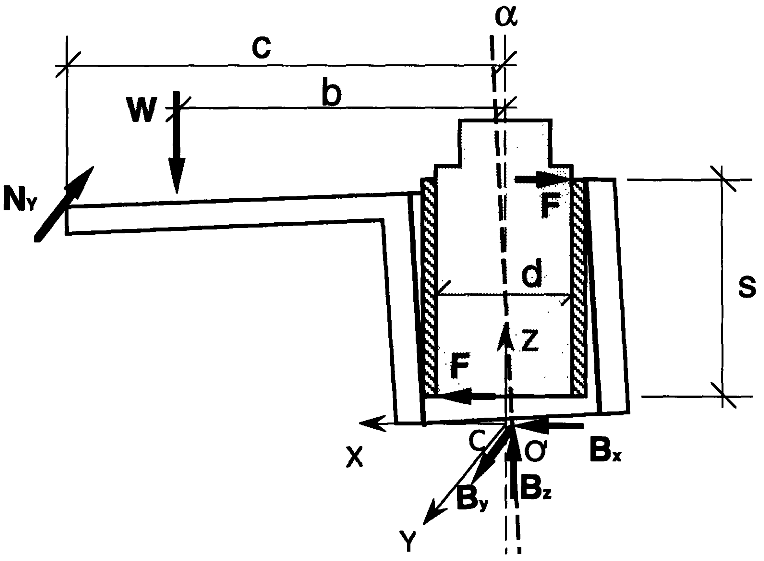

Figure 4.4 Free body diagram of the shaft/bussing assembly in the housing showing the external and internal forces.

During the experiment, a cantilever beam instrumented with strain gages prevents the housing from following the motion of the shaft. Since the signal from the strain gages is proportional to the force applied to the cantilever beam, the torque applied to the housing is known. The frictional force on the bushing is then calculated from this value of the torque and the system geometry shown in Figure 4.4. Since the maximum tilting angle α in this study is on the order of 0.001 rad, its effect on the moment balance equations was neglected. Taking moments about the Y and Z axes gives

$$Wb = Fs \tag{4.10a}$$

$$N_y c = \mu F d \tag{4.10b}$$

where

W : counterweight
N_y : measured force
F : contact normal force developed at the bearing interface
$s.\ b,\ c$: dimensions given in Figure 4.4
d : shaft diameter
μ : friction coefficient

So the friction coefficient can be determined as:

$$\mu = \frac{N_y c}{Wbd} \tag{4.11}$$

The tester was put in a vacuum chamber shown in Figure 4.5 with minimum pressure of 6.5×10^{-6} Pa (5×10^{-8} Torr). The rotary back-and-forth motion was produced using a four bar linkage mechanism with three different amplitudes of 20, 30, and 40 degrees.

4.5.2 Materials

The bushings used in this experiment were made of stainless steel 304 , a stainless steel that is commonly used in vacuum applications. All of the shafts were made of titanium diboride dispersion strengthened copper (MXT3). The mechanical properties of the stainless steel 304 and the copper are given in Table 3.1.

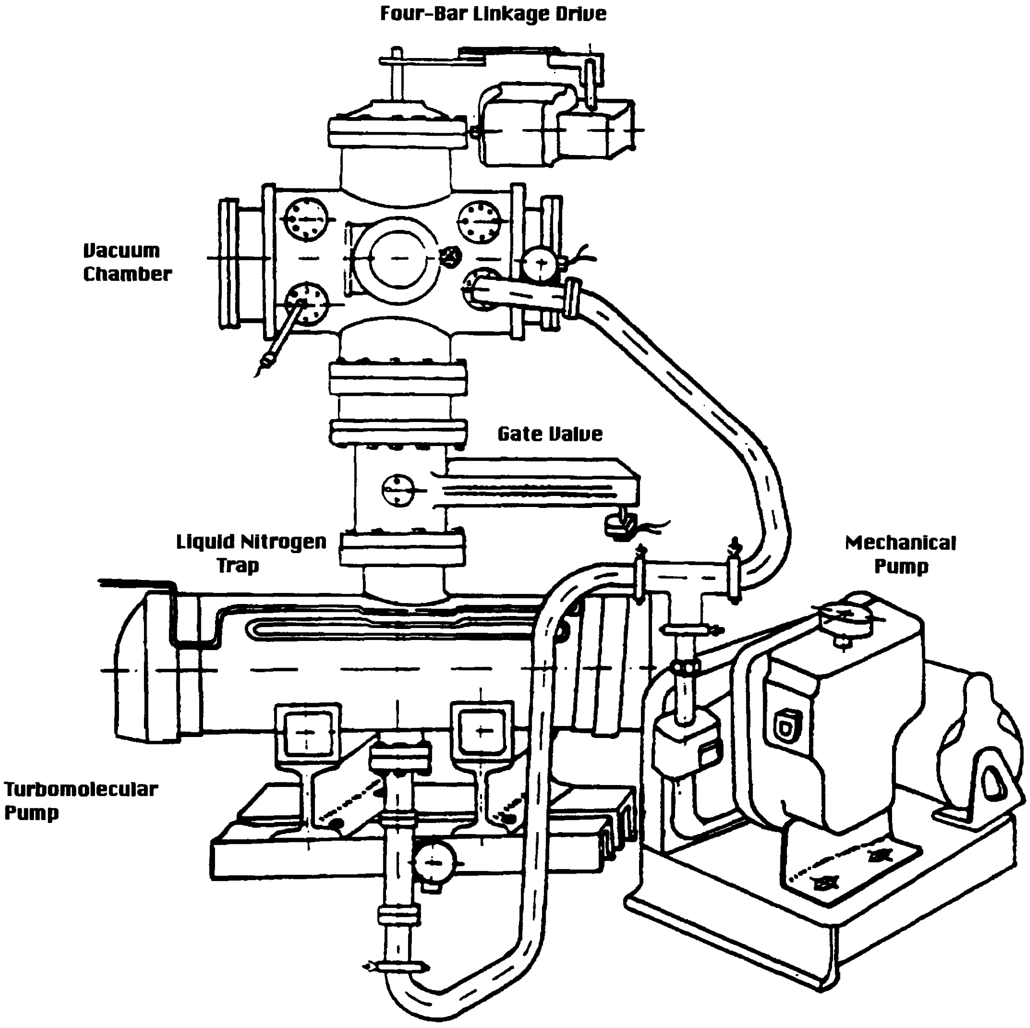

Figure 4.5 General view of high vacuum system (6.5×10^{-6} Pa).

4.5.3 Fabrication of Smooth and Undulated Bearings

Smooth shafts and bushings were turned on a lathe and ground to size with a tolerance of 2.5 μm (0.0001 inches.). The inner diameter of the bushings was always $3.175^{+0.00025}$ cm ($1.25^{+0.0001}$ inches), while the outer diameter of the shafts was varied in order to study the effect of bearing clearance. The RMS and peak-to-valley roughness of the ground surfaces were in the range 60 to 100 and

600 to 800 nm, respectively. The bushings seemed to have slightly smoother surfaces because of their higher hardness as shown in Figure 4.6.

Undulations on shafts were made by machining process described in section 3.3.1.3 and their nominal and machined size are given in Figures 3.5 and 3.6.

4.5.4 Experimental Conditions

Test samples were ultrasonically cleaned, rinsed with acetone, ethyl alcohol, and isopropyl alcohol prior to each experiment. The counterweight for all experiments was 1.45 N. This corresponds to a 2.50 N normal load between the shaft and the bushing at the two contact points. The amplitude of rotation during all tests was 30 degrees and the shaft's frequency was 0.83 Hz. The maximum duration of each experiment was 20,000 cycles at room temperature and 10,000 cycles at high temperature unless the bearings seized before these upper limits were reached. The distance slid in each cycle was approximately 1 cm. Experiments were conducted in air and at room temperature, in vacuum and room temperature and finally in vacuum and at high temperatures.

4.6 Results

As a first step toward estimating the accuracy of the experimental data, the frictional behavior of a bearing was examined without a counterweight. If the system is balanced, this should result in zero frictional force between the shaft and the bushing. However, experiments showed that a contact normal force of about 0.1 N was developed at the shaft/bushing interface. Since the typical value of the frictional force in this study is about 2 N, this corresponds to an error of about 5 percent.

Since the sliding at the interface is a rotary oscillatory motion, the frictional force measured by the force measurement unit changes its sign from positive to negative. Two friction coefficients shown in the "negative" and "positive" parts of the friction coefficient plots correspond to clockwise and counterclockwise rotation of the shaft, respectively.

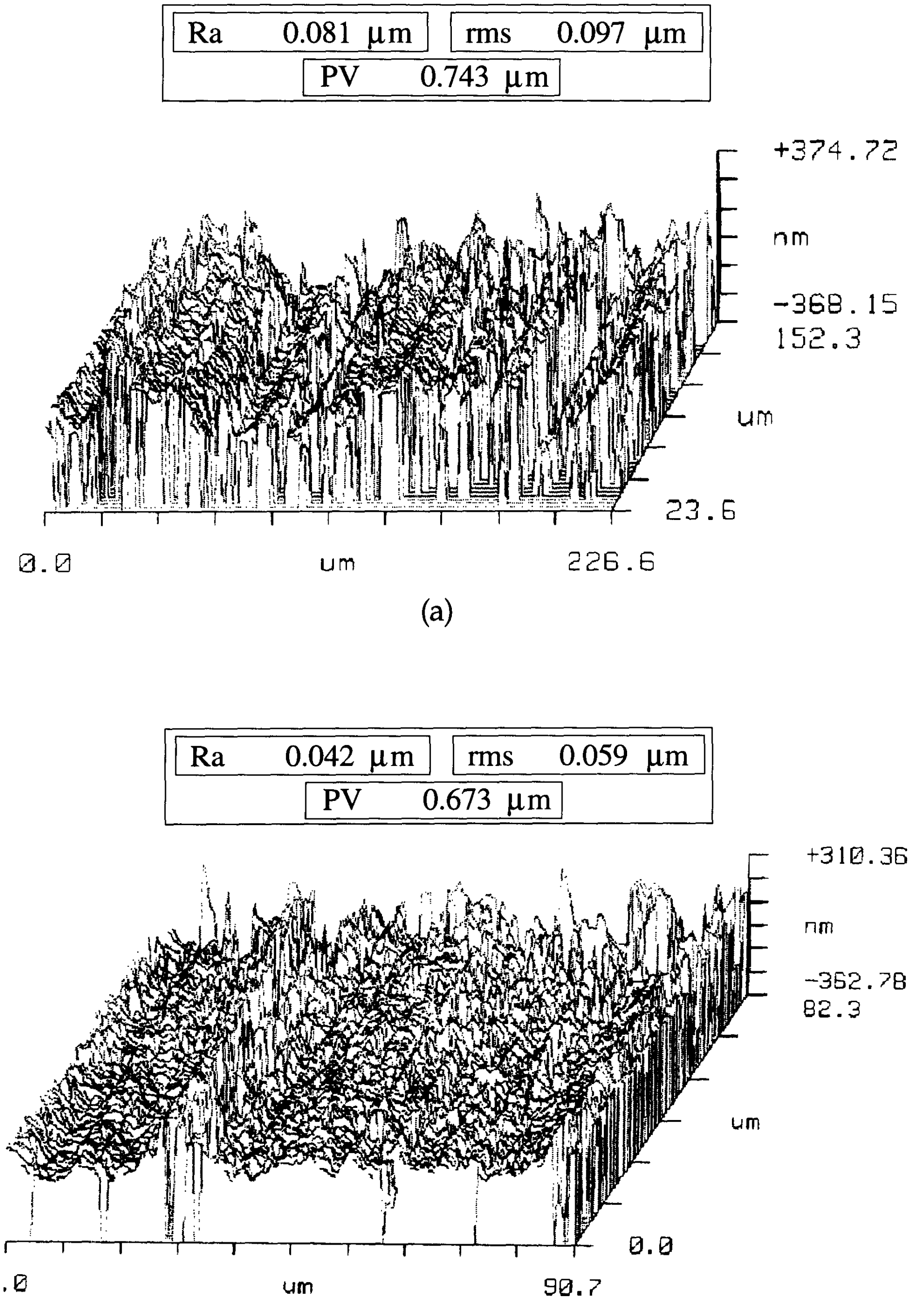

Figure 4.6 Digital image of the surface profile of the copper shafts (a) and the stainless steel bushings (b).

4.6.1 Results Obtained in Air at Room Temperature

Figure 4.7 shows the friction coefficient of smooth and undulated bearings with a diametral clearance of 100 μm tested in air at room temperature. The friction coefficient starts at a value of 0.25 for both bearings, but increases to a higher steady state value of 0.75 for smooth bearings. On the other hand the undulated bearing exhibits a friction coefficient of about 0.25-0.3 throughout the test. As the diametral clearance of the bearing decreases, the steady state value of the friction coefficient of smooth bearings increases while the initial value remains unchanged, as shown in Figures 4.8 and 4.9 for diametral clearances of 25 and 12.5 μm, respectively.

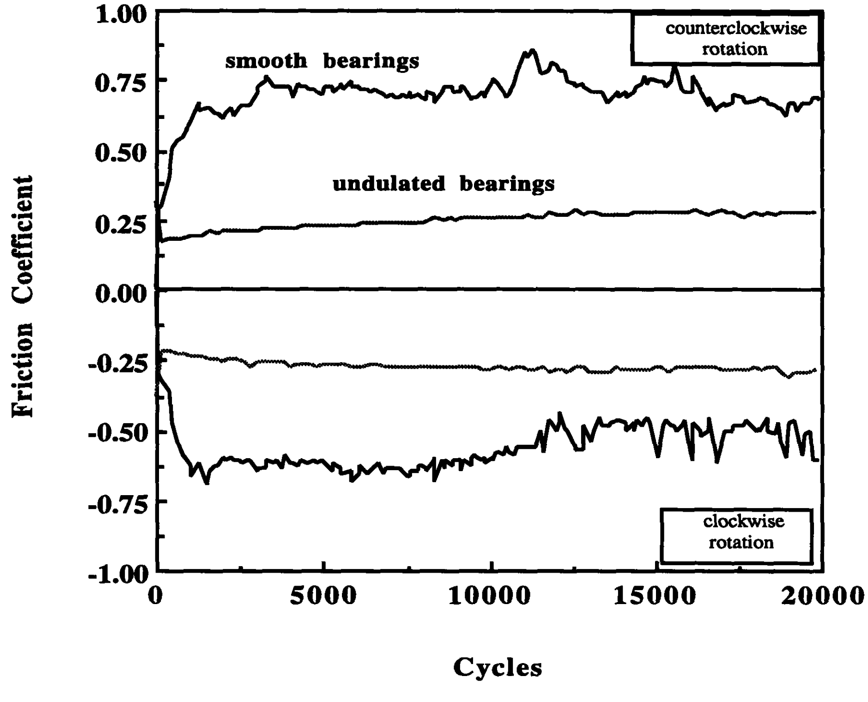

Figure 4.7 Friction coefficient of smooth and undulated bearings tested in air at room temperature with a diametral clearance of 100 μm. Normal Load= 2.5 N

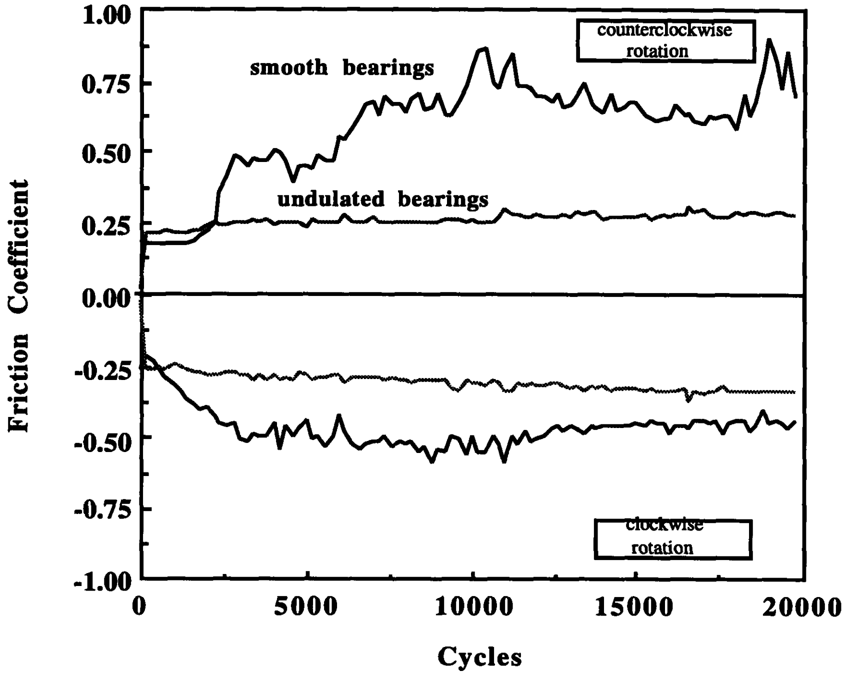

Figure 4.8 Friction coefficient of smooth and undulated bearings tested in air at room temperature with a diametral clearance of 25 μm. Normal Load= 2.5 N

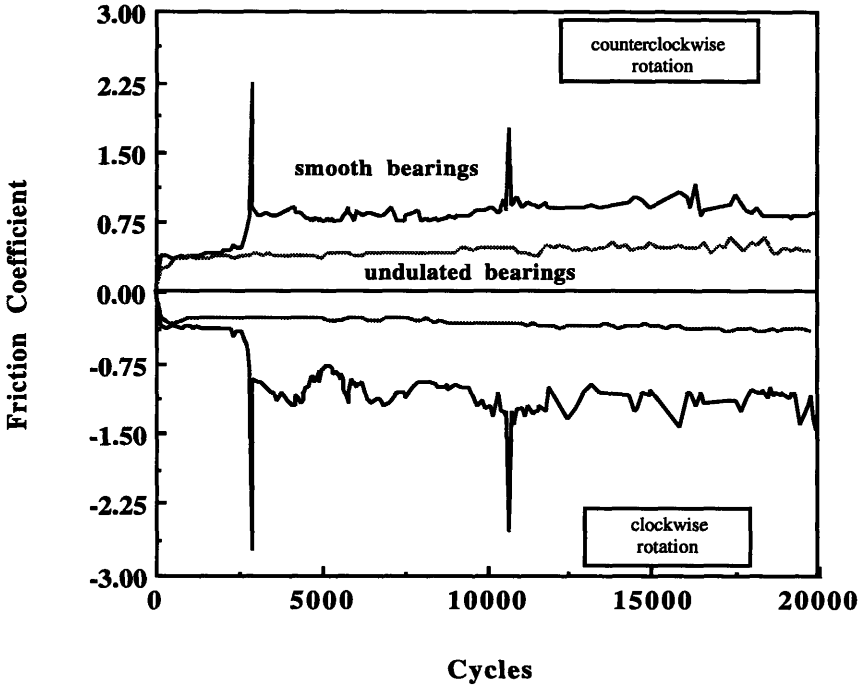

Figure 4.9 Friction coefficient of smooth and undulated bearings tested in air at room temperature with a diametral clearance of 12.5 μm. Normal Load= 2.5 N

Occasional spikes in the friction coefficient of smooth bearings can be seen when the diametral clearance reaches extremely low values, possibly leading to complete seizure, as shown in Figure 4.9. On the contrary, the friction coefficient of undulated bearings remained insensitive to the diametral clearance and did not show a noticeable increase from the initial low value of 0.25.

4.6.2 Results Obtained in Vacuum at Room Temperature

The frictional behavior of smooth surfaces in high vacuum is highly dependent on the diametral clearance of the bearing. However, for undulated bearings such dependence was not observed. Figure 4.10 shows the friction of a smooth and undulated bearings with a clearance of 100 μm tested in a high vacuum of 6.5×10^{-6} Pa (5×10^{-8} Torr). Both bearings exhibit the same friction coefficients obtained with the same diametral clearance in air, namely about 0.8 for smooth and about 0.3 for undulated bearings. In a smooth bearing with a diametral clearance of 25 μm, the friction coefficient is about 1 for up to 13000 cycles then show a sudden increase, as shown in Figure 4.11.

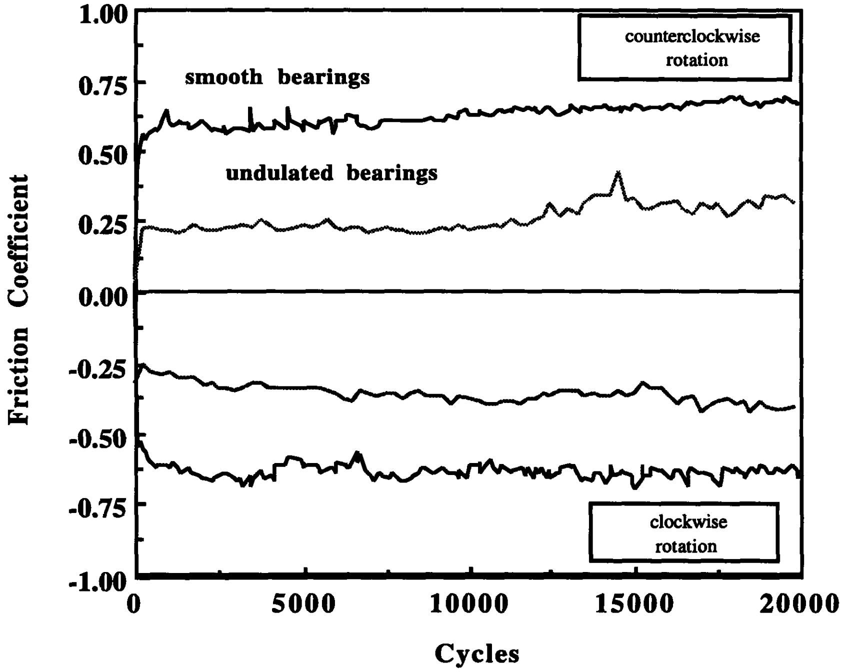

Figure 4.10 Friction coefficient of smooth and undulated bearings in vacuum of 6.5×10^{-6} Pa at room temperature. Normal Load= 2.5 N, Cd= 100 μm.

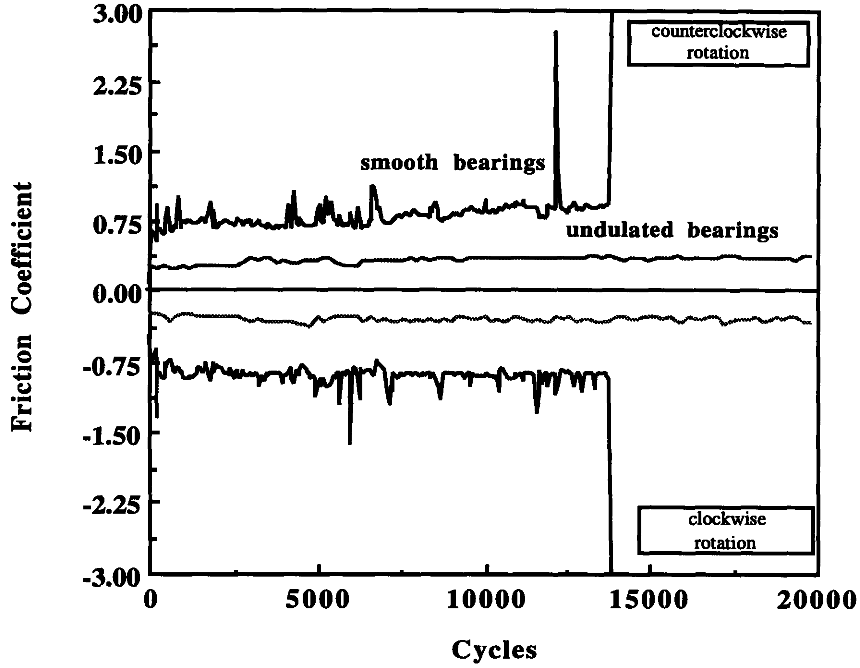

Figure 4.11 Friction coefficient of smooth and undulated bearings in vacuum of 6.5×10^{-6} Pa at room temperature. Normal Load= 2.5 N, Cd= 25 μm.

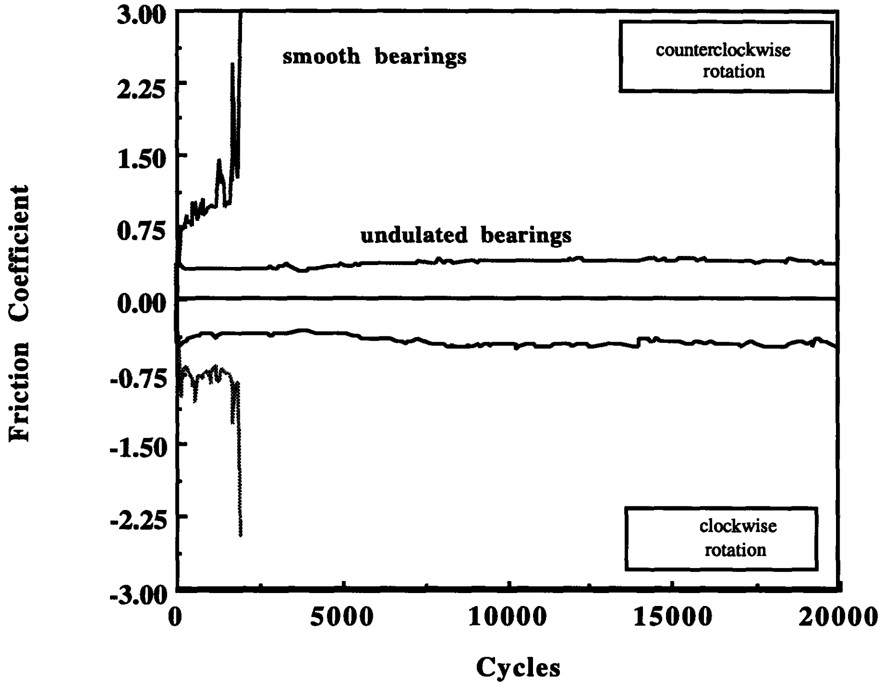

Figure 4.12 Friction coefficient of smooth and undulated bearings in vacuum of 6.5×10^{-6} Pa at room temperature. Normal Load= 12.5 N, Cd= 100 μm.

By comparison the undulated bearing with the same diametral clearance operates consistently throughout the duration of the test. For a diametral clearance of 12.5 m, the friction coefficient of smooth and undulated bearings is shown in Figure 4.12. The smooth bearing seized after about 2500 cycles whereas the undulated one did not show any marked increase during the test.

4.6.3 Results Obtained in Vacuum at Elevated Temperatures

Friction tests in high vacuum and high temperature conditions were performed at a vacuum of 1.3×10^{-4} Pa (10^{-6} Torr) and at temperatures of 150 °C and 245 °C. The level of vacuum was less than that at room temperature experiments due to degassing of the materials at higher temperature. The friction coefficient of smooth bearings with a diametral clearance of 100 μm is shown in Figure 4.13. At 150 °C the friction shows an increase of about 35% compared to those obtained in air or vacuum at room temperature. This increase is about 100% when the temperature was increased to 245 °C.

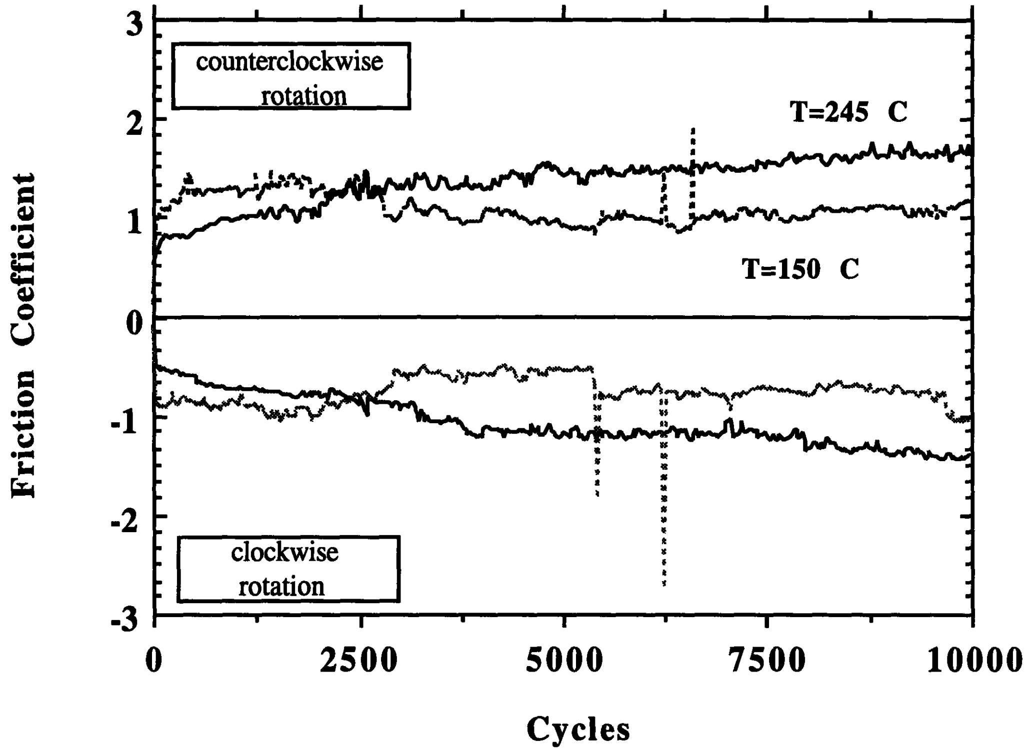

Figure 4.13 Friction coefficient of smooth bearings in vacuum of 1.3×10^{-4} Pa at different temperatures. Normal Load= 2.5 N, Cd= 100 μm.

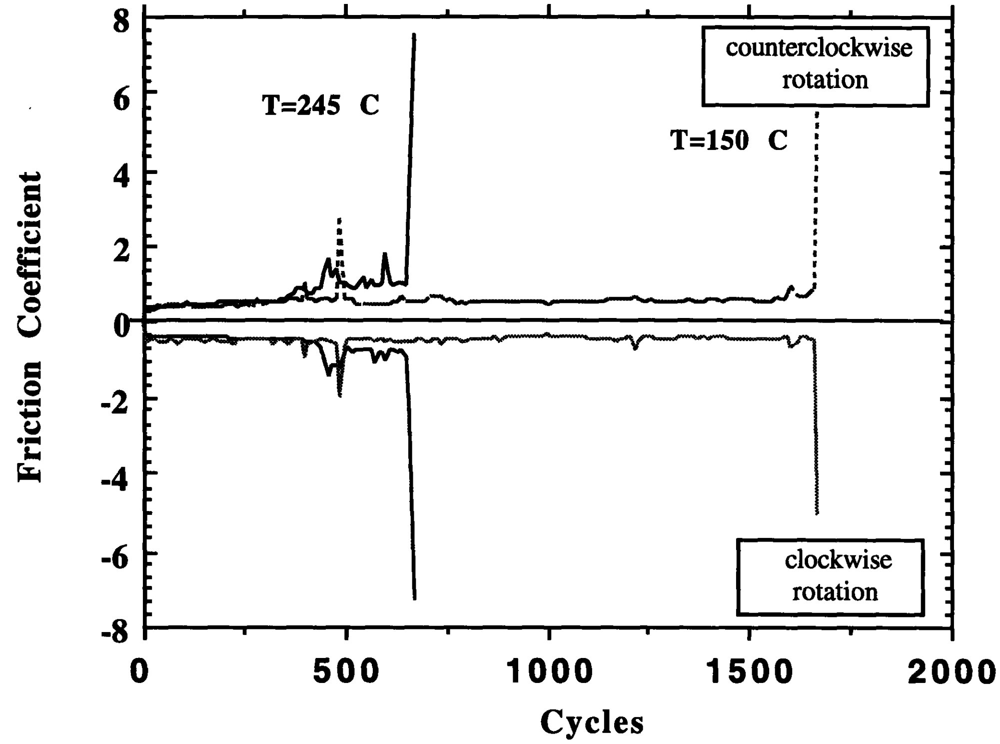

Figure 4.14 Friction coefficient of smooth bearings in vacuum of 1.3×10^{-4} Pa at different temperatures. Normal Load= 2.5 N, Cd= 25 μm.

When the diametral clearance was decreased to 25 μm the smooth bearings seized as shown in Figure 4.14. The failure life of bearings tested at 150 °*C* and 245 °*C* was 650 and 1600 respectively. Undulated bearings were tested at different temperatures in vacuum. Figure 4.15 shows the friction coefficient vs. the number of cycles at two different temperatures. The friction coefficient plot at 150 °*C* has a higher value in the counterclockwise rotation. This was found to be the effect of imbalance in the strain gages bridge. The friction coefficients at both temperatures are higher than that those obtained with undulated bearings at room temperature.

4.7 Examination of Worn Surfaces with SEM

The worn surfaces of copper shafts were examined with the scanning electron microscope. The worn surfaces of smooth bearings show a mild damage to the copper surface in both vacuum and air at room temperature as shown in Figures 4.16 and 4.17. At higher temperatures in vacuum, wear is significant and the damage to the surface can be seen from Figures 4.18 and 4.19 for two different temperatures.

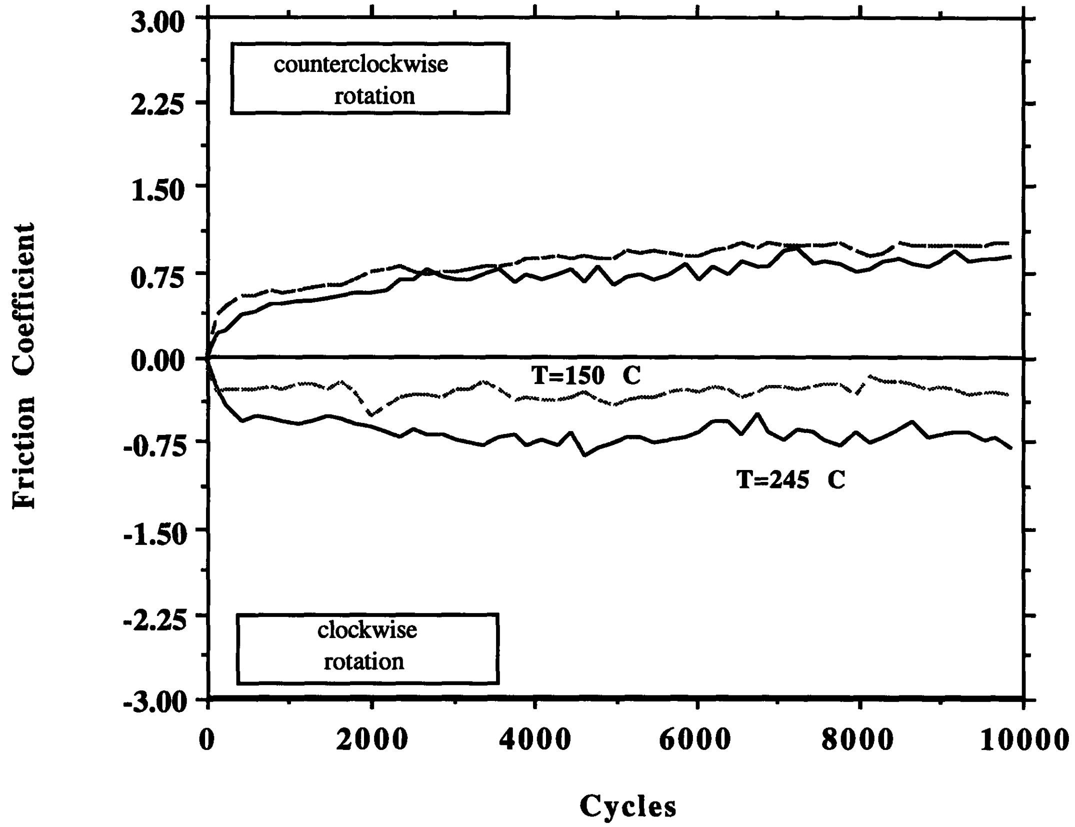

Figure 4.15 Friction coefficient of undulated bearings in vacuum of 1.3×10^{-4} Pa at different temperatures. Normal Load= 2.5 N, Cd= 25 μm.

The micrographs of wear particles trapped in the grooves of an undulated shaft and the micro plowing of undulation pads tested in vacuum at room temperature are shown in Figures 4.20 and 4.21, respectively. The undulated surface have experienced microplowing by hard asperities and small wear particles. However, the amount of damage to the undulations at high temperature in vacuum is significant as shown in Figures 4.22 and 4.23. The damage to the undulations includes plowing and large scale plastic deformation. Such plastic deformation might have been eased by thermal softening of the material. Furthermore, undulations in high temperature/high vacuum have not

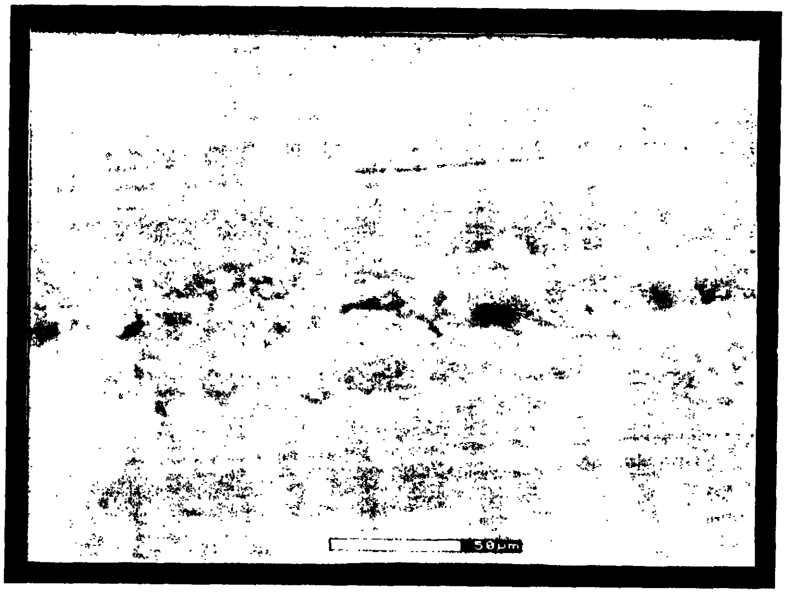

Figure 4.16 Wear tracks on a smooth copper shaft tested in air at room temperature. Normal Load= 2.5 N

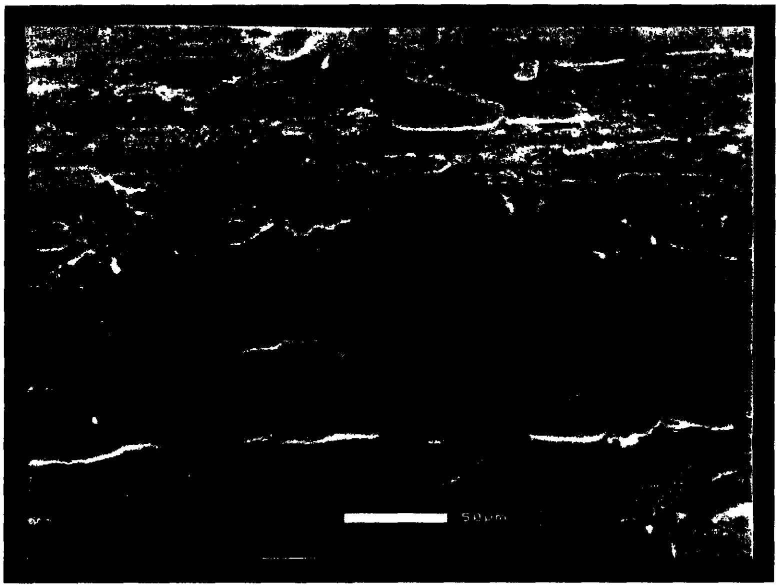

Figure 4.17 Wear tracks on a smooth copper shaft tested in vacuum of 6.5×10^{-6} Pa at room temperature. Normal Load= 2.5 N

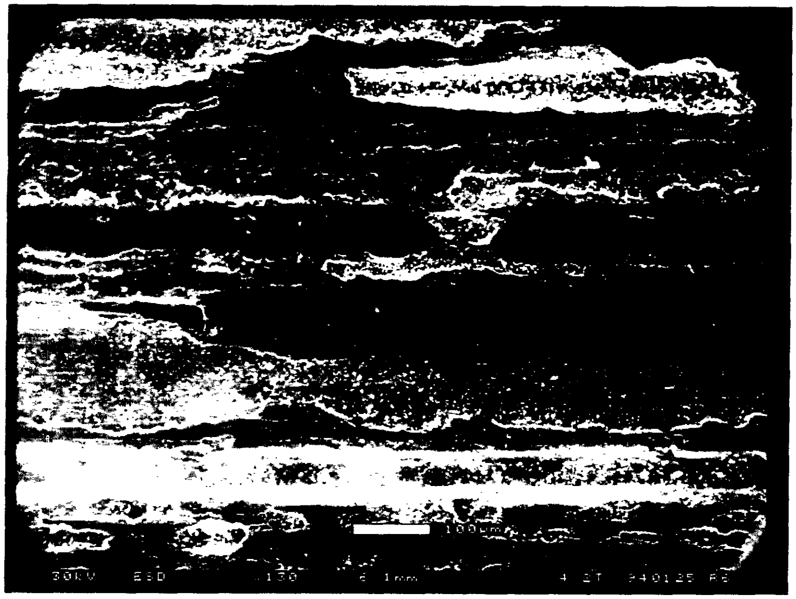

Figure 4.18 Plowing grooves on a smooth copper shaft tested in vacuum of 1.3×10^{-4} Pa at 150 $^{\circ}C$. Normal Load= 2.5 N

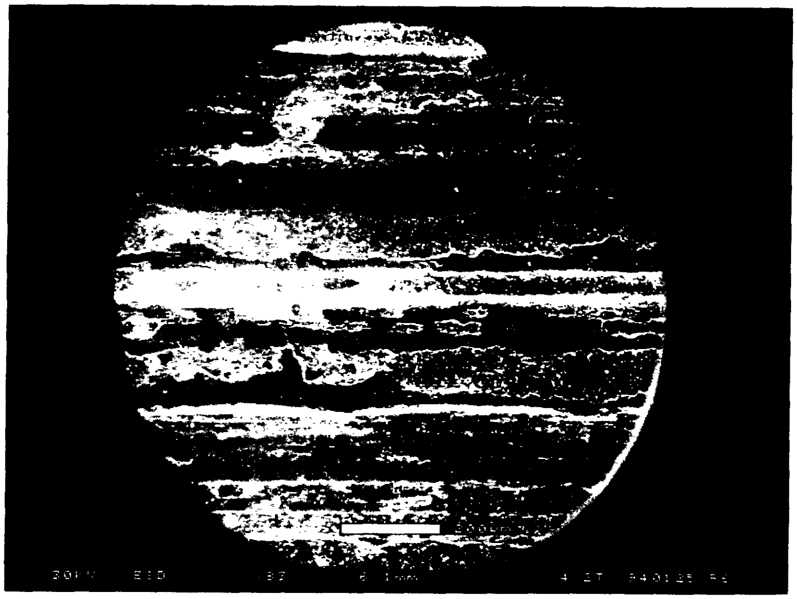

Figure 4.19 Sever plowing of a smooth copper shaft tested in vacuum of 1.3×10^{-4} Pa at 245 $^{\circ}C$. Normal Load= 2.5 N

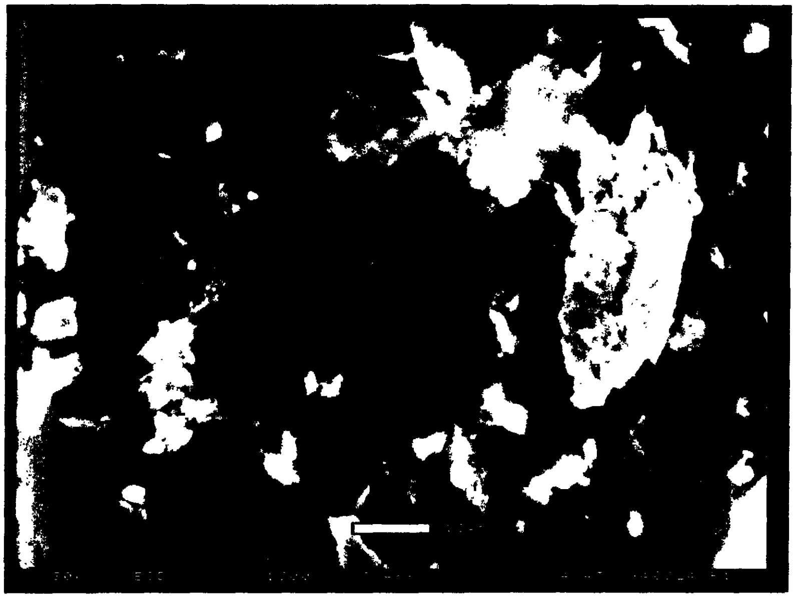

Figure 4.20 Wear particles trapped in the grooves of an undulated copper shaft tested in vacuum of 6.5×10^{-6} Pa at room temperature. Normal Load= 2.5 N

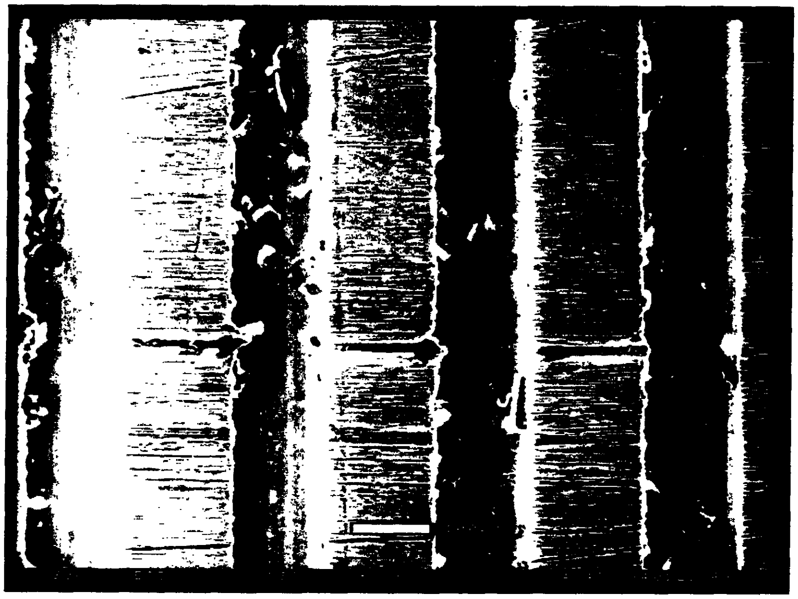

Figure 4.21 Micro-plowing of undulation pads of a copper shaft tested in vacuum of 6.5×10^{-6} at room temperature. Normal Load= 2.5 N

Figure 4.22 Severe plowing of undulation pads of an undulated copper shaft tested in vacuum of 1.3×10^{-4} Pa at 150 $^{\circ}C$. Normal Load= 2.5 N

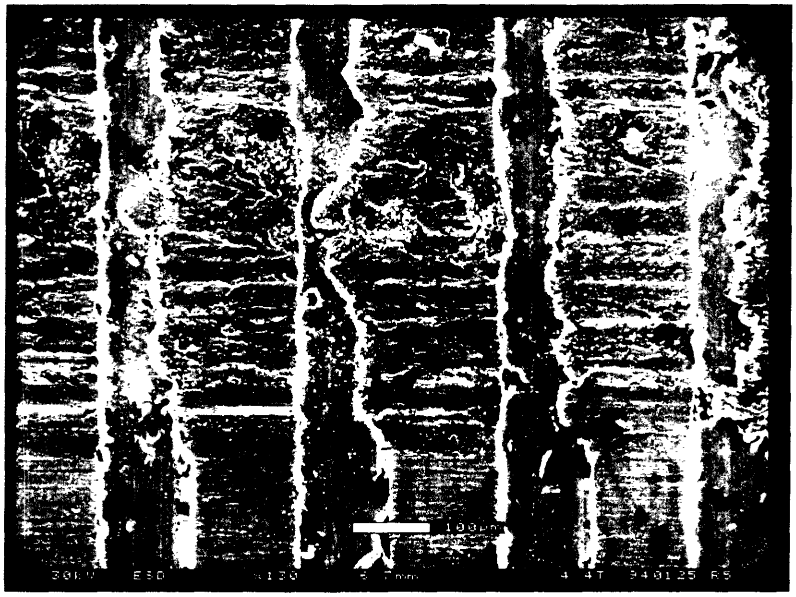

Figure 4.23 Plastic deformation of undulations of an undulated copper shaft tested in vacuum of 1.3×10^{-4} Pa at 245 $^{\circ}C$. Normal Load= 2.5 N

been as effective as those tested in air in Chapter 3 (shown in Figure 3.22) with respect to trapping wear particles at the interface.

4.8 Major Observations of Friction Tests in Different Environmental Conditions

The experimental results obtained in air and vacuum at room temperature and in vacuum at high temperature provide important information which are outlined as follows. These results will be later explained in terms of the role of environmental conditions on the behavior of wear particles while considering the geometrical constraints of the sliding systems.

(1) The friction coefficient of large diametral clearance smooth bearings have not been affected by the atmospheric pressure to levels of 6.5×10^{-6} Pa. The friction coefficient was about 0.7-0.8 for such bearings in air and in vacuum.

(2) For small diametral clearances the friction coefficient of smooth bearings was significantly increased in vacuum compared to that obtained in air. Also, the life-to-failure of these bearings was shorter in vacuum.

(3) Undulated bearings in vacuum and in air for both small and large diametral clearances exhibited almost the same friction coefficient in the range of 0.25-0.4.

(4) At high temperature in vacuum severe wear and a high friction coefficient leading to seizure of smooth bearings were observed. The friction coefficients obtained with large diametral clearances (Table 4.1) can be considered as that of unconstrained systems under the same environmental conditions.

Table 4.1 Summary of friction coefficient of smooth bearings with large diametral clearance (Cd= 100 μm) in different environments.

Environments	Friction Coefficient
Atmosphere Temperature= 25 C	0.8
Vacuum (6.5×10^{-6} Pa) Temperature= 25 C	0.75
Vacuum (1.3×10^{-5} Pa) Temperature= 150 C	1.1
Vacuum (1.3×10^{-5} Pa) Temperature= 245 C	1.65

(5) Undulated bearings have significantly improved the operating life of sliding bearings in high vacuum and high temperature. However, the friction coefficient of undulated bearings in such environments has increased to high values of 0.75. The scanning electron microscopy examination of undulated worn surface shows significant plowing damage to the surface of undulations. Furthermore, the entrapment of wear particles in the grooves of undulations has not been as effective as those bearings examined in Chapter 3. Especially at 245 $^\circ C$ local plastic deformation of undulations has occurred which can clog up the grooves and prevent removal of wear particles from the interface.

A summary of the friction coefficients of undulated bearings in different environmental conditions are given in Table 4.2. It should be noticed that the diametral clearance of theses bearings is four times smaller than those of smooth ones. The smooth bearings with diametral clearance of 25 μm seized in all cases except the one tested in air.

Table 4.2 Summary of friction coefficients of undulated bearings with small diametral clearance (Cd= 25 μm) in different environments.

Environments	Friction Coefficient
Atmosphere Temperature= 25 $^\circ C$	0.25
Vacuum (6.5×10^{-6} Pa) Temperature= 25 $^\circ C$	0.3
Vacuum (1.3×10^{-5} Pa) Temperature= 150 $^\circ C$	0.6
Vacuum (1.3×10^{-5} Pa) Temperature= 245 $^\circ C$	0.75

(6) The failure life of smooth bearings tested in vacuum is strongly dependent on the operating temperature. This has been shown in Figure 4.24 for bearings with 25 μm diametral clearance. For instance, the failure life of smooth bearings at 250 $^\circ C$ is reduced by a factor of 50 compared with the bearings operating in room temperature. Undulated bearings on the other hand did not fail for this period of testing. The final number of cycles in the friction tests with undulated surfaces is considered as the failure life and is shown in the same plot against temperature. A significant improvement is made with undulated surfaces with respect to the operating life of the sliding bearings. The failure life seems to be independent of the operating temperature.

4.9 Similarity Between Friction Coefficient of Large Diametral Clearance Systems with That of Unconstrained Systems

A bearing with a large diametral clearance can be considered an unconstrained system. Therefore, an attempt was made to compare the frictional behavior of large diametral clearance bearings with the unconstrained system. A series of pin-on-disk type experiments were conducted with stainless steel pins on OFHC disks in a wide range of normal load in vacuum of 6.5×10^{-6} Pa and in air. The sliding speed and the wear track diameter for all tests was 10 cm/s and 2.5 cm respectively. This translates to a 0.75 second travel time for the pin to complete one turn. The copper disks were polished to a mean roughness of about 30 nm while that of the stainless steel pins was about 25 nm. The friction

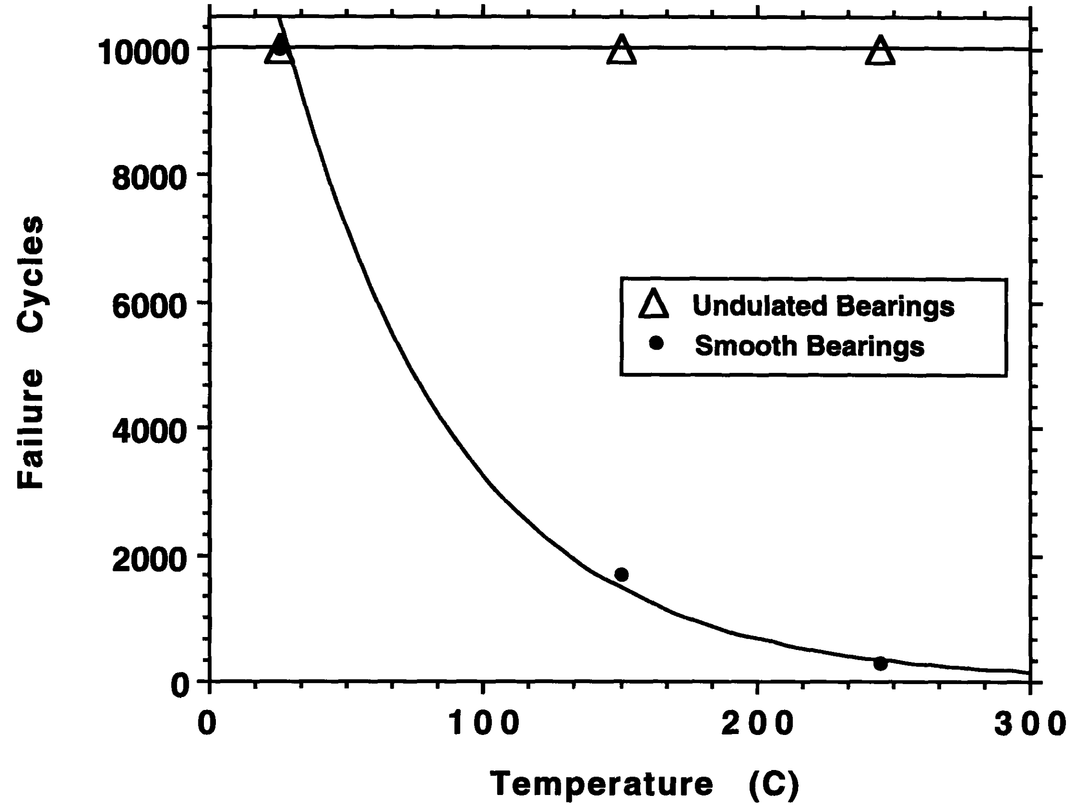

Figure 4.24 Failure cycles of smooth and undulated bearings vs. temperature in vacuum of 1.3×10^{-5} Pa. Normal Load= 2.5 N, Cd= 25 μm

coefficients are shown in Figure 4.25. Under a heavy normal load, i.e. 200 g or 50 g, the friction coefficient is about 0.4 for both vacuum and air. When the normal load is light, i.e. 2 g and 1 g, the friction coefficient is about 0.25 and again is the same for vacuum and air. The conclusions that can be drawn from these experiment are as follows.

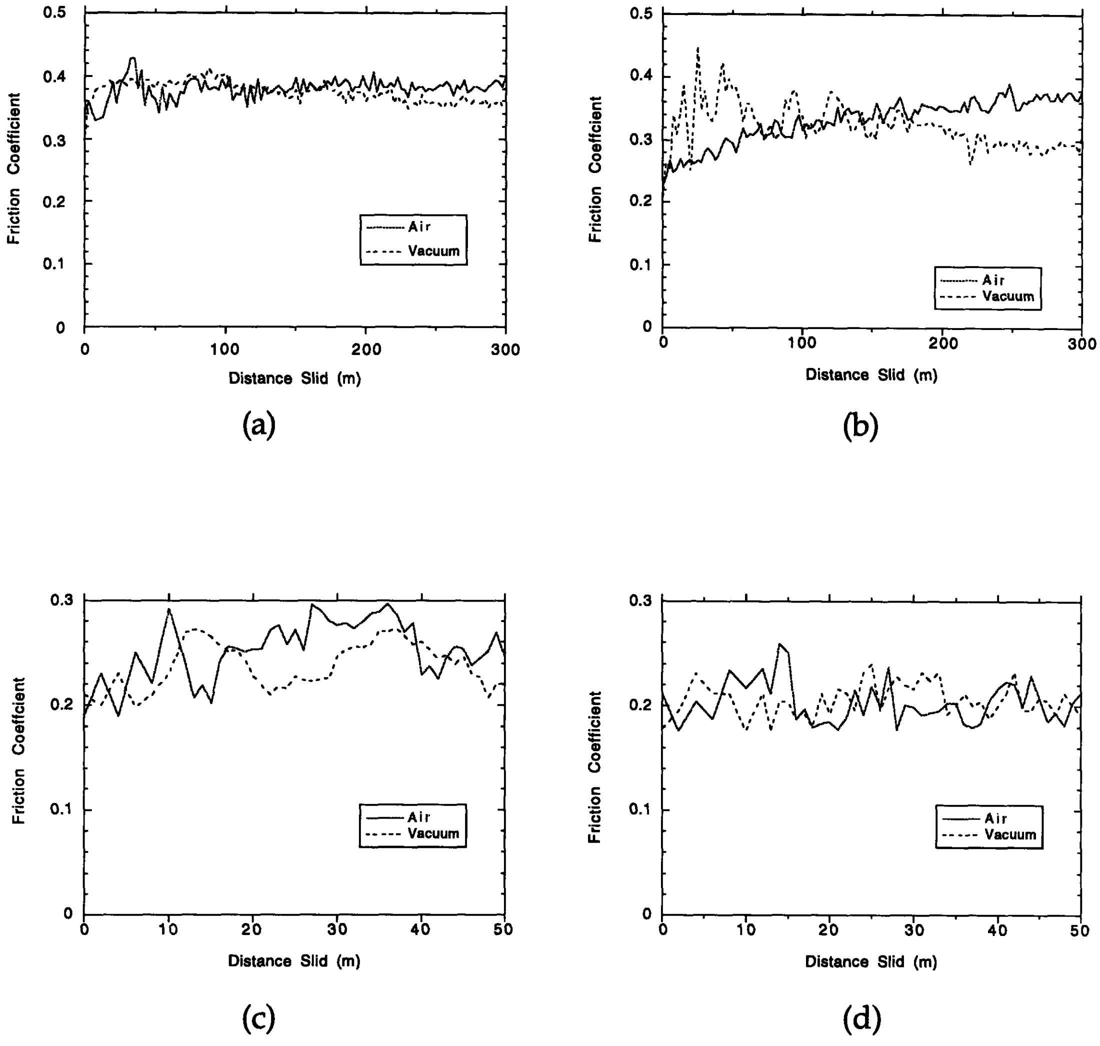

(a) (b) (c) (d)

Figure 4.25 Friction coefficient of stainless steel balls (4 mm diameter) against OFHC disks under 200 g (a), 50 g(b), 2 g (c), and 1 g (d) normal load. Speed= 5 cm/s.

First, contrary to what has been reported in the literature that vacuum will increase the friction coefficient due to higher adhesion with clean surfaces [32-34], such an increase is not observed in this study even in vacuum of 6.5×10^{-6} Pa. Instead, the friction coefficient in vacuum and air for a wide range of normal loads seems to be the same. Second, the transition from a low friction regime to a high regime is not caused by higher adhesion due to the removal of oxide layers. If this were the case then the friction coefficients after transition for vacuum and air would be different due to the absence of surface contamination in vacuum. The transition, instead is caused by the increasing number of wear particles at the interface and the subsequent plowing action [28]. The role of higher normal load is to accelerate the transition due to the larger plastic deformation of the surface layer which in turn accelerates the formation of wear particles.

The low friction coefficients obtained with undulated bearings in vacuum and air without any transition from a low friction regime to a high one supports the above statement as well. Since the only difference between the undulated and smooth surfaces is in removal of wear particles by undulations, one can appreciate the role of wear particles on friction especially when the clearance of the sliding system is small.

The conclusion is that for extremely small clearance systems the increase in the friction coefficient in vacuum is not solely due to the removal of surface films and higher adhesion. Instead, such environment and the geometrical constraints accentuate the mechanical components of friction. The mechanism by which these two influence the friction coefficient is wear particle agglomeration.

References

[1] Snyder, Jr., C.E., Gschwender, L.J., Randolph, B.B., Paciorek, K.J.L, Shih, J.G. and Chen, G.J., "Research and development of low volatility long life Silahydrocarbon based liquid lubricants for space", Lubrication Engineering, Vol. 48, No. 4, 1992, pp. 325-328.

[2] Ward, W.E., "Evaluation of a 90-mm Bore bearing operating in a simulated space environment", Lubrication Engineering, Vol. 40, No. 1, 1984, pp. 290-928.

[3] Sharma, K.S., Snyder, Jr., C.E., Gschwender, L.J., "Tribological behavior of some candidate advanced space lubricants", STLE Transactions, Vol. 36, No. 2, 1993, pp. 321-325.

[4] Mortimer, B., and Lancaster, J.K., "Extending the life of aerospace dry bearings by the use of hard smooth counterfaces", Wear, Vol. 121, 1988, pp. 289-305.

[5] Singer, I.L., "Solid lubrication films for extreme environments", Materials Research Society Proceedings, Vol. 140, 1989, pp. 215-225.

[6] Holinski, S., and Gansheimer, J., "A study of the lubricating mechanism of molybdenum disulfide as a lubricant", Wear, Vol. 19, 1972, pp. 329-342.

[7] Spalvins, T., "Morphological and frictional behavior of sputtered MoS_2 films", Thin Solid Films, Vol. 96, 1982, 17-24.

[8]DeGee, W.J., Solomon, Y., and Zaat, J.H., "On the mechanisms of of MoS_2 films failure in sliding friction', ASLE Transactions, Vol. 8, 1983, pp. 209-218.

[9] Suzuki, M., Moriyama, M., and Hasegawa, M., "Friction and wear of self-lubricating composites at temperatures to 450 C in vacuum", Wear, Vol. 162-164, 1993, pp. 471-479.

[10] Young, D.M., and Crowell, A.D., "Physical adsorption of gases" Butterworth & Co., London, 1962.

[11] Dash, J.G., 'Films on solid surfaces" ,Academic Press, Inc., New York, NY, 1975.

[12] Li, Z., Rabinowicz, E., and Saka, N., "The stiction between magnetic recording heads and thin film disks", STLE transactions, Vol. 26, 1989, pp. 64-70.

[13] Bhushan, B., and Dugger, M.T., "Liquid-meditated adhesion at the thin-film magnetic disk/slider interface", ASME Journal of Tribology, Vol. 112, 1990, pp. 217-223.

[14]McClelland, G.M., and Mate, C., "Atomic scale friction measured with an atomic force microscope", Engineering Materials for Advanced Friction and

Wear Applications", P.J. Blau and Smidt, eds., ASM Intl., Metals Park, OH, 1988, pp. 13-22.

[15] Schneir, J., Marti, O., Remmers, D., Glaser, D., Ronnenfeld, R., Drake, B., and Hansma, P.K., "Scanning tunneling microscopy and atomic force microscopy of the liquid-solid interface", Journal of Vacuum Science and Technology, Vol. 6A, No. 2, 1988, pp. 283-286.

[16] Johnson, J.L., " Slding monolithic brush systems for large currents", Electrical Contacts, III. Inst. Tech., Chicago, IL, pp. 3-17.

[17] Gao, C., Kuhlmann-Wisldorf, D., Makel, D.D., "Moisture effects including stiction resulting from adsorbed water films", Journal of Tribology, Vol. 114, No. 1, 1992, pp. 174-180.

[18]Gao, C., Kuhlmann-Wisldorf, D., Bednar, M.S., "On the tribological behavior of adsorbed layers, especially moisture", Wear, Vol. 149, 1991, pp. 297-312.

[19] Kayaba, T., and Kato, K., "Frictional properties of surface films in air and in high vacuum" Wear, Vol. 47, 1978, pp. 93-105.

[20] Kofstad, P., High Temperature Corrosion, Elsevier Applied Science Publishers LTD, London, U.K. , 1988.

[21] Cocks, M., "Surface oxide films in intermetalic contact", Nature, Vol. 170, 1952, pp. 203-204.

[22]Rabinowicz, E., "Lubrication of metal surfaces by oxide films", ASLE transactions, Vol. 10, 1967, pp. 400-407.

[23]Wilson, J.E., Stott, F.H., and Wood, G.C., "The development of wear protective oxides and their influence on sliding friction", Proceedings of the Royal Society, Series A, Vol. 369, 1980, pp. 557-574.

[24] Quinn, T.F.J., Sullivan, J.L., and Rowson, D.M., "New developments in the oxidation theory of the mild wear of metals", Proceedings of International Conference on Wear of Materials, Dearborn, Mich., April 16-18, 1979, Eds. Ludema, K.C., Glaser, W.A., and Rhee, S.K., ASME, New York, 1979, pp. 1-11.

[25] Tao, F.F., "A study of oxidation phenomenon in corrosive wear", ASLE Transactions, Vol. 12, 1969, pp. 97-105.

[26] Komvopoulos, K., Saka, N., and Suh, N.P., "The significance of oxide layers in boundary lubrication", Journal of Tribology, Vol. 108, 1986, pp. 502-513.

[27] Lancaster, J.K., "The formation of surface films and the transition between mild and severe metallic wear, Proc. Royal Soc. A, Vol. 273., 1963, pp. 466-483.

[28] Suh, N.P., Tribophysics, Prentice-Hall, Inc., Englewood Cliffs, New Jersy, 1986, pp. 65-75.

[29] Tylecote, R.F., Howd, D., and Furmidge, J.E., "The influence of surface films on the pressure welding of materials", British Welding Journal, Vol. 5, 1958, pp. 21-38.

[30] Bocharov, Y., Kobayashi, S., and Thomsen, E.G., "The mechanics of the coining process", Journal of Engineering for Industry, Vol. 84, 1962, pp. 491-501

[31] Oktay, S.T., and Suh, N.P., "Wear particle formation and agglomeration", Journal of Tribology, Vol. 114, No. 2, 1992, pp. 379-393.

[32] Batchelor, A.W., Stachowiak, G.W., Cameron, A., "The relationship between oxide films and the wear rate of steels", Wear, Vol. 113, 1986, pp. 203-223.

[33]Zhang, R., Zhu, B., and Liu, J., "Mutual transfer of materials for dry sliding of brass against stainless steel", Wear, Vol. 140, 1990, pp. 207-222.

[34]Lebedeva, I.L., and Presnyakova, G.N., "Adhesion wear mechanism under dry friction of titanium alloys in vacuum", Wear, Vol. 148, 1991, pp. 203-210.

Chapter 5

Minimization of Mechanical Aspects of Friction Through the Design of Covalent Solids

5.1 Introduction

The contribution of mechanical factors to friction of geometrically constrained sliding systems was investigated in the previous chapters. Although undulated surfaces served to reduce such factors by the removal of wear particles from the interface, plowing on microscale in air and even to a larger extent in high vacuum/high temperature environments was not entirely avoided. Friction coefficients as low as 0.25 obtained by undulated surfaces over a long operating time might be considered satisfactory for certain sliding systems where some damage to the sliding surfaces is tolerable. However, such a friction coefficient is not low enough for applications in which the energy losses due to friction must be extremely small. Miniature mechanical and electromechanical mechanisms, magnetic recording devices, bioengineering bearings, are some of the tribological systems in which low friction and low wear are the most important design requirements. The small relative motion of sliding surfaces in miniature systems of high stiffness requires a new design of surfaces which exhibit ultra-low friction in short sliding distances without wear [1-3]. In magnetic recording devices, for example, a low friction coefficient at start up would increase the durability of the storage media [4,5]. In biomedical applications wear debris can cause a foreign body tissue response, leading to potential failure of the sliding components [6,7].

Besides these special applications, the development of ultra-low friction surfaces could have a great impact on the design of bearings. Many complex bearings and their auxiliary equipment could be replaced by simpler low friction sliding bearings. The stiffness of precision machines could be increased leading to nanoscale tolerances. All these benefits result in energy and cost savings as well as improvements in the life of engineering machines, a considerable contribution indeed.

5.2 An Ideal Surface for Sliding

Although it is clear from the theoretical point of view that the lowest friction coefficient can be achieved through only the elastic interactions of sliding surfaces, the practical implementation of such an idea in actual sliding situations using the existing solids is rather difficult, if not impossible. In an attempt to maintain a low contact pressure at the sliding interface to minimize the chance of plastic deformation at the asperity contact, Kim [8] studied the friction of smooth and hard solids under relatively light loads. At first it was thought that an elastic contact with a friction coefficient of 0.09 had been achieved, for examination of the surfaces using SEM did not show any damage to the surface. However, etching of the tested surface revealed that dislocations were lined up along the sliding path, suggesting that indeed plastic deformation had taken place. The conclusion was that the occurrence of plastic deformation of the surface layer during the contact sliding of solids is in fact unavoidable.

5.2.1 Functional Requirements

It is well known that if a solid in a sliding contact situation is too soft it will undergo plastic deformation at the surface, whereas if it is too hard the contact stresses will be high enough to cause plastic deformation in the subsurface. Thus the goal of this study was to develop a model surface to prevent plastic deformation at the surface as well as in the subsurface. The first step toward this goal is the identification of the functional requirements for such a surface. The following requirements should be met if the minimum friction coefficient is to be achieved.

- The sliding surfaces should be atomically smooth to reduce the high asperity contact stresses which results in the microscale permanent deformation of the interface.
- The surface layer should be very compliant to allow a large reversible elastic deformation in order to accommodate the microscale asperities of

the counterface and to distribute the surface traction on a large region of the substrate.

- The substrate should be hard enough to carry the normal and tangential surface traction due to the frictional loading without undergoing plastic deformation.
- The surface atoms or molecules must only form secondary van der Waal's bonds with the counterface in order to reduce the breakage energy of the atomic interactions at the interface while they are bound together through primary bonds.

To satisfy these functional requirements a material with a diamond-like bulk and an elastomeric-like surface is needed [9]. The elastomeric surface can accommodate the microscale asperities of the counterface without undergoing plastic deformation. In addition, the covalent bonds of the surface layer, which are formed only between specific atoms and are directional, do not allow the formation of primary bonds with the counterface. However, the elastomeric surface layer must have a limited degree of crosslinking to allow some movement of the molecular chains in an elastic manner.

5.2.2 Solid Lubrication Versus Elastic Contact

The idea of developing a covalent solid using an elastomeric surface layer on a hard substrate to reduce the friction might seem similar to the use of a solid lubricant at the sliding interface to reduce the shear resistance of the interface to motion. In particular the friction mechanisms that governs the friction of polymer films such as polytetrafluoroethylene (PTFE) and polyvinylidenefluoride (PVF), which are now being used as solid lubricants can be mistaken with the solid whose functional requirements were specified previously.

The concept of using a soft material layer is based on the adhesion theory of friction which expresses the friction coefficient as the ratio of the junction flow strength (τ) to the hardness (H):

$$\mu = \frac{\tau}{H} \tag{5.1}$$

A soft solid film, according to this theory, provides a low junction flow strength while the hardness of the material is kept high due to the hard substrate; thus reducing friction. A special case is when the soft layer has a lamellar structure. The interplanar bonds can be broken due to the shear force at the surface and result in low friction.

Obviously the basis of solid lubrication concept is the occurrence of plastic deformation either at the junctions or between the molecular layers [10-12]. This is in opposition to the goal which is set in this study. The surface molecules in the ideal surface are expected to respond elastically to the moving asperities, and no interplanar slip is allowed. The means to providing such properties are the crosslinking of molecular chains of the elastomer and the boundary conditions during the sliding. This issue will be addressed later in the conclusions in the light of experimental results to evaluate the frictional behavior of the model surface.

The method used in this study to develop such a surface was to use elastomeric thin polyurethane coatings on a hard and smooth substrate. The hypothesis being that through the minimization of the mechanical interactions at the interface and the plastic deformation of the substrate, low friction coefficients could be achieved. The friction coefficient obtained in the absence of such effects will be mainly due to adhesion at the interface and the hysteresis losses in the film.

Polyurethane coated surfaces were created and tested in an earlier study [13]; however, the lowest friction coefficient achieved was 0.16. The major source of energy loss for such surfaces seemed to be hysteresis losses and therefore in this study the frictional behavior of sub-micron films is investigated.

5.3 Materials and Coating Procedure

A hard substrate in the form of a smooth silicon wafer was coated with a thin layer of polyurethane to create an elastomeric surface layer. Bayhydrol 121 and Bayhydrol 123, two polycarbonate-based aqueous polyurethane dispersions comprising polyurethane, N-methyl pyrrolidinone, and triethylamine were supplied by Miles Industries Inc. These two polyurethane dispersions can be used in the formulation of ambient-cure or baked coatings for a wide range of rigid and flexible substrate such as plastics and metals. They exhibit a combination of flexibility, good water and solvent resistance, and hydrolytic stability. In addition, they may be blended together to achieve intermediate properties. The physical properties of polyurethane dispersions are given in Table 5.1.

Table 5.1 Physical properties of polyurethane dispersions

PU Dispersion	**Bayhydrol 121**	**Bayhydrol 123**
physical form	liquid	liquid
color	milky white	milky white to brown
pH	7.0-8.5	7.5-9.0
Boiling point (°C)	100	100
Specific gravity	1.1	1.07

Polyurethane films were prepared by dipping single crystal silicon wafers ({100} orientation) into solution. containing 5%, 7.5%, 10%, and 12.5% polyurethane dispersions. Different PU concentrations lead to various film thicknesses. These solutions were made by diluting PU dispersions with deionized water and by mechanical stirring. Also each solution contained 0.5%, by volume, of a nonionic surfactant, (a fluorad coating additive commercially known as FC-430 supplied by 3M Co.), to improve wetting of the silicon surface by the solution. This coating additive is soluble and compatible with most polymers and remains active throughout the drying and curing process. When used in water-based polymers FC-430 tends to reduce the aqueous/organic interfacial tension and remains surface active in the organic portion of the polymer system. The use of a good surfactant can eliminate surface defects in coatings, such as cratering and crawling, caused by poor wetting of a low energy surface or of a contaminated substrate. Also, leveling problems caused by surface tension gradients formed during drying of the film can be eliminated. Finally, a proper surfactant can maintain surface tension balance between solvent and polymer, and thereby preventing creeping during solvent evaporation. The physical properties of the surfactant are given in Table 5.2.

Silicon wafers that had been rinsed with deionized water and allowed to air dry were mechanically dipped into polyurethane solutions by attaching one end of a thread to the wafer and the other end of the thread to a speed-controlled motor. The silicon wafer was dipped into the solutions at a speed of 0.2 cm/s and allowed to remain in the solution for 30 s and then was taken out from the solution at the same speed.

Table 5.2 Physical properties of the surfactant FC-430.

Surfactant	**Fluorad Coating additive (FC-430)**
Type	nonionic
Color	amber
Viscosity at 25 C (cp)	7000
Specific gravity	1.1
Refractive index at 25 C	1.446

In this dip-coating method, the thickness of the deposited liquid film depends on the properties of the coating solution (density, viscosity, and surface tension) and on the selected withdrawal speed. In general, the film thickness is a function of the square-root of the withdrawal speed and therefore the higher this speed is, the thicker the film will be [14,15]. Coated wafers were then air dried for about 15 hours at 25 °C while they were kept at an angle of about 20 ° to the horizontal.

In order to crosslink the coatings the coated samples were baked in an oven at different temperatures. The baking time for all samples was 15 minutes. Some unbaked samples were also used in the testing for comparison with the baked samples. Furthermore, some of the coatings baked at 140 °C were electron beam irradiated to further increase the crosslinking density. The electron beam energy of irradiation was 2.5 MeV and the dosage was varied.

The mechanical properties of silicon wafers, borosilicate glass balls, and polyurethane coatings based on the data obtained from the manufacturer are given in Tables 5.3 and 5.4.

Table 5.3 Mechanical properties of polyurethane films

Coating Materials	**Bayhydrol 121**	**Bayhydrol 123**
Tensile strength (MPa)	46.19	41.37
Elongation at Break (%)	150	320
Modulus at 100% Break (MPa)	34.89	6.41
Hardness (pencil)	2H	H

Table 5.4 Mechanical properties of silicon wafers and glass balls

Material	Hardness (MPa)	Modulus (GPa)
Silicon wafers ({100} orientation)	8000	110
Borosilicate glass balls (4 mm diameter)	6000	70

A roughness analysis of the silicon wafers was performed using a DekTak 3000 profilometer. The profile of the silicon substrate and the analysis box are shown in Figure 5.1. The RMS and mean roughness of the wafers were 3.3 and 3.4 nm respectively while the peak to valley roughness was about 16.2 nm.

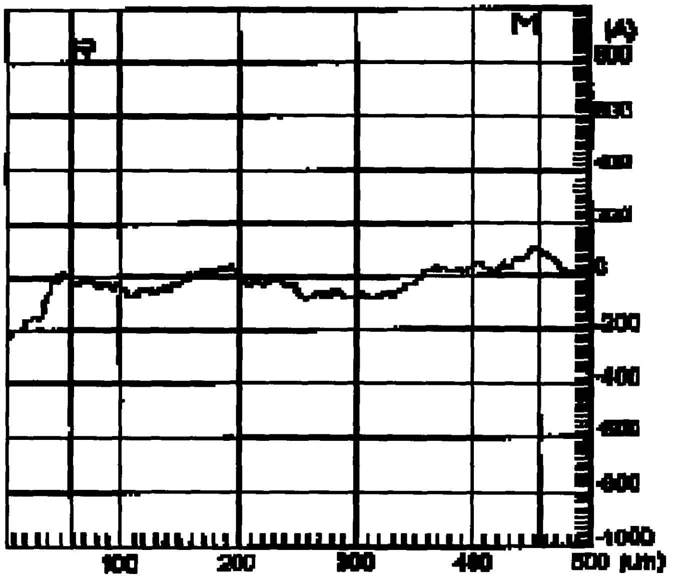

(a)

ANALYTIC FUNCTIONS:			R: (mm)	M: (mm)
Ra	= 33	A	57.45	455.32
Rq	= 39	A	57.45	455.32
Rt	= 162	A	57.45	455.32
P-V	= 151	A	57.45	455.32

(b)

Figure 5.1 Surface profile (a) and roughness analysis (b) of the silicon substrate.

The entire process of making solutions, coating silicon wafers, air drying samples, as well as friction testing, was performed under a Class 100 laminar flow hood to minimize the effect of air-borne particles. The temperature was set to 25 °C during the sample preparation process and testing.

5.4 Coating Characteristics

The thickness of the films was a function of polyurethane concentration in the solutions and the withdrawal speed of silicon wafers from the solutions. Since the withdrawal speed was set to 0.2 cm/s for all coatings the only variable that affects the thickness is the concentration. A profilometer was used to measure the thickness of polyurethane coatings. Using a sharp blade, a small area of the film was removed and the change in the height as the profilometer's tip steps down from the film onto the silicon surface was monitored. The thickness of the layer ranged from 0.09 to 0.25 μm for Bayhydrol 121 and from 0.11 to 0.4 μm for Bayhydrol 123. Figure 5.2 shows the film thickness as a function of polyurethane concentration in the solutions for both materials.

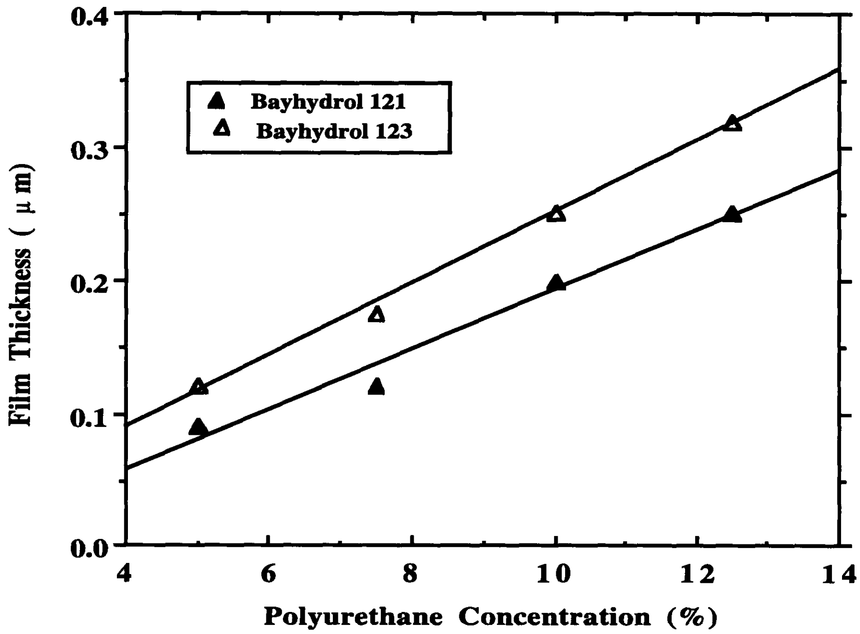

Figure 5.2 Thickness of the films as a function of polyurethane concentration in the solution.

5.5 Experimental Set-up

A reciprocating pin-on-disk tester was used to carry out friction tests on polyurethane coatings of varying thickness and normal loads. The main part of the tester , shown in Figure 5.3, is a tempered steel cantilever of breadth and length of approximately 15 mm and 125 mm respectively. Strain gages are installed near the fixed end of this cantilever and wired in a Whetstone bridge which is connected to a data acquisition system. A small horizontal deflection of the free end of the cantilever causes an unbalanced voltage from the strain gages which is converted to a horizontal force through calibration. The force measurement resolution of this cantilever is 5 mg when the excitation voltage is 5 volts. The cantilever was pivoted on ball bearings and could be balanced by a counterweight when there was no applied load on the pin. The cantilever assembly was fixed on an adjustable height table which allowed fine adjustment of the glass ball on the coated samples prior to loading. The test samples were positioned on a reciprocating table with variable speed and amplitude.

Friction tests were carried out at a speed of 0.3 cm/s under normal loads ranging from 0.5 to 5 g for a ball of radius of 2 mm. When a larger ball with a radius of 76.6 mm was used to carry out friction tests the normal load was 20 g. Prior to each test, the glass balls were washed with isopropyl alcohol and left to dry in the clean room. Both pins and coated samples were dusted off with clean air prior to each test. The distance slid for in cycle was 2 cm and for most of the tests the total number of cycles was 50.

The data acquisition program only measures the frictional force in each test during sliding and not near the end of the stroke in each cycle. This assures that the noise generated as a result of a sudden stop in the motion of the reciprocating table at the end of each cycle is filtered out from the friction results. Furthermore, the friction data were averaged over the sliding distance in each cycle.

5.6 Experimental results

The results can be grouped into three different sections for ease of discussion. In the first part the effect of varying the normal load and the film thickness will be addressed. In the second part the effect of crosslinking of the polymer coating will be presented. Finally in the third section the results of experiments conducted with large surface pins are described.

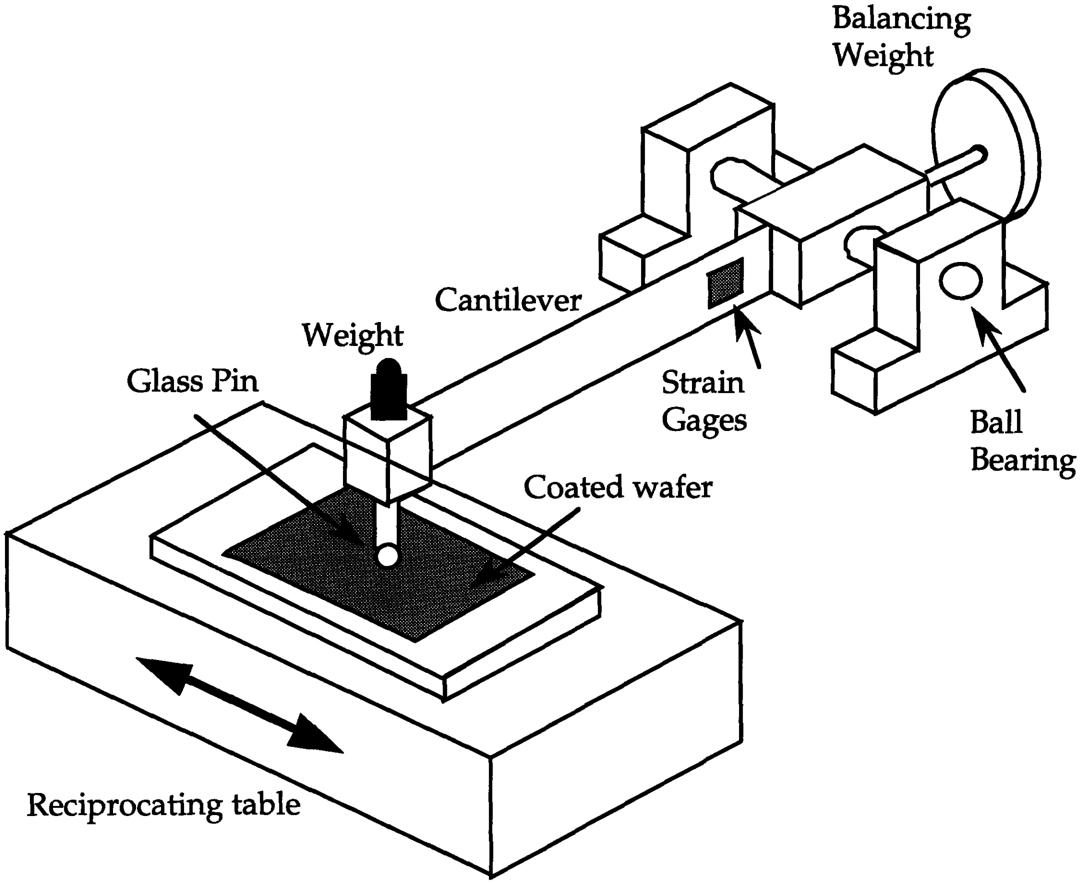

Figure 5.3 Schematic of the low load friction tester with a transverse force resolution of 5 mg.

5.6.1 Effects of Normal Load and Film Thickness on Friction

Average friction coefficients of films made of Bayhydrol 121 sliding against a 4 mm borosilicate glass ball are shown in Figure 5.4 through Figure 5.6. Three significant observations can be made from the data. First, in all tests the friction coefficient starts off from a low value of 0.03-0.08 and in many cases it stays at this low value for the duration of the test. Second, as the thickness of the film decreases the possibility of the film being removed in the early sliding cycles is high. This is the case for the 0.09 μm thick film tested under a 5 g normal load.

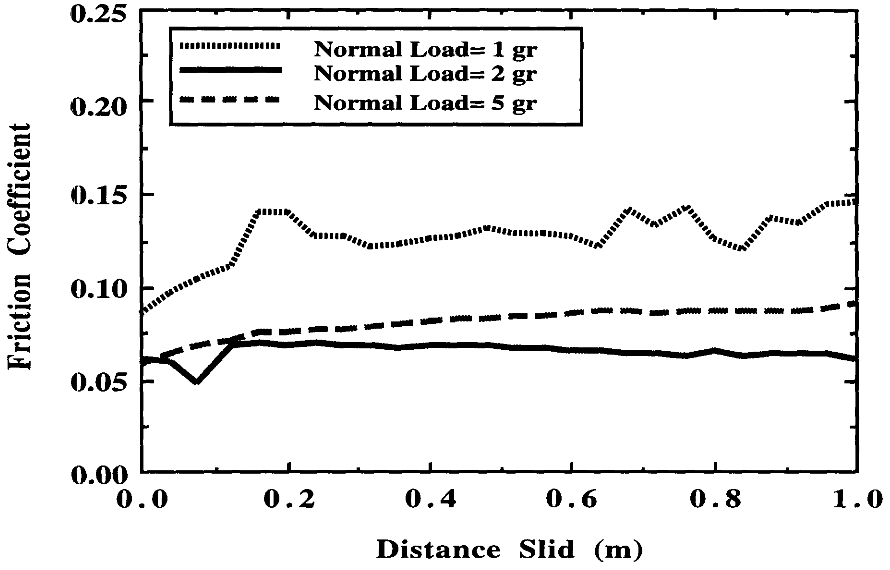

Figure 5.4 Friction coefficient of a 0.25 μm thick film of Bayhydrol 121.

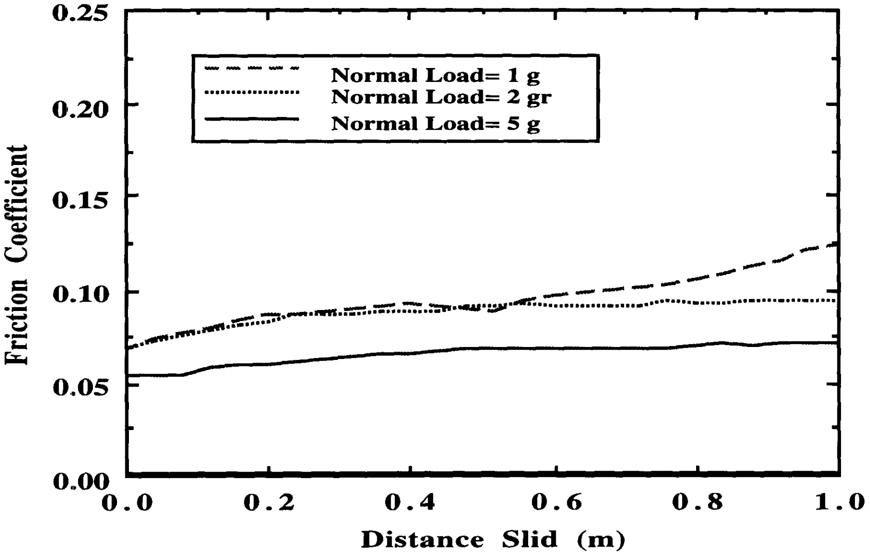

Figure 5.5 Friction coefficient of a 0.2 μm thick film of Bayhydrol 121.

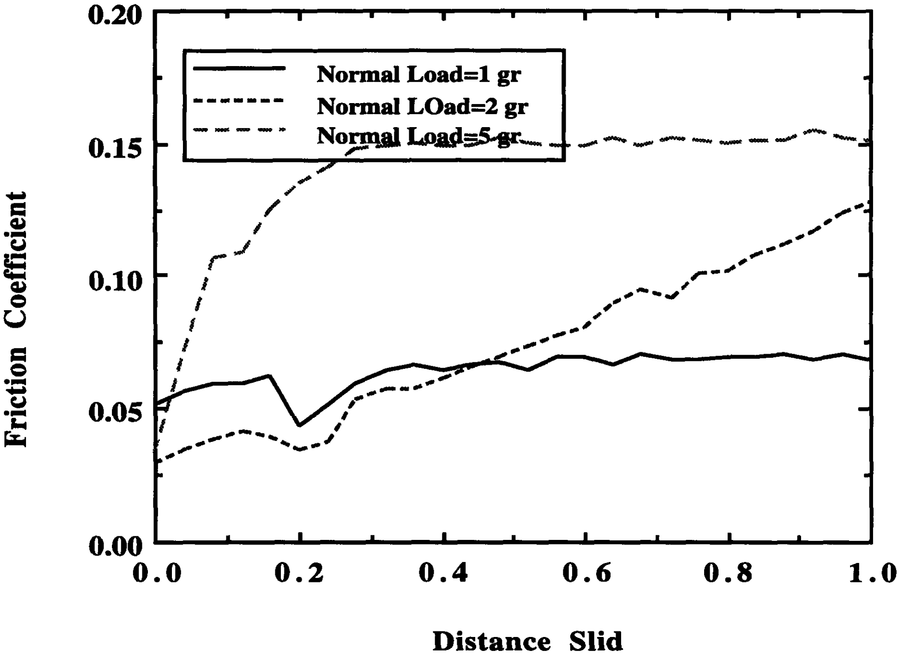

Figure 5.6 Friction coefficient of a 0.09 μm thick film of Bayhydrol 121

The friction coefficient increases sharply to a high value of 0.15 due to extensive plastic deformation of the surface layer. Third, when the normal load was 1 or 2 g light microscopy examination of the tested samples showed no apparent damage to the surface. However, as it will be shown in the AFM studies of the wear tracks, nanoscale damage to the surface during the friction testing had occurred.

Films made of Bayhydrol 123 whose modulus is about one fifth of that of Bayhydrol 121 were also friction tested under the same conditions. The higher compliance of this material is expected to result in a better load distribution in the surface layer and less damage to the surface which in turn results in lower friction coefficient. The friction coefficient plots are shown in Figure 5.7 through Figure 5.9. Generally friction coefficients were slightly lower compared with those of Bayhydrol 121 and the minimum friction coefficient was 0.04 under 2.5 g normal load and with a 0.25 μm thick coating. Wear tracks for 1 and 2 g normal load could not be seen with the naked eye nor by optical microscopy, but it was evident in the atomic force microscope as will be discussed later.

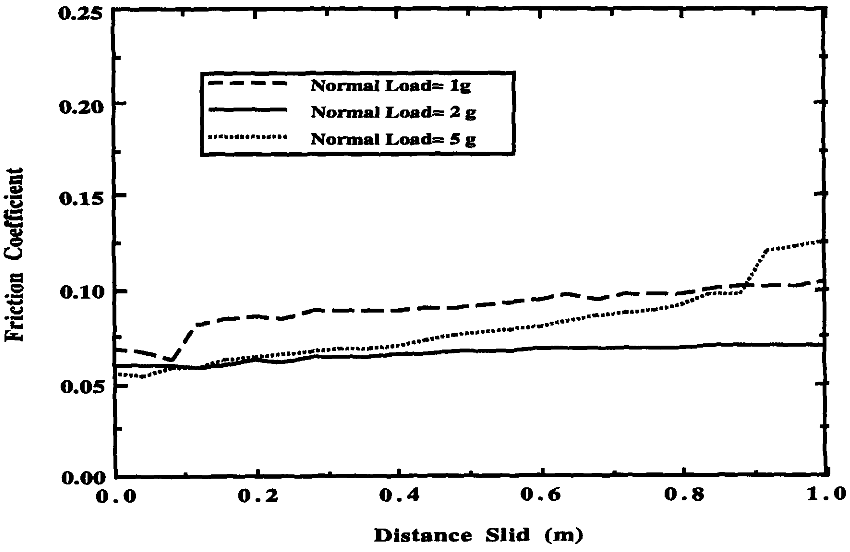

Figure 5.7 Friction coefficient of a 0.4 μm thick film of Bayhydrol 123

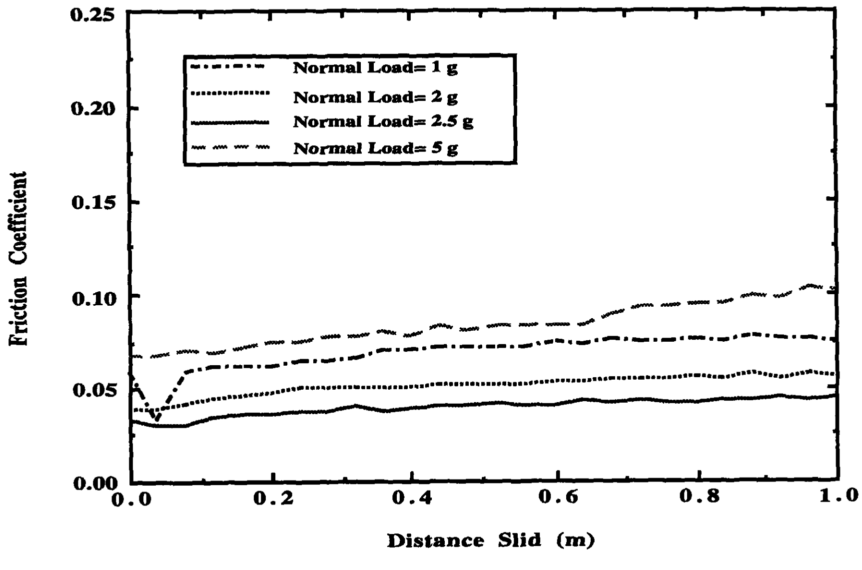

Figure 5.8 Friction coefficient of a 0.25 μm thick film of Bayhydrol 123

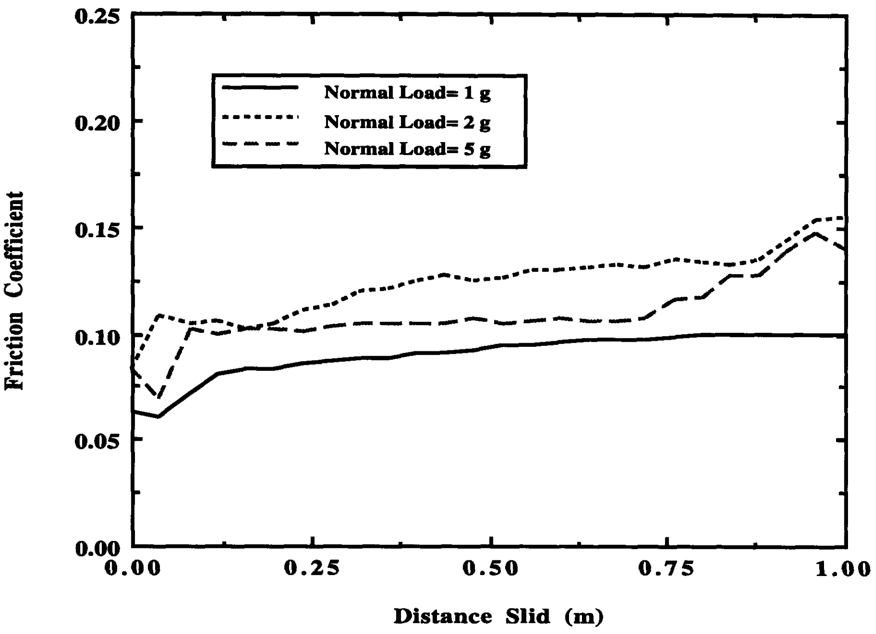

Figure 5.9 Friction coefficient of a 0.11 μm thick film of Bayhydrol 123

The thickness and normal load dependence of friction coefficient of polyurethane films could more clearly be seen in Figure 5.10 and Figure 5.11. In these figures the friction coefficient is plotted as a function of the film thickness for both coating materials. In Figure 5.10 the normal load is 2g and the friction coefficient plot shows three different regimes. The friction coefficient is minimal only in the intermediate zone whereas it reaches higher values if the film is either too thick or too thin. For 1 g normal load as shown in Figure 5.10 the friction coefficient plot shows a declining trend as the film thickness decreases. Although it seems that thinner coatings might have given lower friction under 1 g normal load, due to the poor quality or discontinuity of coatings thinner than 0.09 μm they were not made. Also, the airborne particles or the submicron particles in the solutions play an enhanced role in the frictional behavior of films when their size is comparable to the film thickness. This causes stick-slip during sliding and subsequent tearing of the film when particles are embedded in the surface.

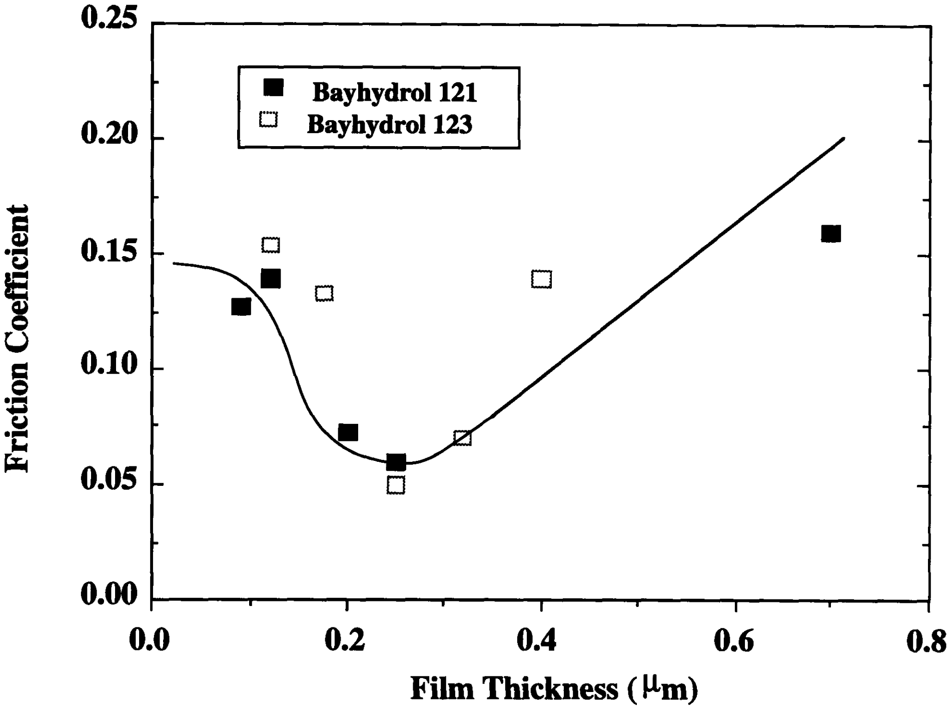

Figure 5.10 Dependence of friction coefficient on film thickness. Load= 2 g.

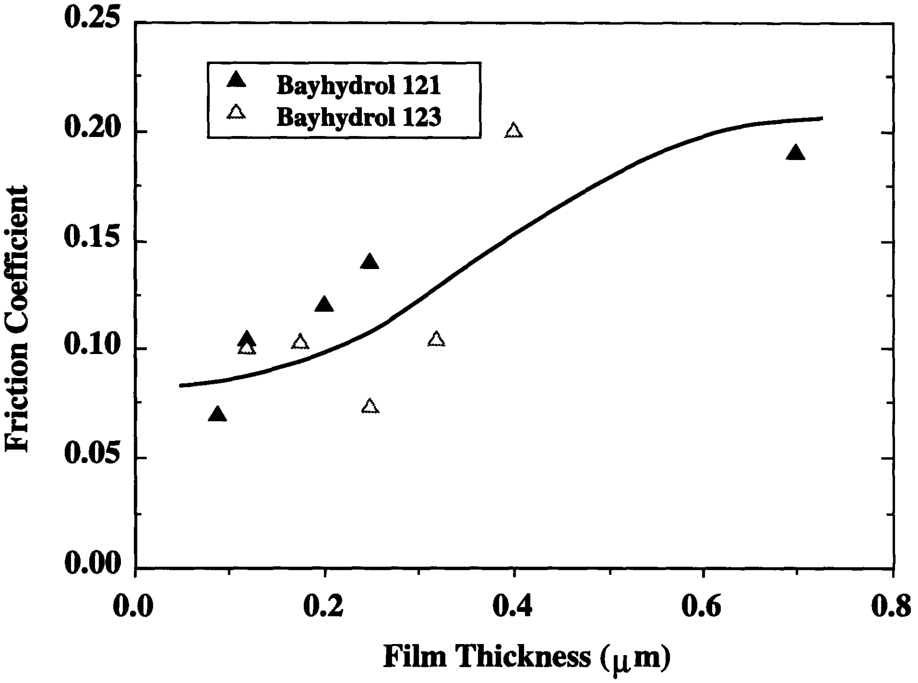

Figure. 5.11 Dependence of friction coefficient on film thickness. Load= 1 g

5.6.2 Effect of Film Crosslinking Density on Friction

Although high compliance of the surface layer is a functional requirement for the ideal surface, the mobility of the molecules at the surface should not be left uncontrolled. The shear deformation experienced by a crystalline polymer surface layer during sliding leads to the orientation of polymer molecules at the interface. When the intermolecular force between the layers of oriented molecules is exceeded by the applied frictional force, wear of these layers is unavoidable. In order to prevent such plastic deformation, the molecules near the surface can be crosslinked without making the entire surface layer overly brittle. Crosslinking of polyurethane films was accomplished through baking and/or exposure to electron beam radiation. Films made of Bayhydrol 121 and baked at 75 °C, 140 °C, and 175 °C for 15 seconds were friction tested as well as the unbaked films. The effect of baking temperature is seen in Figure. 5.12 and Figure 5.13 for 2 and 1 g normal loads respectively. Crosslinking of the surface molecules to a certain degree lowers the friction coefficient due to prevention of intermolecular slip between the polymer chains. However, if the surface is over-crosslinked it becomes brittle which causes fracture during sliding. This in turn increases the friction coefficient.

In addition to increasing the crosslink density of the films by increasing temperature, the samples baked at 140 °C were also electron beam irradiated and friction tested under the same conditions. Tables 5.5 and 5.6 represent the friction coefficient of films of different thicknesses as the irradiation parameters change for 2 and 1 g normal load respectively. It is clear from the results that further increase in the crosslink density by irradiation has not improved the frictional behavior. Instead the surface layer has become too brittle, and from the onset of sliding an extensive fracture of film results in much higher.

Table 5.5 Friction coefficient of samples baked at 140 °C and irradiated with electron beam radiation. Normal Load= 2 g

Film Thickness (μm)	Unirradiated	1 MRad & 2.5 MeV	MRad & 2.5 MeV
0.12	0.140	0.125	0.355
0.20	0.073	0.281	0.420
0.25	0.06	0.155	0.485

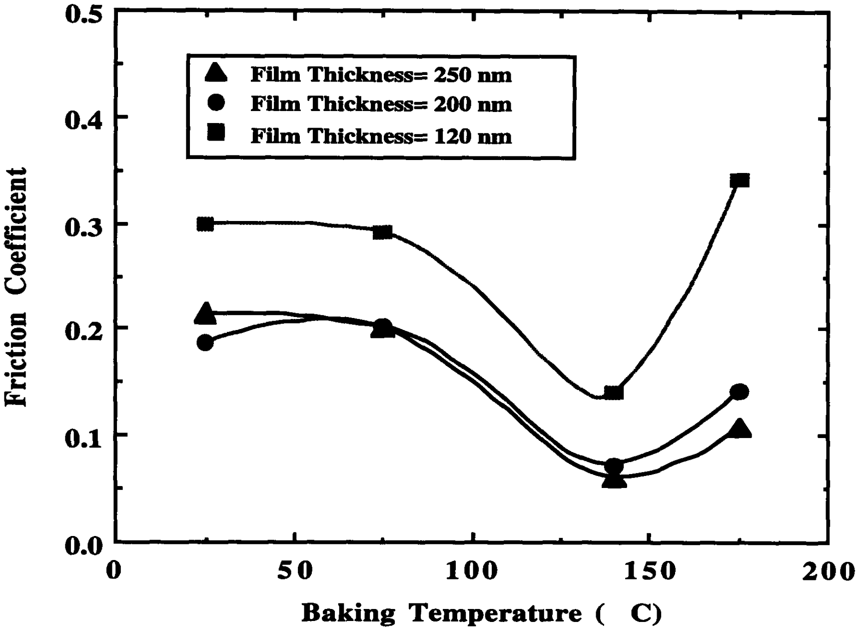

Figure 5.12 Friction coefficient vs. baking temperature for three different thicknesses of Bayhydrol 121 films. Normal Load= 2 g.

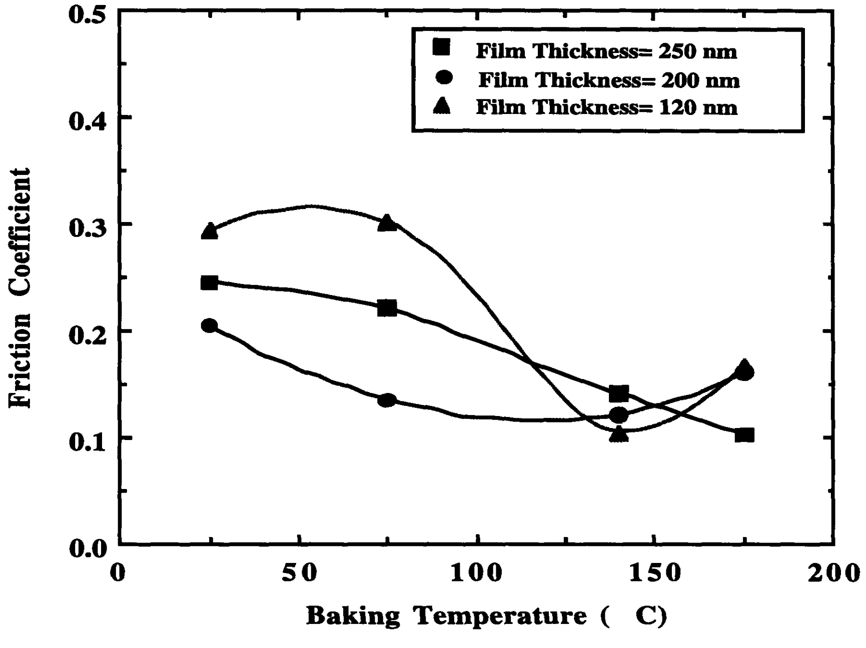

Fig. 5.13 Friction coefficient vs. baking temperature for three different thicknesses of Bayhydrol 121 films. Normal Load= 1 g.

Table 5.6 Friction coefficient of samples baked at 140 °C and irradiated with electron beam radiation. Normal Load= 1 g

Film Thickness (µm)	Unirradiated	1 MRad & 2.5 MeV	5 MRad & 2.5 MeV
0.12	0.104	0.219	0.389
0.20	0.120	0.151	0.416
0.25	0.140	0.195	0.341

friction coefficient compared to unirradiated samples. High friction coefficients of about 0.5 observed from samples irradiated with a dosage of 5 MRad is the result of an early fracture of the interface which produces large wear particles followed by plowing. The damage to the surface after the tests for all irradiated samples could be seen by the naked eye.

The crosslinking density of the samples baked at different temperatures or those of the irradiated samples were not measured in this study. However, the data supports the argument that there is a minimal crosslinking density for a certain load and film thickness with respect to the value of friction coefficient.

5.6.3 Effect of Contact Geometry on Friction

The contact geometry in the previous experiments consisted of a 4 mm ball on the smooth surface of the polyurethane coatings. However, practical sliding bearings utilize a large contact area which gives rise to many tribological phenomenon, such as entrapment of wear debris at the interface. In order to take a step toward understanding of the behavior of the surfaces developed in this study, the effect of the increasing the contact geometry was investigated. A flat on flat geometry is an appropriate contact geometry to simulate that commonly found in practical bearings. However, the film was scratched by the edges of the sample due to the misalignment caused by the pivoting action of the cantilever of the tester. An alternative method is to use a large radius ball sliding against the polyurethane coated samples. A borosilicate crown glass bi-convex lens with a 76.6 mm radius of curvature was used as a pin to perform friction tests. The plot of friction coefficient is shown in Figure 5.14 for 20 g normal load and 0.25 µm thick films of Bayhydrol 121 and Bayhydrol 123. The stick-slip phenomena was observed occasionally during the tests.

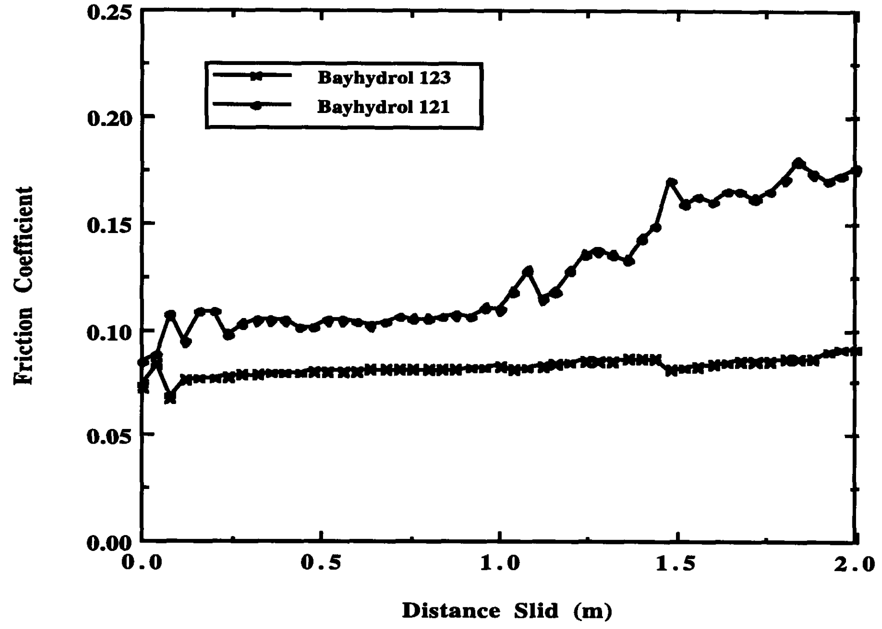

Fig. 5.14 Friction coefficient vs. distance slid for 0.25 μm thick films. Ball radius = 76.6 mm, Normal Load= 20 g.

An examination of the surfaces after the tests showed that at some spots the coatings were totally removed from the silicon wafers. These spots are the locations on the coating where airborne particles, contaminant particles in the polyurethane solutions, or particles in the deionized water are present in the film. If the size of these particles is comparable to the film thickness they can cause the removal of the film through a mechanism similar to plowing by wear particles.

5.6.4 Atomic Force Microscopy of Wear Tracks

Surfaces of polyurethane films were examined using an atomic force microscope in the tapping (non-contact) mode to prevent any damage to the surface during scanning. In the tapping mode as the silicon nitride tip of the AFM scans over the surface without contact it taps the surface with a certain amplitude and frequency. The scanning frequency was in the range of 0.5 to 2 Hz for all AFM studies. Figure 5.15 and Figure 5.16 show the two and three dimensional views of a 5X5 μm area of the non-tested surfaces of 0.25 μm thick films made of Bayhydrol 121 and Bayhydrol 123, respectively. The RMS and the mean roughness of surfaces were in the range 2 to 4 nm. In the three dimensional pictures the features of the surfaces are enhanced about 20 times in the z-direction.

Surfaces of these samples tested with 2 g normal load were also examined in the AFM to find out if any damage was made to the surface during sliding. Figure 5. 17 is the 3-D view of a 0.25 μm thick film of Bayhydrol 121 tested under 2 g normal load with a friction coefficient of 0.06. There appears to be a plowing groove on the surface , about 5 μm wide. Also, compared with the non-tested surface, the mean and the RMS roughness of this surface have increased to the 5 to 9 nm range.

The unbaked and the irradiated films of Bayhydrol 121 were also examined in the AFM and their 3-D views are shown in Figure 5.18 and Figure 5.19 respectively. These images show extensive damage to the surface during the sliding.

A significant observation from the AFM images is that these surfaces which exhibited higher friction coefficients have experienced higher damage. The amount of damage to those surfaces with low friction coefficients of about 0.05 is minimum, but not zero. This shows that even at such low values of friction coefficient there still exists a contribution by the mechanical interactions in friction. Also, the unbaked samples with a friction coefficient of about 0.2 tend to act as a lubricant in reducing the friction by the ease of shearing at the asperities. This causes numerous plowing grooves on the surface as shown in Figure 5.18. The irradiated samples show a rather different mode of damage, that of extensive fracture of the film (Figure 5.19). Since the fractured segments of the film are entrapped at the sliding interface they cause severe plowing and result in a friction coefficient as high as 0.5. The friction coefficient between the glass ball and the silicon wafer is only 0.3.

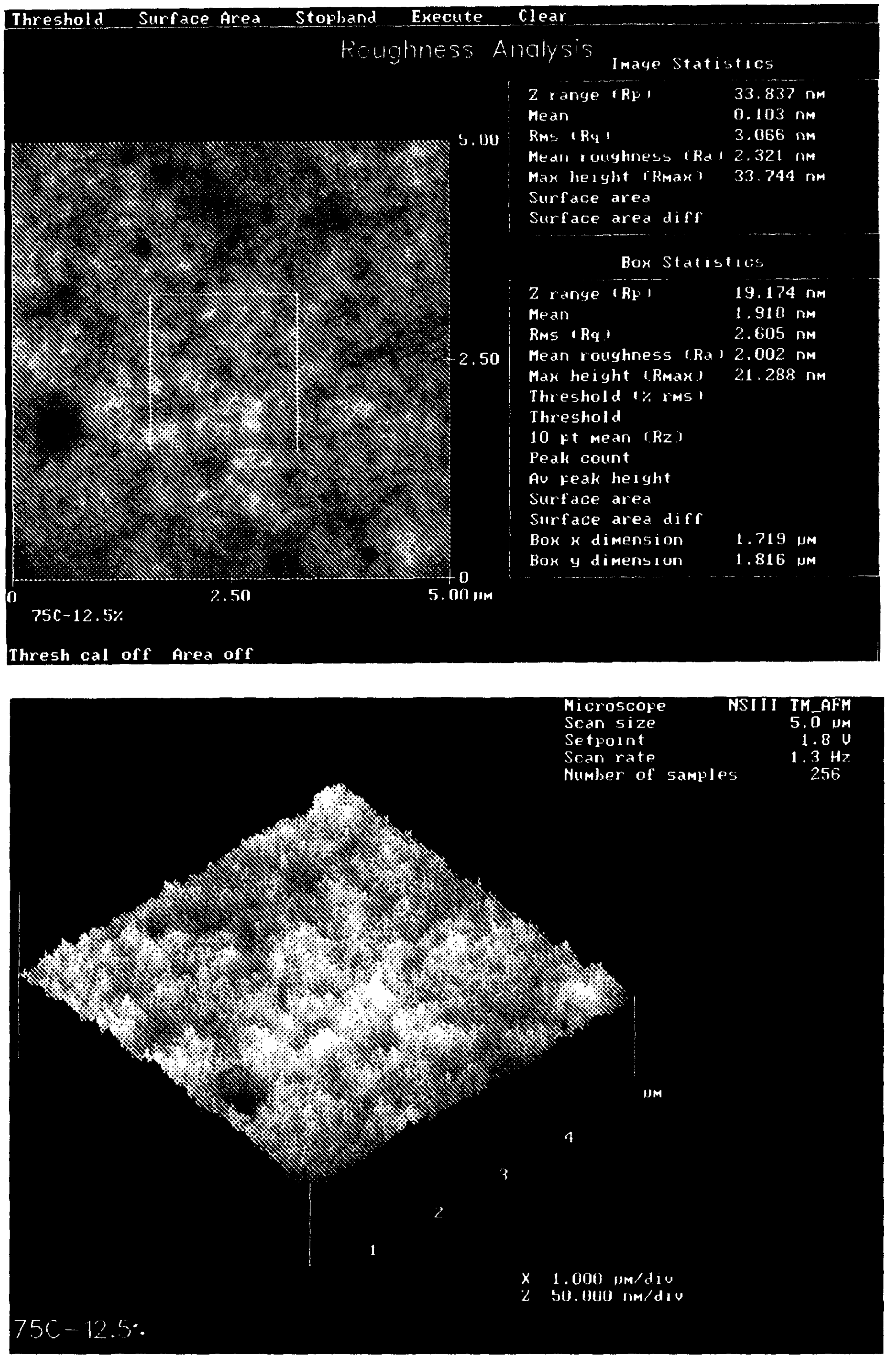

```
Image Statistics

Z range (Rp)              33.837 nm
Mean                       0.103 nm
Rms (Rq)                   3.066 nm
Mean roughness (Ra)        2.321 nm
Max height (Rmax)         33.744 nm
Surface area
Surface area diff

Box Statistics

Z range (Rp)              19.174 nm
Mean                       1.910 nm
Rms (Rq)                   2.605 nm
Mean roughness (Ra)        2.002 nm
Max height (Rmax)         21.288 nm
Threshold (% rms)
Threshold
10 pt mean (Rz)
Peak count
Av peak height
Surface area
Surface area diff
Box x dimension            1.719 µm
Box y dimension            1.816 µm
```

```
Microscope          NSIII TM_AFM
Scan size                 5.0 µm
Setpoint                   1.8 V
Scan rate                 1.3 Hz
Number of samples          256
```

```
X    1.000 µm/div
Z   50.000 nm/div
```

Figure 5.15 Two and three dimensional views of the surface of a 0.2 µm thick coating of Bayhydrol 121 on silicon taken in Atomic Force Microscope in tapping mode.

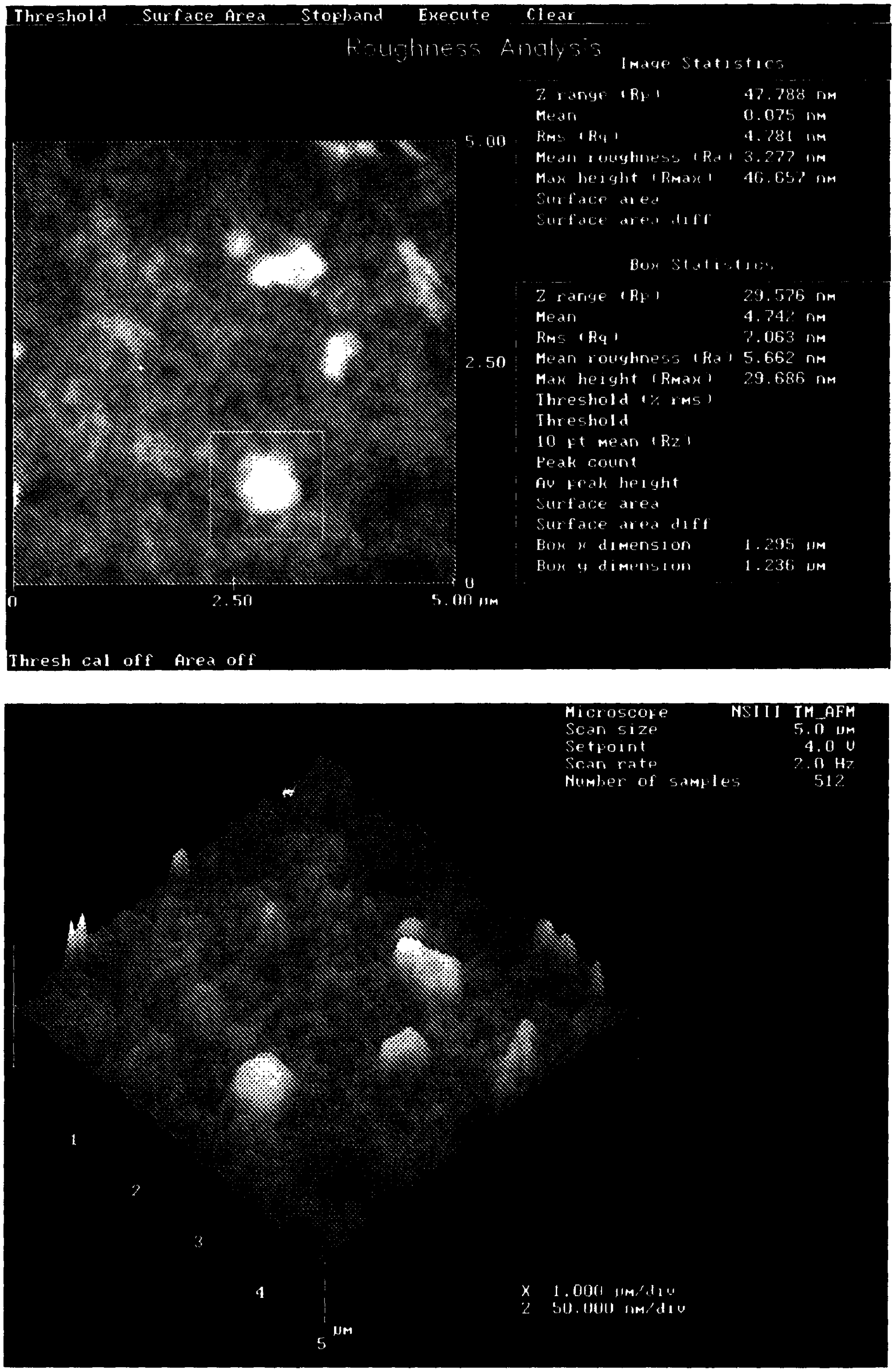

```
               Image Statistics
Z range (Rp)                47.788 nm
Mean                        0.075 nm
Rms (Rq)                    4.781 nm
Mean roughness (Ra)         3.277 nm
Max height (Rmax)           46.657 nm
Surface area
Surface area diff

               Box Statistics
Z range (Rp)                29.576 nm
Mean                        4.742 nm
Rms (Rq)                    7.063 nm
Mean roughness (Ra)         5.662 nm
Max height (Rmax)           29.686 nm
Threshold (% rms)
Threshold
10 pt mean (Rz)
Peak count
Av peak height
Surface area
Surface area diff
Box x dimension             1.295 µm
Box y dimension             1.236 µm
```

```
Microscope             NSIII TM_AFM
Scan size                    5.0 µm
Setpoint                      4.0 V
Scan rate                    2.0 Hz
Number of samples               512
```

Figure 5.16 Two and three dimensional views of the surface of a 0.25 µm thick coating of Bayhydrol 123 on silicon taken in Atomic Force Microscope in tapping mode.

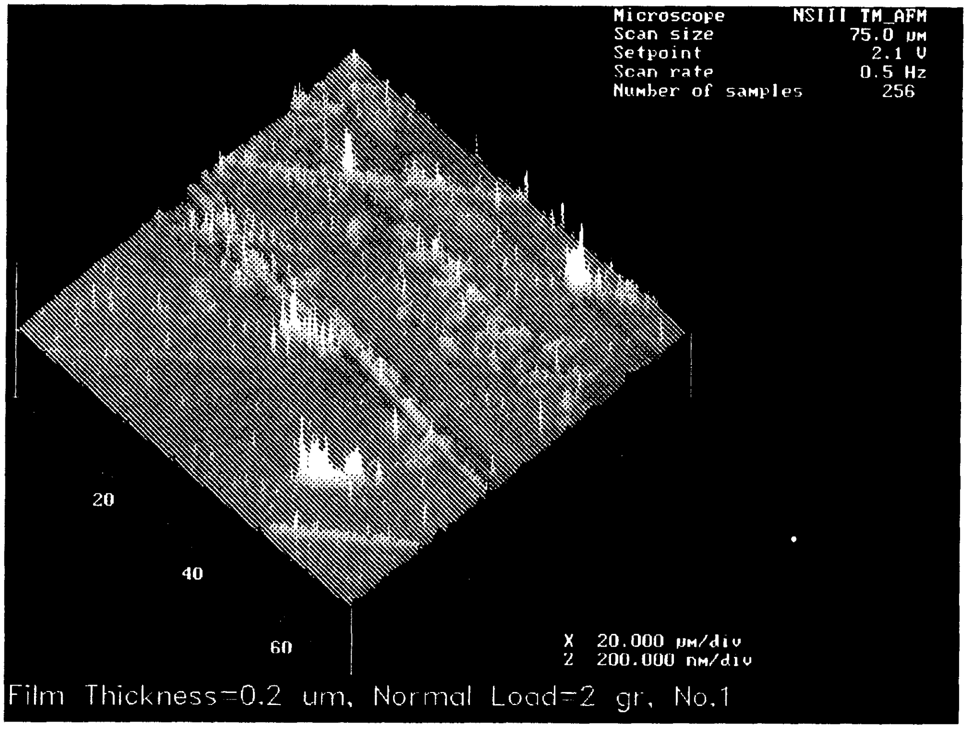

Figure 5.17 Three dimensional view of a wear track on a 0.25 µm thick film of Bayhydrol 121 baked at 140 C. Normal Load= 2 g.

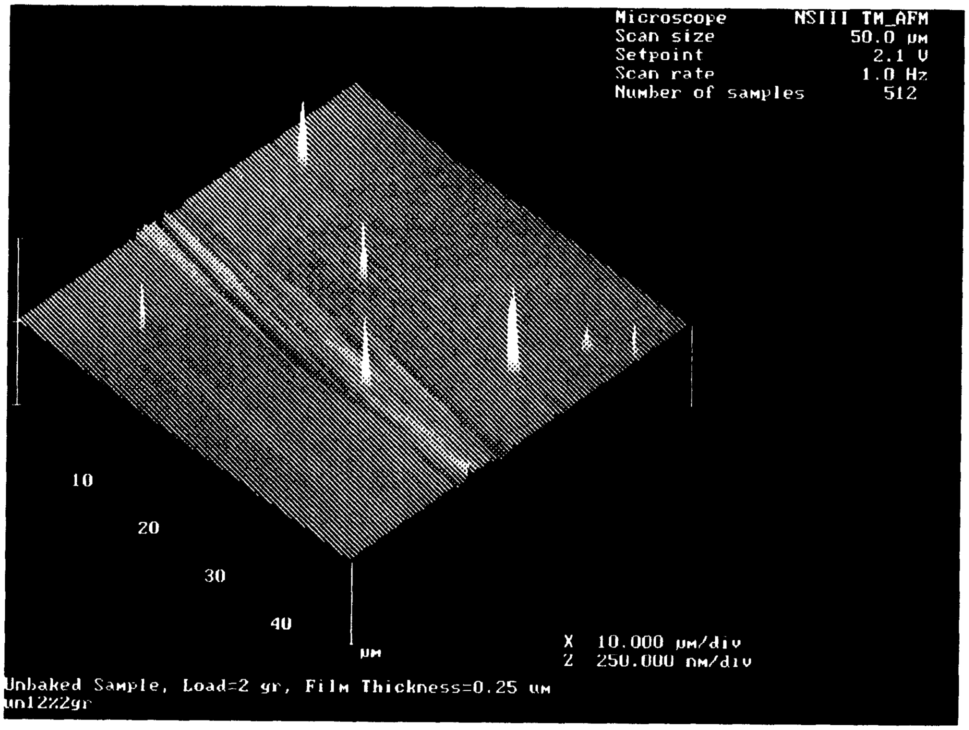

Figure 5.18 Three dimensional view of a wear track on a 0.25 µm thick unbaked film of Bayhydrol 121. Normal Load= 2 g.

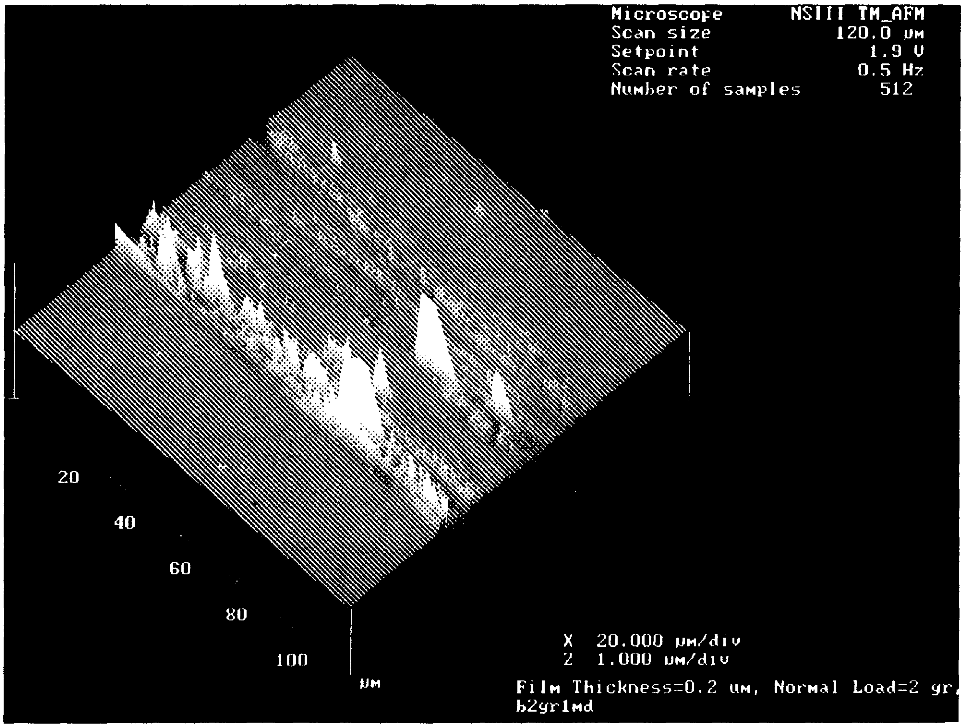

Figure 5.19 Three dimensional view of a wear track on a 0.25 μm thick film of Bayhydrol 121 baked at 140 C and electron beam irradiated with 2.5 MeV at a dosage of 1 MRad. Normal Load= 2 g.

5.7 The Contribution of Hysteresis Losses to Friction of Polyurethane Films

Microscopic plastic deformation of the surface observed in AFM, adhesion and hysteresis contribute to the low friction obtained between the polyurethane films and the rigid counterface. The hysteresis is a bulk phenomenon whose origin is the viscoelastic behavior of elastomers. In general, the magnitude of the hysteresis component of friction in a given sliding system depends on the film thickness, load, sliding speed, and the material properties. In a simple model for a spherical indentor it can be assumed that the difference between the elastic work done in deforming the elastomer in front of the indentor and the recovered work from the rear represents the hysteresis loss.

The elastic work done by a sliding sphere on an elastomeric film can be estimated from the force exerted on the front half of the sphere by the horizontal component of the interfacial forces. If the whole of the elastic energy were lost by hysteresis this would correspond to the force required to move the ball. Using the these assumptions and the geometry given in Figure 5.20, Greenwood and Tabor [16] derived the total horizontal force in the direction of the motion as:

$$F = \int_0^a \frac{2}{\pi} \frac{pr}{R} \pi dr = \int_0^a pr^2 dr \tag{5.2}$$

where

p : contact pressure at a distance of r from the center
R : ball radius
a : radius of the contact circle

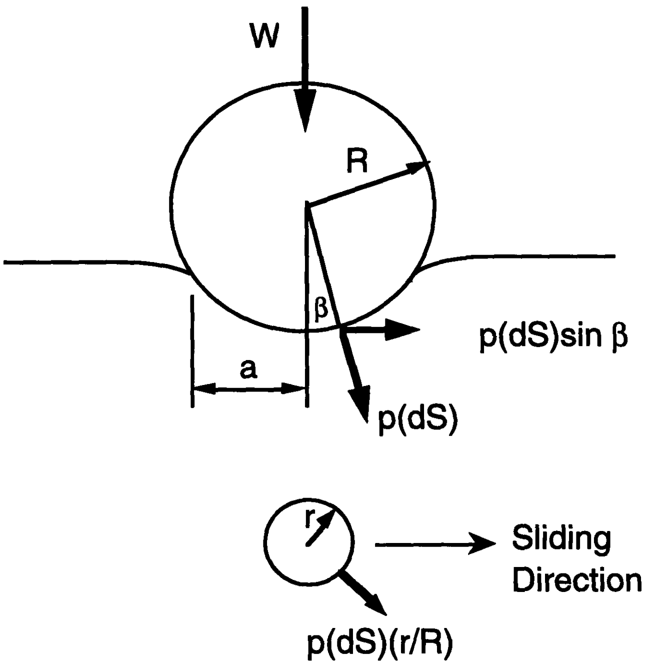

Figure 5.20 Horizontal component of force over the front half of the circle of contact for a rigid sphere indenting an elastomer.

If the thickness of the elastomer is large, the contact pressure could be found by the Hertzian contact solution. However, in the case of a thin polyurethane film the contact pressure must be found from the solution of contact problems for an elastic thin layer bonded to a rigid substrate. Such problems have been studied theoretically and numerically for a variety of contact geometry and loading [17]. Although the theoretical solutions involve approximations and have assumed the contact to be "frictionless", they provide a means of estimating the contact pressure and the deformation of the surface layer. Hui and Demsey [18] presented the solution of an axisymmetric contact of an elastic layer with a rigid base under it by using an exponential series approximation, and an infinite integral containing two Bessel functions. In their solution, the surface displacement of an elastic layer w(r) due to an axisymmetric surface load p(r) is given by

$$w(r) = \frac{1}{E_1}\int_0^\infty p(s)G(s,r)ds \tag{5.3}$$

$$G(s,r) = \frac{2s}{d}\int_0^\infty f(\alpha)J_0(\alpha r/d)J_0(\alpha s/d)d\alpha \tag{5.4}$$

where

$$f(\alpha) = \frac{1-2e^{-2\alpha}+e^{-4\alpha}}{1+4\alpha e^{-2\alpha}-e^{-4\alpha}} \tag{5.5}$$

$$E_1 = \frac{E}{1-\upsilon} \tag{5.6}$$

where E, and υ are the elastic modulus and the Poisson's ratio of the layer, respectively, while d is the layer depth. In equation (5.4) J_0 is the Bessel function of zero order. For a rigid sphere on a layer bonded to a rigid substrate, shown in Figure 5.21, the boundary conditions on the upper surface of the layer are

$$\begin{aligned} &w(r) = \delta - (r^2/2R), \quad p(r)\rangle 0, \quad for \quad r\langle a \\ &w(r)\rangle\delta - (r^2/2R), \quad p(r) = 0, \quad for \quad r\rangle a \end{aligned} \tag{5.7}$$

where a is the contact radius and R is the radius of the sphere.

The corresponding analytical solutions for the contact pressure, the contact radius and the indentation depth are

$$\frac{2p(r)}{p_{ave}} = 3\sqrt{1-(r/a)^2} \tag{5.8a}$$

$$\frac{\pi a^3 E_1}{RW} = \frac{4(1-2\nu)}{(1-\nu)^2}\frac{d}{a} \tag{5.8b}$$

$$\frac{2\pi\delta a E_1}{W} = \frac{4(1-2\nu)}{(1-\nu)^2}\frac{d}{a} \tag{5.8c}$$

The solution presented here is valid only when the layer depth is very small in comparison with the contact radius, i.e.,

$$({}^{d}\!/_{a})\langle 0.1 \tag{5.9}$$

Since the radius of contact for the polyurethane films under the loading applied in this study is in the order of few micrometers and their thickness is a fraction of a micrometer, the above condition is satisfied.

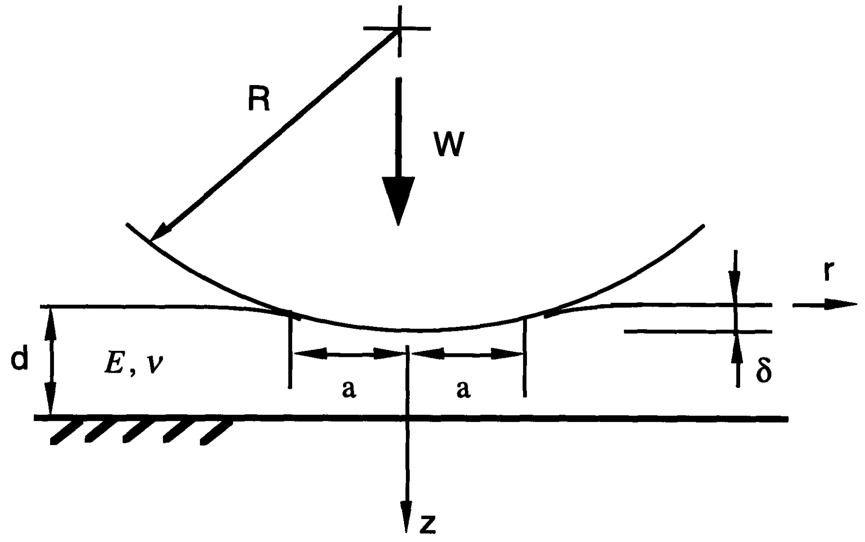

Figure 5.21 Axisymmetric contact problem of a rigid sphere on a complaint layer.

Knowing the expression for the contact pressure from eq. (5.8a) and by substitution into eq. (5.2) the total horizontal force in the direction of sliding is

$$F = \frac{3W}{16R}\left\{\frac{4(1-2\nu)(1+\nu)RW}{\pi E(1-\nu)}d\right\}^{0.25} \tag{5.10}$$

In moving forward a unit distance the elastic work done in the horizontal direction is thus:

$$\varphi = F \tag{5.11}$$

As the sphere moves forward on the film it stores an amount of elastic energy per unit distance of travel on the oncoming material. If it is assumed that a fraction k of the input energy is lost as a result of elastic hysteresis in the elastomer, the work lost per unit distance of travel is k. This amount of work is provided by the frictional force F. Therefore the contribution of the friction coefficient due to the hysteresis losses is:

$$\mu_{hysteresis} = \frac{k\varphi}{w} \tag{5.12a}$$

$$\mu_{hysteresis} = \frac{3k}{16R}\left\{\frac{4(1-2\nu)(1+\nu)RW}{\pi E(1-\nu)}d\right\}^{0.25} \tag{5.12b}$$

The values of friction coefficient determined by eq. (5.12b) are plotted in Figure 5.22 vs. the film thickness under 2 g normal load for Bayhydrol 121 and Bayhydrol 123. In general the friction coefficient due to hysteresis is very small based on the simple model developed here. The main reason for the small contribution of hysteresis is due to the submicron thickness of the films. From the plot it can be concluded that the contribution of hysteresis in the friction coefficients of 0.05 obtained with the films is less than 5%.

5.8 Influence of External Particles on Friction of Polyurethane Films

External particles could be found in the polyurethane film as a result of impurities in the solutions or due to the airborne particles in the environment.

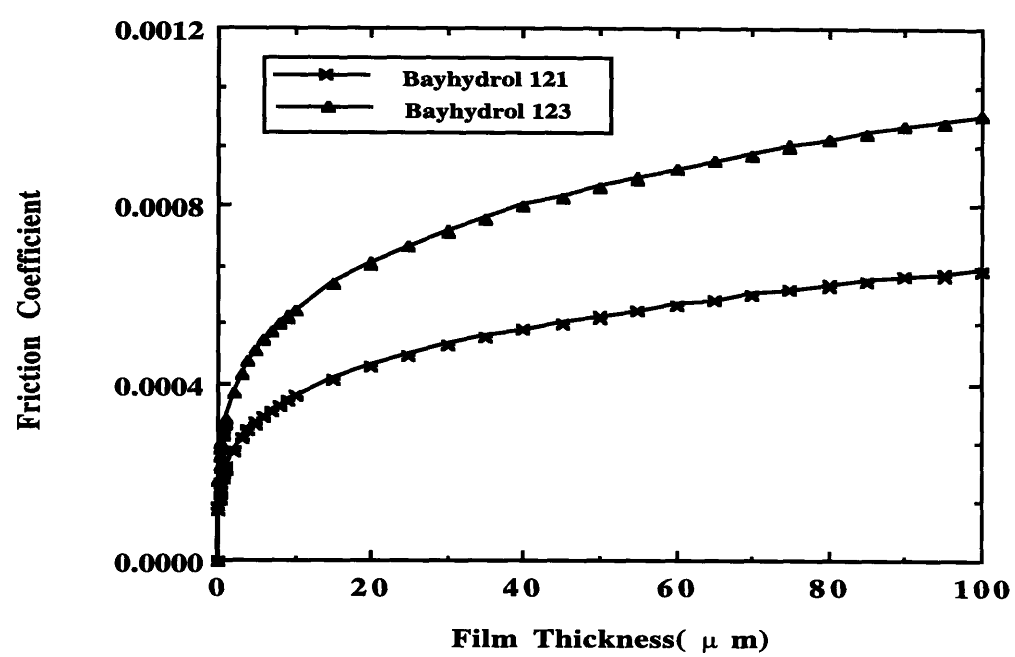

Figure 5.22 Contribution of hysteresis losses to the friction coefficient of thin elastomeric layers.

These particles can affect the friction of such films especially if their size is comparable to the coating thickness. When such particles are present in a sliding system they plow the coating and result in a local removal of the film and can cause high friction. The problem becomes magnified when the apparent area of contact increases due to the use of a large radius ball or a flat surface. For a small radius ball, the probability of entrapment of a particle at the interface is much slighter than that of a flat counterface of a large radius ball. This might be the reason for the high friction coefficients observed with a glass ball of radius 76.6 mm. The higher probability of encountering particles by a large counterface area is shown in Figure 5.23. The reasoning is validated based on the examination of samples tested with a 76.6 mm radius ball which showed the removal of the film at some spots.

Although the adverse effects of such particles on friction is magnified when the counterface is nearly flat, it does not entirely remove the possible contribution to the low friction coefficient of 0.04 which was obtained with small radius balls.

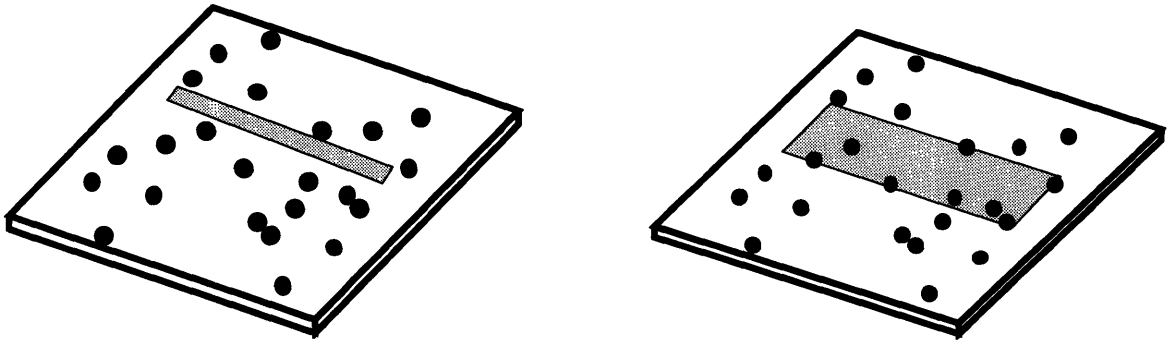

(a) Wear track of a small radius pin **(b) Wear track of a large radius pin**

Figure 5.23 Location of external particles in wear tracks of a small radius ball (a) and a large radius ball (b).

5.9 Dip-Coating Method and Drying Defects

The choice of a coating technique is a key factor to the surface characteristics of a deposited film [19]. There are many considerations in choosing a particular coating process such as: number of coating layers, wet layer thickness, coating consistency, substrate, and so on. One of the oldest techniques is to dip the web into the coating solution and then withdraw. This process can lead to a stable coating surface when the coating speed is sufficiently low and the required thickness is not large. However, the uniformity of the film, especially when there in no scraper in the coating process to remove the excess material, is not well controlled.

A dip-coating technique always involves a drying process which can cause different types of defects in a coating [20]. These can be, stresses-induced, surface tension driven, contamination related, or film-substrate bond related defects. For example many different types of defects such as; holes in the film, and craters are the result of airborne particles, grease, or other contaminations. The starry night defects, curling, and mudcracking defects are among those induced by internal stress in the film due to improper drying [21,22]. Also drying process can cause the adhesive failure or delamination between the coating and the substrate. From the tribological point of view, a film without any residual stresses is favored. Since the drying process causes such stresses in the film, it is important to know the approximate magnitude of these internal stresses.

5.10 Residual Stresses in Films

The magnitude of the internal stress developed in a polymer coating is presented based on a model which assumes that the residual stress in the film is solely due to the difference between the volume fraction of the solvent at which the film solidifies and the volume fraction of the solvent in the dry film [23]. Prior to the solidification, the coating can flow and allow the volume change due to the solvent evaporation. After the film is solidified, the coating material can no longer flow, and the loss of the solvent results in the internal tensile stress in the plane of coating. The internal stress can then be determined by

$$\sigma = \left(\frac{E}{1-\nu}\right)\left(\frac{\Delta V}{3V}\right) \cong \left(\frac{E}{1-\nu}\right)\left(\frac{C_s - C_r}{3}\right) \tag{5.13}$$

where

E : elastic modulus of coating
ν : Poisson's ratio of coating
ΔV : volume of solvent loss after solidification
V : volume of coating at solidification
C_r : volume fraction of solvent retained in dry film
C_s : volume fraction of solvent at solidification

The solidification point occurs when the concentration of solvent has reduced to a point where the large scale relative molecular motion in the solution is frozen. This point can be identified as the solvent concentration at which the ambient temperature becomes the glass transition temperature of the polymer solution. In order to calculate the volume fraction of the solvent retained in the dry film an experimental procedure was followed which involved the measurement of the weight loss of solvent during the coating process.

A simple way used here is to replace V which is the volume of the coating at the solidification point by V^* which is the volume of the coating after baking. Since the volume of the coating gets smaller as it shrinks during the baking, the residual stress calculated using V^* will be higher than that determined by eq.(). In order to calculate the residual stresses in the coating using this approximation, one must know the volume of the solvent loss from the coating after the solidification and the volume of the final coating. The latter can be determined from the coating geometry. The former, however, needs the solidification point to be identified. Again the approximation used here is to assume that due to the very small thickness of the film, the solidification happens almost right after the silicon wafer is withdrawn from the solutions. The volume of the solvent from this point to the final drying stage (ΔV^*) can be determined from the weight loss of the coating and the density of the solvent.

Based on the above assumptions silicon wafers were weighed and then coated with Bayhydrol 121 solutions of 10% and 12.5% concentrations. They were again weighed 60 seconds after they were withdrawn from the solution. The samples were left in the clean room for 15 hours and weighed after this period. The coatings were baked at 140 C for 15 seconds. After baking they were taken out from the oven and left in the clean room for 15 minutes to cool down and finally weighed. The results are shown in Table 5.7.

Table 5.7 Numerical values of the coating's weight at the solidification point (W_s), coating weight after baking (W_d), ratio of differential solvent volume per coating volume ($\Delta V^*/V^*$), and residual stress (σ).

W_s (kg)	W_d (kg)	ΔV^* (m^3)	$\Delta V^*/V^*$	σ (Pa)
1.20416	1.20414	2e-11	0.008368	195258
2.42453	2.42450	3e-11	0.010149	236806

The values of residual stresses for two different film thicknesses are approximately equal. These stresses are well below the tensile strength of the polyurethane coating and therefore the possibility of cracking [24,25] of the film at the surface is remote.

In a typical sliding situation due to the tensile stress developed behind the slider precludes an internal tensile stress at the surface . If the magnitude of such stress is high it can cause cracking of the film during the sliding. However, in the polyurethane films the internal stress in the film is fairly low.

5.11 Conclusions

The idea of using a covalent, compliant film on a hard substrate to minimize the mechanical interactions during the sliding has been presented. Friction coefficients as low as 0.04 obtained with such surfaces indicate that in the absence of gross mechanical interactions the contribution of other components to friction such as hysteresis losses and adhesion is very small. The AFM views of friction tested samples showed that the nanoscale plowing of the surfaces was not altogether avoided during the sliding and contributed to friction.

For a given normal load, the film thickness is a critical factor in the frictional behavior of elastomeric films on a hard substrate. In the plots of friction coefficient versus the film thickness there appears to be a regime in which friction is minimum. In this regime the hysteresis losses throughout the thickness are minimum and the film is not easily removed from the substrate due to a high shear gradient in the film as a result of friction.

Crosslinking of surface molecules causes the formation of intermolecular bonds between polymer chains. When there a minimum crosslinking the deformation mode is similar to that occurs in solid lubrication. Plowing by hard asperities or the interplanar slip are the dominant mechanism friction and energy dissipation. Friction coefficients as high as 0.15-0.25 obtained from the surfaces with low crosslinking density along with the large amount of damage detected in AFM support this idea. As the crosslink density increases the number of intermolecular bonds increases which results in increased stiffness. Based on the solid lubrication theory it is expected that the friction coefficient will increase. However, the experimental result proves the opposite. A minimum friction coefficient as low as 0.04 is reached at a certain crosslinking density. The deformation mode is assumed close to elastic. In this mode the energy dissipation in minimum and is mainly due to adhesion and hysteresis losses, although the mechanical interactions at the surface layer are not entirely eliminated. If the crosslink density is further increased the film becomes too brittle. The deformation mode will be mainly fracture, either at the surface or at the film-substrate interface which results in a high friction coefficient. Hard wear particles produced during sliding plow the surface and contribute to friction.

The friction coefficient of 0.5 obtained with irradiated film is even higher than that obtained between glass and silicon; about 0.3. This indicates the severe role of plowing by hard wear particles and the continuous fracture of the film. The AFM image of irradiated film confirms the tremendous amount of damage to the surface.

The friction coefficient of surfaces developed in this study is approximately an order of magnitude smaller than that of undulated surfaces used in the experimentation of geometrically constrained sliding systems. There is still room for improvement in lowering of friction. This may be achieved through the optimization of the sliding system with respect to the properties of the elastomer used and the characteristics of the surfaces. At this stage it can be said that even a friction coefficient of 0.04 is not truly a material property of the surface, but instead it is a result of mechanical interactions at the nanoscale level, adhesion, and hysteresis. The next development in this area would be to make practical bearings with a large contact area and high load capacity.

One other important issue is the durability of the such surfaces in order to satisfy the no-wear loss criterion. The experiments conducted here were only for a small range of motion and limited number of cycles. Although ideally the concept of ultra low friction surfaces through the breakage of van der Waal's forces means that there will be no wear loss, the AFM studies showed a certain amount of damage to the surface due to sliding. This is a challenging frontier for further development in this area. Also, the strength of the substrate-film bond is of great importance for a better understanding of the friction of elastomeric-coated surfaces.

5.9 References

[1]Trylinski, W., Fine Mechanisms and Precision Instruments, Pergamon Press-Wydawnictwa Naukowo-Techniczne, Oxford, Warsaw, 1971.

[2] Rymuza, Z., Tribology of Miniature Systems, Elsevier Science Publishers B.V., Netherlands, 1989.

[3] Gohar, R., "Low friction rolling element bearings", Wear, Vol. 104, 1985, pp. 309-315

[4] Bushan, B., Phelan, M.R., "Frictional properties as a function of physical and chemical changes in magnetic tapes during sliding", ASLE Transactions, Vol. 29, 1986, pp. 402-407

[5] Li, Z., Rabinowicz, E., and Saka, N., " The stiction between magnetic recording head and thin film disks", *Tribology and Mechanics of Magnetic Storage Systems*, STLE SP-26, 1989, pp. 64-70.

[6]Dixon, F.C., and Rickert, U.G., "Tissue tolerance to foreign materials", J. Am. Dent. Assoc., Vol. 20, 1958, pp. 1933.

[7] Spector, M., Cease, C., and Tong-Li, X., "The local tissue response to biomaterials", Vol. 5, No. 3, 1989, pp. 269-295.

[8] Kim, D. E., and Suh, N.P, "Frictional Behavior of extremely smooth and hard solids", Wear, Vol. 162-164, 1993, pp. 873-879.

[9] Suh, N.P., "In pursuit of Lower limit of friction coefficient in dry sliding", ASME annual Meeting, New Orlando, 1993.

[10] Braithwaite, E.R., and Hickman, J., "Dry film lubrication of metals", Metal Industries, Vol. 104, 1964, pp. 190-194.

[11] Deacon, R.F., and Goodman, J.F., "Lubrication by lamellar solids", Proc. Roy. Soc., London, Series A. Vol. 243, 1958, pp. 464-482.

[12] Haltner, A.J., and Oliver, C.S., "Frictional properties of some solid lubricant films under high load" , Journal of Chemical Engineering Data, Vol. 6, 1961, pp. 128-130.

[13] Howard, P.S, Investigation of the Friction of Thin Polyurethane Coatings, S.M. Thesis, Mechanical Engineering Department, MIT, 1993.

[14] Gugliemi, M., Colombo, P., Peron, F., and Mancinelli, L., "Dependence of thickness on the withdrawal speed for SiO_2 and TiO_2 coatings obtained by dipping method", Journal of Materials Science, Vol. 27, 1992, pp. 5052-5056.

[15] Ruschak, K. J., "Coating flows", Annual Review Fluid Mechanics, Vol. 17, 1985, pp. 65-89.

[16] Greenwood, J.A, and Tabor, D., "The friction of hard sliders on lubricated rubber: The importance of deformation losses", Proc. Roy. Soc., Vol. 71, 1958, pp. 989-999.

[17] Matthewson, M. J., "Axi-symmetric contact on thin compliant coatings", Journal of Mechanics and Physics of Solids, Vol. 51(2), 1981, pp. 89-113.

[18] Hui, L., and Dempsey, P., "Axisymmetric contact of an elastic layer underlain by rigid base", International Journal for Numerical Methods in Engineering, Vol. 29, 1990, pp. 57-72.

[19] Cohen, E. D., Gutoff, E. B., "Modern coating and Drying Technology", VCH Publishers, Inc., New York, NY, 1992.

[20] Bierwagen, G. P., "Film formation and mudcracking in latex coatings", Journal of Coating Technology, Vol. 51(658), 1979, pp. 117-126.

[21] Schoff, C. K., "Coating defects: causes and analysis", 9th International Conference on the Coating Sciences and Technology, 1979, pp. 173-195.

[22] Cary, J. D., and Gutoff, E. B., "Analyze the drying defects of aqueous coatings", Chemical Engineering Progress, Vol. 51(2), 1991, pp. 73-79.

[23] Croll, S. G., "The origin of residual internal stress in solvent-cast thermoplastic coatings", Journal of Applied Polymer Science, Vol. 23, 1979, pp. 847-858.

[24] Sato, K., "The internal stress of coating films", Progress Org. Coatings, Vol. 8, 1980, pp. 143-160.

[25] Beuth Jr, J. L., "Cracking of thin bonded films in residual tension", International Journal of Solids Structure, Vol. 29(13), 1992, pp. 1657-1675.

Chapter 6

Application of Ultra-Low Friction Surfaces to Sliding Contact Bearings

6.1 Introduction

In the previous chapter the concept of ultra-low friction surfaces was shown to provide a means for minimizing the mechanical interactions at the surface layer, such as plowing by hard asperities and/or wear particles. Although friction coefficients as low as 0.04 were achieved with pin-on-disk experiments, the application of such surfaces to practical bearings requires further investigation. From the engineering point of view, achieving such a goal has many implications, limited only by one's imagination. Ultra-low friction sliding bearings could be the simplest, the least expensive bearings not requiring a lubricant. Such bearings could be used in extremely clean environments and could replace ball bearings where space constraints do not permit bearing housings. All these characteristics lead to very stiff precision machine elements without restriction on the size of the bearings.

However, the geometrical differences between a ball-on-flat and the practical bearing configurations introduce new problems for the surface engineer. These problems stem from the frictional behavior of materials at the micro-, nano-, and atomic scales. The theoretical models presented for one scale cannot describe the nature of surface interactions at another scale. Also these models do not agree with the experimental results at higher or lower scales.

The good agreement observed between the low friction coefficients achieved with polyurethane coatings (0.04-0.06 with 1-5g normal load) and those reported in friction experiments in AFM [1] under microgram normal loads can be considered an important step toward the development of an ultra-low friction sliding bearing. The next step is to understand the topographical, geometrical, and boundary condition differences between a pin-on-disk experiment and a practical bearing. A smooth simple shaft/bushing bearing is a good candidate for coating with polyurethane dispersions in order to apply the ultra-low friction concept to practical sliding bearings. However, the roughness of practical bearing surfaces will be greater than that of the silicon wafers used previously. Since only one of the surfaces will be coated by polyurethane coatings the rough surface of the counterface is expected to greatly affect the friction of such bearings.

6.2 Contact Between Rough Surfaces

The contact area between rough surfaces is limited to a very small portion of the apparent area of contact. When solid bodies are brought together, contact will initially occur at a few high asperities on either surface. As the normal load increases, the deformed high asperities and the newly formed junctions provide support for the increased normal load. Contact stresses between asperities are generally high and may result in localized plastic deformation. In an elementary analysis of the contact between two rough surfaces one can assume that the asperities of the surface are spherical with a constant radius and height, and that each asperity deforms independently of the others [2]. Therefore the hertzian contact solution can be applied, and the area of contact for the case of pure elastic contact is

$$A \propto W^{2/3} \tag{6.1}$$

and for the case of perfectly plastic contact the true area of contact is known to be proportional to the normal load

$$A \propto W \tag{6.2}$$

The simplified picture of contact presented above only gives the lower and the upper bounds of contact area. However, real surfaces are neither composed of uniform asperities of a single radius and height nor do the asperities deform independently. The random nature of surface roughness imposes the need for investigation of the behavior of a statistically distributed set of asperities when they come into contact.

6.3 Statistical Model of Contact Between Rough Surfaces

The emphasis of this section is to concentrate on the elastic limit involved in the contact of rough surfaces under a given load. It is well accepted that the real area of contact is established when a sufficient number of asperities come into contact by undergoing deformation to balance the normal load. The question to be answered is: At what loads do the asperities undergo permanent deformation during contact? Furthermore, how is the elastic limit related to the surface roughness of surfaces in contact?

One of the first statistical models of contact between rough surfaces is the one presented by Greenwood and Williamson [3]. This was followed by many later theories which have progressively done away with some of the simplifications made by them. In a model presented by Whitehouse and Archard [4], the mean contact pressure (P_{mean}) is given by the following expression:

$$P_{mean} = \frac{W}{A_r} = \frac{4\sigma E}{3n\pi(2.3\beta^*)} \frac{\int_d^\infty (z^* - d)^{3/2} \int_0^\infty \frac{f^*(z^*,C)}{C^{1/2}} dC dz^*}{\int_d^\infty (z^* - d) \int_0^\infty \frac{f^*(z^*,C)}{C} dC dz^*} \qquad (6.3)$$

Where

β^* :the correlation distance obtained from the exponential autocorrelation function of a surface profile

n : number of asperities per unit of apparent contact area

z^* :the normalized ordinate defined as $z^* = z/\sigma$

z : distance from the mean line

N : the ratio of peaks to ordinals. In this model N = 0.33

d : normalized separation between the datum planes of either surface , i.e. $d = h/\sigma$

h : the mean plane separation

C : dimensionless asperity curvature defined as $C = I^2/r\sigma$

I : sampling interval. In this model $I = 2.3\beta^*$

f^* : The probability density function of peak heights and curvature

Also the expressions for the RMS roughness (σ), effective elastic modulus (E), and the asperity radius (r) are as follows

$$\sigma = \sqrt{\frac{1}{L}\int_0^L z^2 dx} \tag{6.4}$$

$$\frac{1}{E} = \frac{1-\nu_1^{\ 0.5}}{E_1} + \frac{1-\nu_2^{\ 0.5}}{E_2} \tag{6.5}$$

$$r = \frac{2\pi^{½}\left(2.3\beta^*\right)^2}{9\sigma} \tag{6.6}$$

where E_1 and E_2 are the elastic moduli of the two solids in contact, while ν_1 and ν_2 are the corresponding Poisson's ratios.

The dependence of the mean contact pressure on material properties and the asperity geometry is clearly seen in eq. (6.3). Some characteristics such as the RMS roughness and asperity curvature are the most important of the shape determining parameters in the magnitude of contact pressure. Intuitively one would expect that if the surface is rougher and the asperities are sharper the contact pressure can be locally high, thus exceeding the elastic limit. The criterion for the transition from the elastic to plastic contact of rough surfaces with spherical asperities of radius r is defined by the plasticity index [3]. This index is defined based on the statistical nature of the surface topography and the contact mechanics as:

$$\psi = \frac{E}{H}\left(\frac{\sigma}{r}\right)^{½} \tag{6.7}$$

where H is the hardness of the softer material.

For values of ψ less than 0.6 elastic deformation is predicted to dominate. However, for values of ψ greater than 1 the model predicts plastic contact even at extremely light loads. When $0.6\langle\psi\langle 1$ the mode of deformation is unknown and can be elastic-plastic. Now suppose that the necessary RMS roughness of a steel surface (E_1=110 GPa, ν_1= 0.3) on a Bayhydrol 123 coating surface (E_2= 6.41 MPa, ν_2= 0.5, H= 6000 MPa) with an asperity radius of 10^{-9} m, is to be calculated to provide elastic contact. Using eq. (6.7) one can find that the RMS roughness of the contacting surfaces should be less that 1.5 nm. This is coincidentally the RMS roughness of the glass ball counterfaces used in the pin-on-disk experiments carried out in chapter 5. The roughness of the high-speed steel counterfaces used in this study is about 10 times higher.

6.4 Topography of Bearing Substrates

The silicon substrates used in chapter 5 were the smoothest available materials for the purpose of coating. The profilometry and AFM studies of silicon substrates and coated wafers showed that the coating tended to have approximately the same surface roughness as the substrate. In order to apply the concept of covalent solids to a shaft in bushing bearing, a mean roughness of few nanometers must be obtained from the bearing surfaces. Such low roughness, is difficult to achieve on any practical metallic bearing surface. The conventional methods of polishing or lapping metallic surfaces have limitations owing to the low hardness of metals compared to composites. The lowest RMS roughness that could be obtained with the shaft and bushings for this study was about 25 nm which is 10 times rougher than that of silicon substrate used in chapter 5. The surface profile and the roughness analysis of the bearing surfaces are shown in Figure 6.1.

In choosing the film thickness with respect to the roughness of the substrate there are two extreme cases. The first is when the coating thickness is much smaller than the height of the highest asperity of the substrate as shown in Figure 6.2a. This can result in early removal of the film by hard asperities of the counterface which in turn results in metallic contact of bearing surfaces. The second is when the film thickness is much greater than the size of any futures on the substrate as shown in Figure 6.2b. Although this case prevents metallic contact, one must be careful not to allow large hysteresis losses in a thick film, a problem that was addressed in chapter 5.

6.5 Boundary Conditions

The differences between the boundary conditions in a pin-on-disk experiment and a rotary sliding bearing arises from the topographical differences as well as the consequences of sliding in geometrically constrained systems. The geometrical differences causes different boundary conditions even at the onset of sliding due to the interaction of surfaces at a larger scale . As sliding progresses asperity deformation and formation of wear particles produces new boundary conditions. Wear particles were shown in chapters 1 through 4 to play a significant role in friction of geometrically constrained systems. The normal load can increase significantly from its initial value which causes a large frictional resistance of surfaces even if the friction coefficient has not increased noticeably. The entrapment of a wear particle agglomerate at a single contact point results in severe plastic deformation and damage to the sliding surfaces. Due to the geometrical constraints these wear particles cannot be removed from the

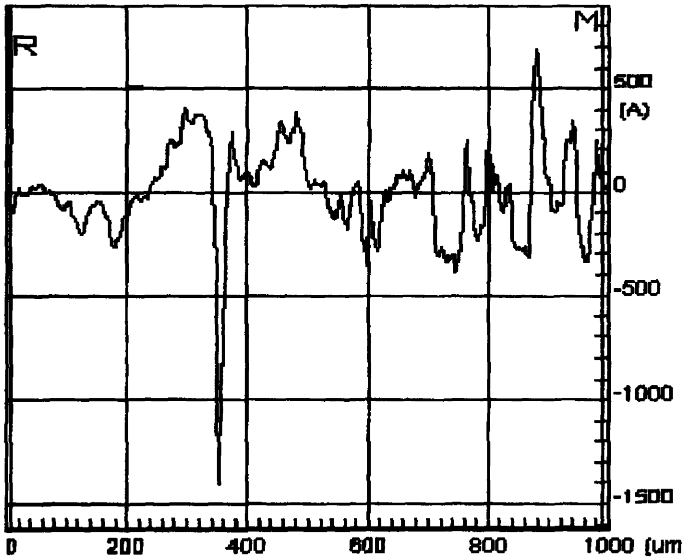

(a)

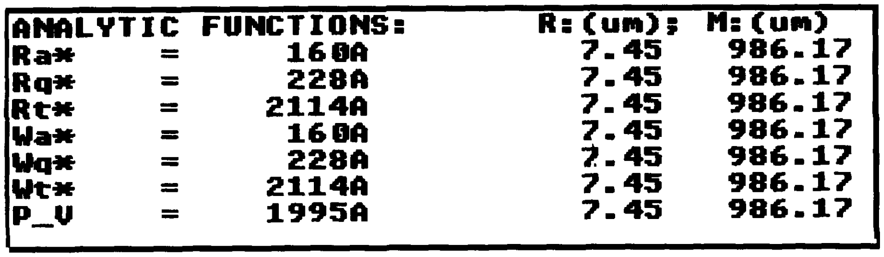

```
ANALYTIC FUNCTIONS:          R:(um);  M:(um)
Ra*      =        160A         7.45    986.17
Rq*      =        228A         7.45    986.17
Rt*      =       2114A         7.45    986.17
Wa*      =        160A         7.45    986.17
Wq*      =        228A         7.45    986.17
Wt*      =       2114A         7.45    986.17
P_V      =       1995A         7.45    986.17
```

(b)

Figure 6.1 Surface profile and roughness analysis of bearing surfaces before coating.

interface and the continuous shearing of particle agglomeration and plowing of the interface become the primary mechanism for energy loss.

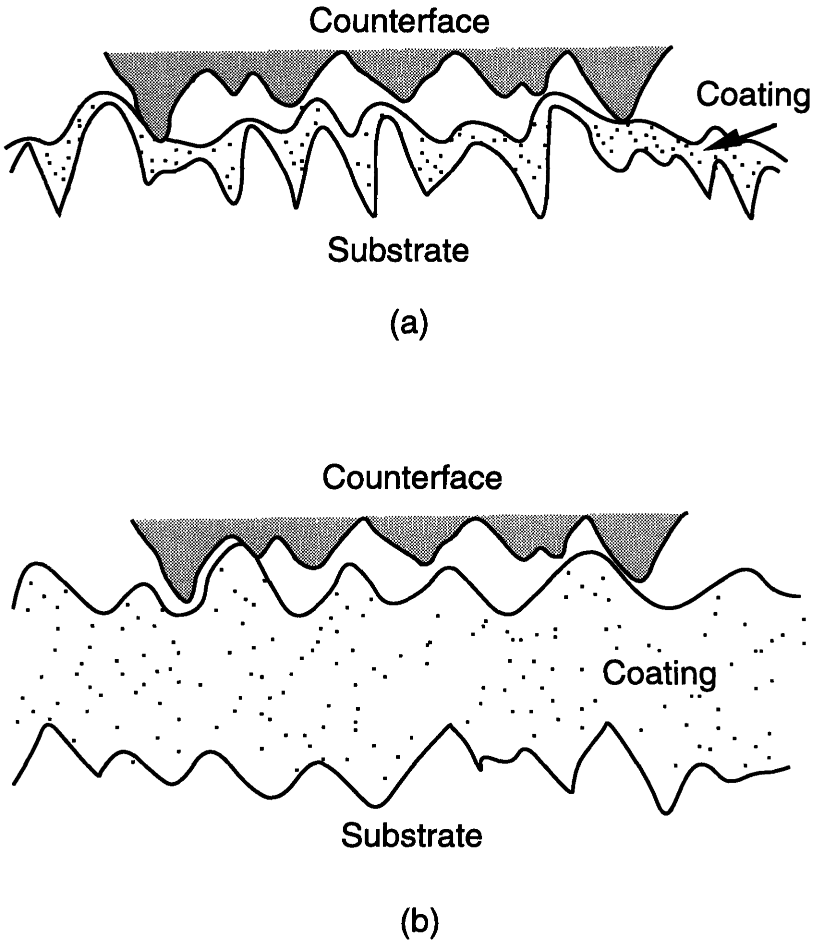

Figure 6.2 Illustration of dimensional comparison of the film thickness to the asperity height for a thin film (a) and a thick film (b) on the same substrate.

6.6 Experimental Set-up and Procedure

High-speed steel drill blanks were coated with Bayhydrol 123 and Bayhydrol 121 by the same coating procedure described in section 5.3. The film thickness was 0.12 μm for Bayhydrol 121 and 0.175 μm for Bayhydrol 123. The baking temperature and time were $140^\circ C$ and 15 minutes respectively. The coated shafts were then friction tested against bushings. The hardness of the shaft and the bushing was 45 R_c. The initial RMS roughness of both shafts and bushings was 0.5 μm. They were lapped to a RMS roughness of about 0.020-0.025 μm.

6.6.1 Friction Tester

A drawing of the friction tester used to carry out the experiments is shown in Figure 6.3a. Two pieces of acrylic were glued to the bushing as a mounting point for the weight and as an extended arm which was constrained from rotation by a load sensor. The resolution of the load cell was about 100 mg. The shaft was driven by a speed controlled motor at 60 rpm which corresponds to a linear speed of 2 cm/s.

Using the free body diagrams of the bushing shown in Figure 6.3b the equilibrium equations give:

$$\sum F_x = 0 \qquad N\sin\alpha - F\cos\alpha - T = 0 \tag{6.8a}$$

$$\sum F_y = 0 \qquad N\cos\alpha + F\sin\alpha - w = 0 \tag{6.8b}$$

$$\sum M_o = 0 \qquad Fr = Tb \tag{6.8c}$$

where W and T are the weight and the measured force by the load cell, while N and F are the total normal and frictional forces at a contact point which makes an angel of α with the y axis.

The contact angel α can found from

$$W\sin\alpha - T\cos\alpha = \frac{b}{r}T \tag{6.9}$$

and the normal load is:

$$N = W\cos\alpha + T\sin\alpha \tag{6.10}$$

The friction coefficient which is the ratio of the tangential load to the normal load will be:

$$\mu = \frac{F}{N} = \frac{(bT/r)}{W\cos\alpha + T\sin\alpha} \tag{6.11}$$

Using equation (6.9) one can find α by trial and error and substituting in equation (6.11) and knowing the values of T, W, and geometrical parameters the friction coefficient can be determined.

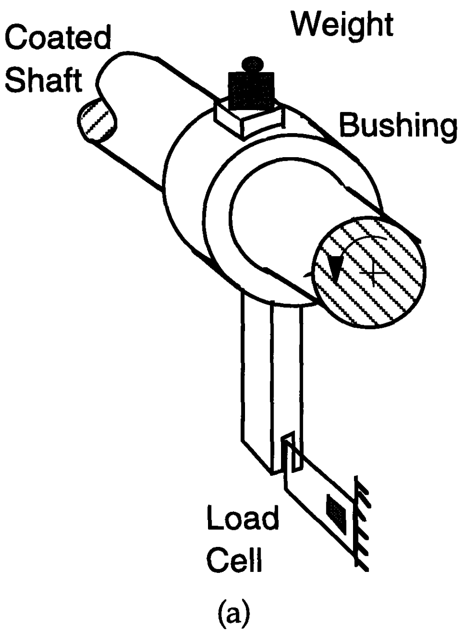

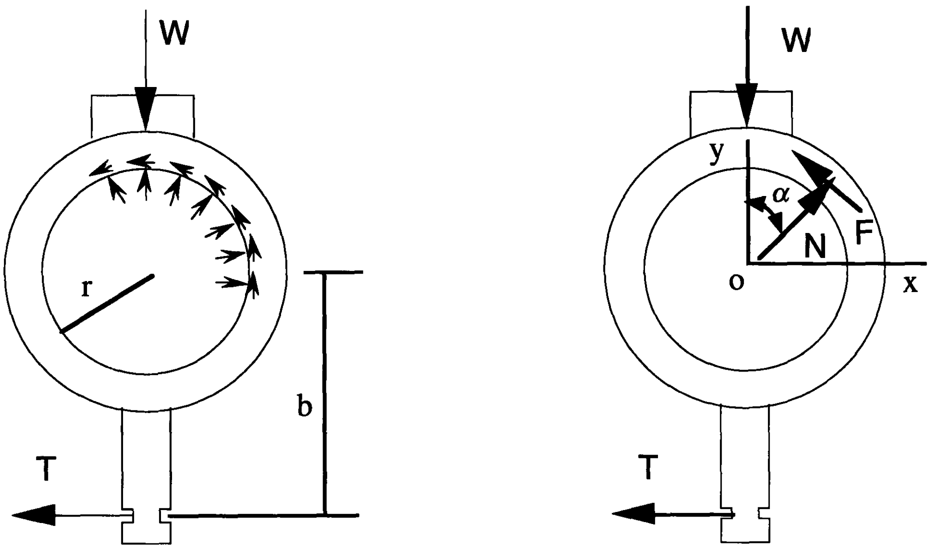

(b)

Figure 6.3 Friction tester (a) and the free body diagrams (b) of the bushing.

6.6.2 Results

The friction coefficient of high speed steel shaft and bushings sliding against each other is given in Figure 6.4. The steady state friction coefficient is about 0.35 after sliding for 12 m. Due to the relatively short sliding distance, the friction plot does not show a transition from the low initial value to a much higher value because the wear particles have not been extensively generated. This friction data are beneficial to understanding when the coefficient of friction of the coated bearings reach the steady state friction coefficient of uncoated specimens. This is due to the local removal of the film or plowing by the hard asperities of the counterface metallic contact which has occurred.

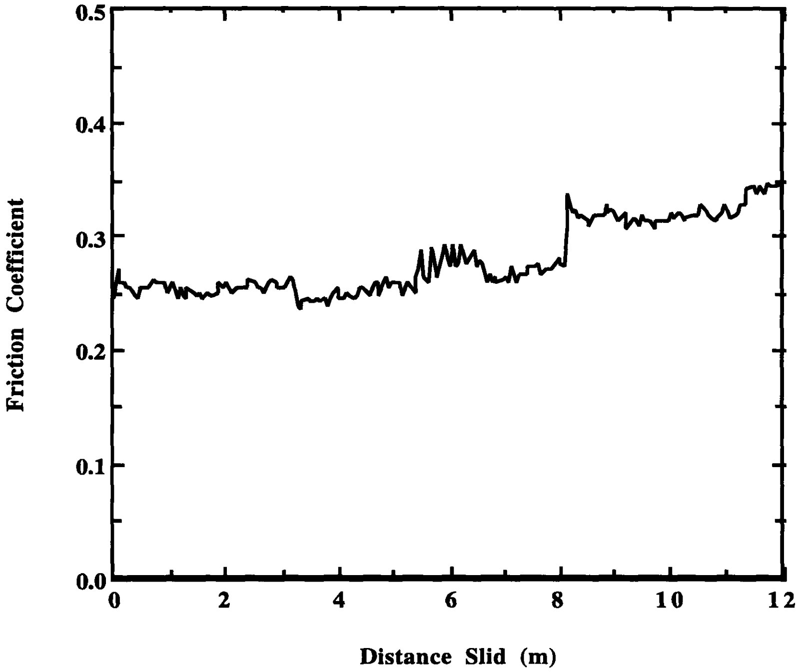

Figure 6.4 Friction coefficient of a high speed steel rod sliding against a high speed steel bushing. Normal Load= 10 g.

Shafts coated with a 0.175 μm films of Bayhydrol 123 were friction tested under two different normal loads and the results are shown in Figure 6.5. When the normal load was 5 g the friction coefficient started at a value of 0.085 and reached a steady state value of about 0.1. Under a 10 g normal load, however, a rapid transition from a low value of about 0.12 to a higher value of about 0.3 was observed. Severe damage and partial removal of the film could be seen on the surface of the shafts.

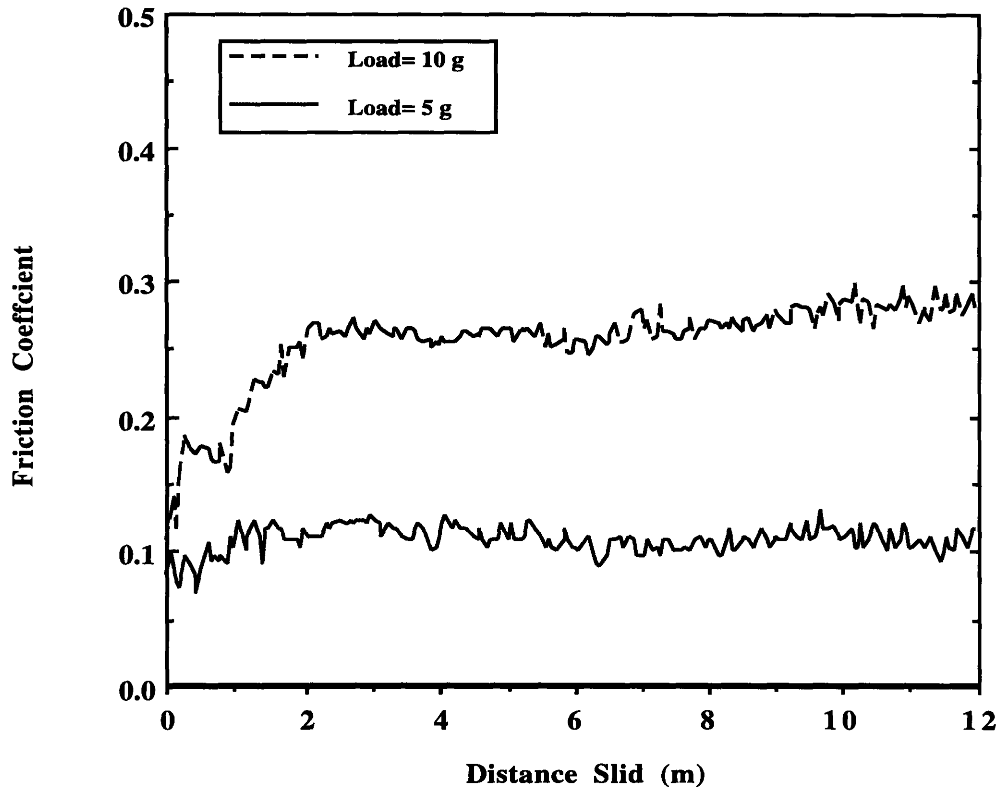

Fig. 6.5 Friction of a high speed steel shaft coated with a 0.175 μm thick Bayhydrol 123 film sliding against a high speed steel bushing.

After the test specimens coated with Bayhydrol 121 were also tested under 5 and 10 g normal loads. Again the friction coefficient under a 5g normal load stars at a low value of 0.075 and increases to a higher value of 0.15 (Figure 6.6). For a 10 g normal load the final value of friction coefficient after 10 m of sliding distance is about 0.32. Wear tracks on the film were clearly seen after the test with 10 g normal load.

Two significant observation could be made from the friction tests. First, the initial friction coefficients for most of tests were as low as those values obtained in pin-on-disk tests presented in chapter 5. However, as sliding proceeds, higher friction coefficients are reached which is the result of plowing of the film with the hard asperities of the counterface. Second, the damage to the film in all cases could be seen by the naked eye which is contrary to the observations made on pin-on-disk testing under optimal conditions.

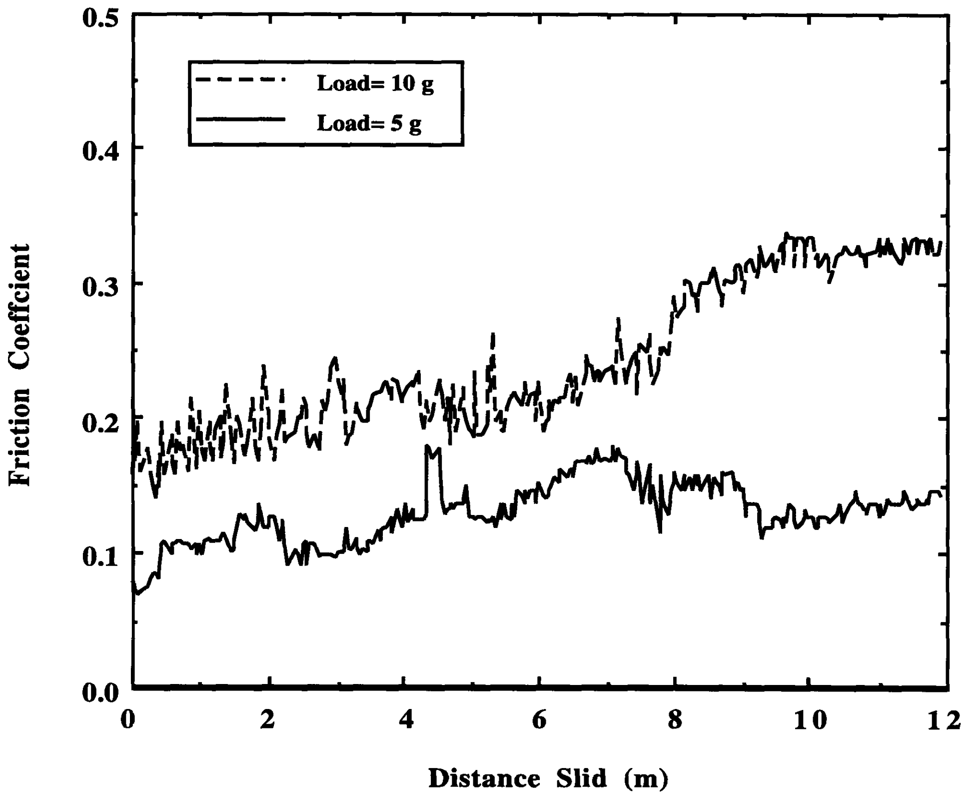

Figure 6.6 Friction of a high speed steel shaft coated with a 0.12 μm thick Bayhydrol 121 film sliding against a high speed steel bushing.

6.5 Conclusions

The attempt to apply the concept of covalent solids to practical bearings revealed the importance of geometrical and boundary conditions in sliding situations as well as the statistical characteristics of surfaces such as the asperity curvature and the surface roughness. The metallic surfaces used here were much rougher than the silicon wafers and glass balls used in chapter 5. This caused microscale plowing and tearing by hard asperities of counterface. Also when the normal load was high, partial removal of the film resulted in early metallic contact with a friction coefficient of about 0.35.

Low friction coefficients of about 0.07 at the onset of sliding followed with friction coefficients of about 0.1 are the promising results of this experimentation. These friction coefficients are low but not as low as what is experienced with pin-on-disk tests. Perhaps, among all differences between the surfaces studied here and the surfaces used in chapter 5, the surface roughness affects friction the most.

The local removal of polyurethane films during sliding in these experiments might raise a question about the strength of the substrate/film interface compared with that of polyurethane/silicon tested in chapter 5. The fact that steel has a higher surface energy than silicon ($\gamma_{steel} = 1500 \quad {}^{erg}/_{cm^2}$, $\gamma_{silicon} = 930 \quad {}^{erg}/_{cm^2}$) shows that the wetting of high speed steel surfaces by the polyurethane solutions ($\sigma_{solutions} = 0.1 \quad {}^{J}/_{m^2}$) was better [5]. Therefore, the strength of the substrate/film interface for steel/polyurethane composite must be higher than that of silicon/polyurethane.

References

[1] Suh, N.P., Mosleh, M., and Howard, P.S., "Control of Friction", Wear, To Appear, 1994.
[2] Archard, J.F., "Elastic deformation and the laws of friction", Proc. Roy. Soc., London, Series A, Vol. 327, 1957, pp. 190-205.
[3] Greenwood, J.A., and Williamson, J.B.P., "Contact of nominally flat surfaces", Proc. Roy. Soc., London, Series A, Vol. 295, 1966, pp. 300-319.
[4] Whitehouse, D.J., and Archard, "The properties of random surfaces of significance in their contact", Proc. Roy. Soc., London, Series A, Vol. 316, 1970, pp. 97-121.
[5] Cohen, E.D., Gutoff, E.B., "Modern Coating and Drying Technology", VCH Publishers, Inc., New York, NY, 1992.

Chapter 7

Conclusions and Recommendations

7.1 Conclusions

The reduction or elimination of mechanical components of friction through the design of surfaces has been investigated. The goal was to utilize the understanding of the dominant mechanism of friction in geometrically constrained systems in order to design and develop bearings for applications where dry sliding is unavoidable. Also, the functional requirements for low friction surfaces were identified and a model covalent solid was developed to minimize the mechanical interactions. For this case friction coefficients as low as 0.04 in dry sliding were obtained. The main conclusions of this thesis are outlined as follows corresponding to the chapters in which they were made.

> The geometrical constraints of a sliding system increase the possibility of entrapment of wear particles at the interface. The entrapped wear particles tend to grow under the compressive and shear forces at the interface and cause the externally loaded system to become internally loaded, whose internal loads depend on the history of sliding. In particular, the normal load in such systems will increase and even when the external loading is released the system will exhibit frictional resistance. The conventional definition of a friction coefficient will not be meaningful unless the real normal load is determined by considering the stiffness of the system constraints.
>
> A precision engineered sliding bearing can be designed with a surface profile having undulations that can remove wear particles from the surface soon after their formation. While such bearings provide high stiffness, in many engineering mechanisms no compromise on the

structural simplicity or the cost requirements needs to be made. Furthermore, friction coefficients as low as those obtained in the boundary lubrication conditions can be obtained in dry sliding of such bearings.

Mechanical aspects of friction such as plowing by wear particles and agglomeration increase in environments in which surface contamination such as physisorbed or chemisorbed films are partially removed or totally eliminated. However, in a high vacuum of 5×10^{-8} Torr, without an increase in temperature, there was no difference in the friction coefficient of bearing systems with large clearances which can be considered unconstrained systems. On the other hand, for extremely small diametral clearances this vacuum level caused seizure due to the compression of newly formed wear particles which clog up the bearing gap and increase the frictional resistance of the system. When the vacuum was accompanied with high temperatures of up to $300\,^{\circ}C$ the friction coefficient was increased to high values for large diametral clearances and led to early seizure of the sliding pairs.

Undulated surfaces operating in high vacuum and high temperature with small diametral clearances were able to prevent seizure but were not as effective as those tested in air in trapping wear particles. The surface of undulations examined with a scanning electron microscope showed extensive plowing damage as well as plastic deformation of undulations pads. This was related to the fact that wear particles in such environments tend to adhere to one of the sliding surfaces in contact and continue the action of plowing. Higher reactivity of a clean surface with wear particles due to the desorption of surface films and removal of oxide layer were the cause of such higher interfacial bonds. Also thermal softening of the metals at elevated temperatures is responsible for the plastic deformation of the undulation pads.

The hypothesis of developing covalent solids with a highly elastic surface layer and a high bulk hardness yielded promising ultra low friction coefficients almost half an order of magnitude less than that previously obtained in dry sliding with undulated surfaces or in boundary lubrication. These solids were created by coating extremely smooth substrates with an elastomeric film made from polyurethane dispersions. The combination of normal load and the thickness of the elastic layer were two important controlling factors on the frictional behavior of such materials. Experimental results suggested that for a given thickness, the friction coefficient plot shows an optimum at a certain load.

The crosslinking density of the surface layer of the model surfaces which is related to the mobility of the surface molecules was found to be the most important factor in minimizing damage during sliding. The atomic force microscope studies of the worn surfaces revealed that a higher friction coefficient was always accompanied by greater amounts of damage to the surface. However, plastic deformation of the surface layer at the nanoscale due to plowing or tearing was not completely avoidable even with a friction coefficient as low 0.04

The application of ultra-low friction surfaces to large area sliding bearings indicated that the surface roughness of the counterface is the most important surface parameter and should be well controlled. The experimental results indicated that plowing by the hard asperities is the dominant mechanism of friction and a friction coefficient of less than 0.1 with a counterface roughness of 20 nm was not achieved. The increase in the normal load caused localized removal of the film and the friction coefficient even at the very early cycles of sliding was high. Moreover, it was as high as that of the counterface sliding directly against uncoated substrate.

The durability of the surface film which depends on the interfacial surface energies of the film, the substrate, and on the plastic deformation of the surface layer in sliding dictates the duration of a low friction coefficient regime. Early removal of the film either due to plowing by hard asperities or tearing of the film causes direct contact between the counterface and the substrate resulting in a high friction regime and high wear.

7.2 Recommendation for Future Research

It has been demonstrated in this research that the surface engineering approach toward controlling friction can be effective and indeed provides alternative solutions to many engineering tribological problems. Design and development of undulated surfaces and bearings is an example of applying the basic knowledge of the role of wear particles at the sliding interface. Furthermore, utilizing the functional requirements for an ideal surface which led to the creation of a model covalent solid has been shown to reduce the destructive aspects of friction and provide ultra-low friction coefficient in pin-on-disk experiments. However, the attempt to create practical bearings with a friction coefficient less than 0.05 in dry sliding based on the findings of this research showed that more work is required in this area. Further research in this area can concentrate on understanding the correlation between the varying frictional behavior of surfaces at different scales and utilizing such understanding in design.

The microplowing of undulated surfaces is one of the reasons that the friction coefficient cannot be reduced less than 0.2 in dry sliding. The question: How can such plowing damage be prevented? can be answered only if the phenomenon of wear particle generation is well understood. The difference between undulated surfaces and smooth surfaces is in the removal of large wear particles from the interface by undulations. However, are the undulations able to remove the submicron wear particles from the interface as well? If not, do these small wear particles remain at the interface and do they cause any plowing? The fact that the pad of undulations used in this study had a width of about 200 μm supports the possibility of plowing of the interface by submicron particles which are produced at one edge of the undulations. Such particles have a distance travel of three order of magnitude longer than their size to plow. On the other hand, if the pad width is too small compared with the other dimensions of undulations such as their high or the groove width, then plastic deformation of the undulations may occur.

There may be many others designs which provide effective entrapment of submicron wear particles. Such designs may be able to offer the required strength to withstand buckling and/or plastic shearing. For instance, if the pads of the undulated surfaces which are typically about 200 μm wide have grooves a few micrometers wide, submicron wear particles may be trapped and still provide high structural strength. Another design may be to fill the undulation grooves with a soft material which allows the compaction of wear particles in them and prevents buckling or shearing of the undulations.

A very important issue concerning undulated surfaces is their manufacture. Design and development of new techniques other than the machining process used in this research is essential if such surfaces are expected to serve in practical bearings. Among the possibilities: chemical etching, photolithography, broaching, and forming. Also, there may exist surfaces which may have naturally occurring undulations.

In the design of covalent solids presented in this research, three important material parameters were considered: namely, elasticity of the surface layer, hardness of the bulk, and surface roughness. High elasticity of the surface layer allows large strains with relatively small or no amount of permanent deformation during which the bulk with a high hardness carries the normal load. Also, reducing the roughness results in low contact stresses at the asperity contact and prevents plastic deformation. However, there are many more issues for further work in this area. The optimization of sliding surfaces with respect to the elastic modulus of the surface layer is important. Also, the surfaces created in this study had a mean roughness of about 2 nm which could be reduced to the atomic scale limit. The dipping and drying techniques used in the coating of substrates in this research result in many defects on the film. Theses defects affect the surface roughness of the film and the interfacial bonds between the film and substrate which in turn affect friction. Furthermore, with these techniques the existence of airborne particles in the film is unavoidable and they were shown to be one possible cause of submicron scratches observed in the films after sliding. A coating technique such as an electrochemical deposition method might be considered as an alternative.

Understanding the structure of the elastomeric material used for the coating purposes and their crosslinking characteristic is essential for future research. The crosslinking density of the films was not measured directly but instead higher baking temperature and higher irradiation dosages were taken as indicators of higher crosslinking density. Since both hardness and toughness of elastomers can be controlled by crosslinking of molecules, the importance of understanding this material characteristic is enormous and will help in taking steps toward friction coefficients as low as 0.01 or less in dry sliding.

Appendix A

Analysis of the Hoop Strain in a Thin Asymmetrically Loaded Ring

Rings have long been used as displacement and force measurement devices in instrumentation and controls. The basic idea is to measure a certain load or displacement through the measurement of the hoop strain and calibration. In many instrumentation applications the rings are symmetrically loaded by a tensile or a compressive force and possibly a shear force which enables an easy calibration. However, when the loading is not symmetric the calculation of hoop strain is more complicated because of the existence of shear and normal stresses at any section of the ring.

Consider a ring which is supported on a pivot at the top and on a roller type of support at the bottom and is loaded by normal and shear forces as shown in Figure A1(a). Forces N_1 and F_1 are applied at a point which makes an angle of α with the y axis. At an angle of $\pi/2+\alpha$ from the y axis two other forces namely N_2 and F_2 are applied to the ring. Suppose that hoop strains at points A and B, shown in Figure A.1b, at angels of γ and $\pi/2+\gamma$ are to be determined.

In the deformed configuration each point on the ring has horizontal and vertical components of deflection as well as a rotation about an axial line through the center of the ring. The ring is constrained from horizontal and vertical deflections at the top support but it can have a rotation. At the bottom support only the horizontal component of deflection is constrained while the vertical deflection and the rotation are allowed. The internal normal force, shear force, and the bending moment at the bottom section are shown in Figure A.2a. Due to the rotation of top section. a horizontal deflection equal to $2R\beta$ will be experienced by the bottom section if it was not constrained horizontally (Figure A.2b).

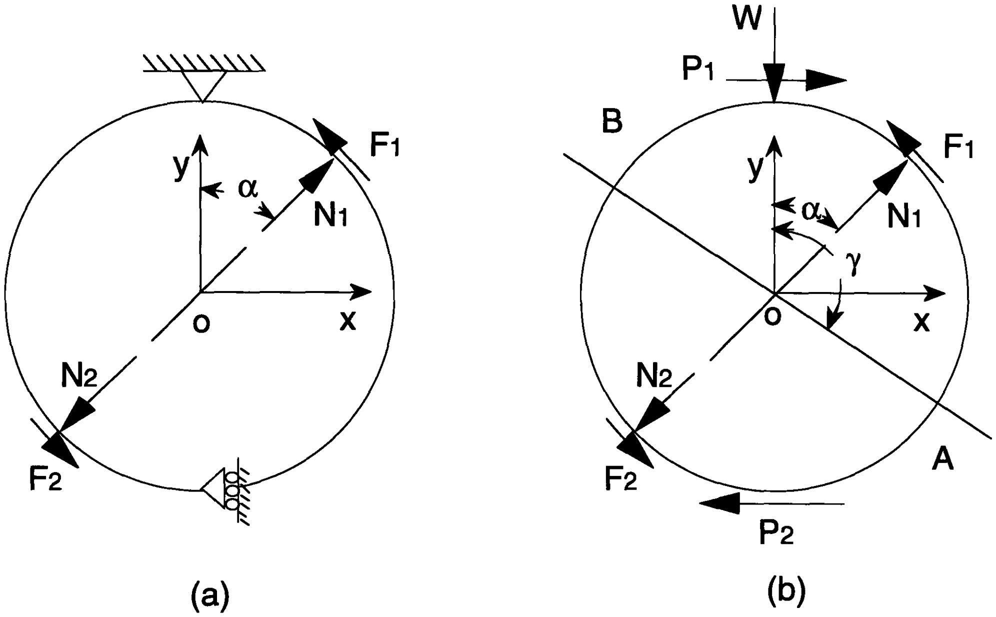

Figure A.1 Free body diagram of a ring showing the supports (a) and the external forces and reactions (b).

In order to calculate the hoop strains at a certain section, one must first determine the internal loads at the bottom section. This can be done using the energy method while applying the deflection and rotation compatibility conditions at the bottom section. The elastic bending energy (U) in each of the half rings is given by:

$$U = \frac{1}{2EI}\int_0^{\pi} M^2 R d\theta \tag{A.1}$$

Where E and I are the modulus and the second moment of inertia of the ring's cross section. To determine the generalized deflection at any point, one must take the derivative of the elastic energy with respect to a generalized load (L_i). This will give the generalized deflection in the direction of the applied generalized force. The generalized load can a force and the corresponding generalized deflection will be a displacement or it can be a moment and the corresponding generalized deflection will be a rotation.

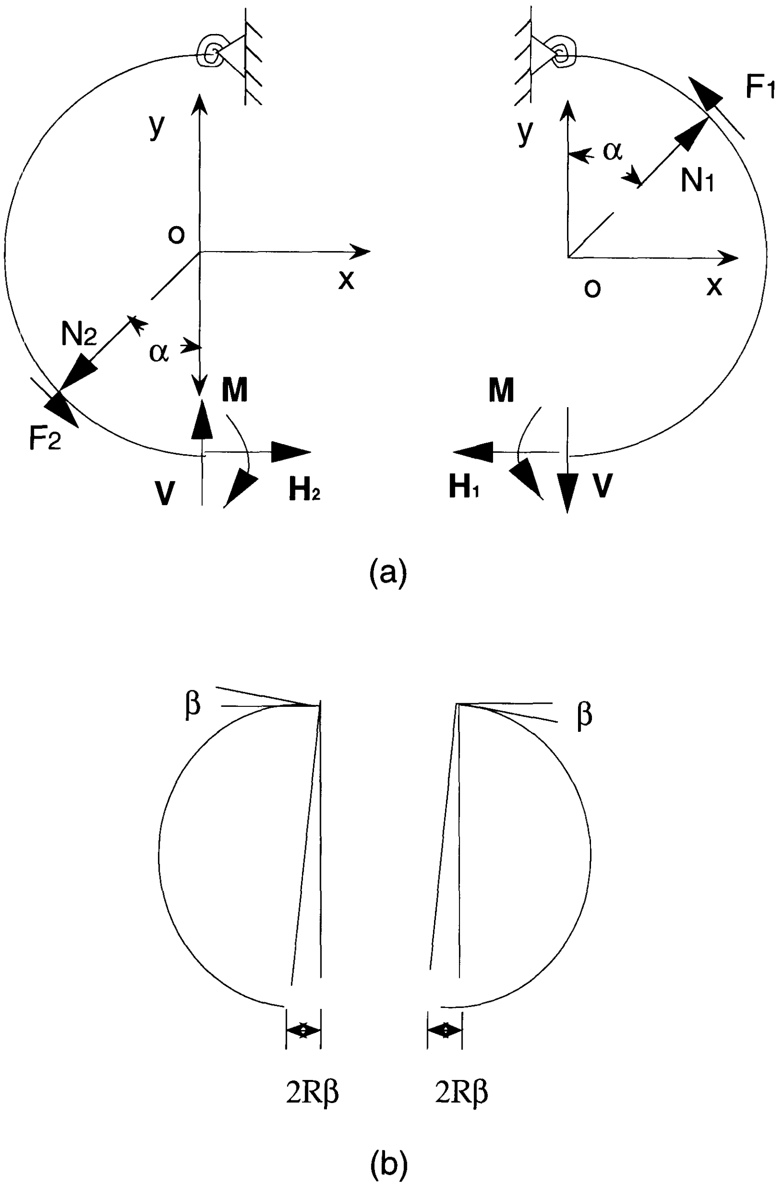

Figure A.2 Free body diagram of half rings with internal loads at the bottom section (a) and the horizontal deflection at the bottom due to the rotation of the top section (b).

Taking the partial derivative of the expression given in eq. (A.1) for the elastic bending energy gives

$$\frac{\partial U}{\partial L_i} = \frac{1}{EI}\int_0^{\pi} M \frac{\partial M}{\partial L_i} R d\theta \tag{A.2}$$

The moment M for the right half of the ring are:

$0\langle\theta\langle\pi-\alpha$

$$M = M_0 + VR\sin\theta - H_1R(1-\cos\theta) \tag{A.3a}$$

$\pi-\alpha\langle\theta\langle\pi$

$$M = M_0 + VR\sin\theta - H_1R(1-\cos\theta) - N_1R\sin(\theta+\alpha) + F_1R[1+\cos(\theta+\alpha)] \tag{A.3b}$$

and the partial derivatives of the moment M with respect to the loads at the section are:

$$\begin{aligned} &\frac{\partial M}{\partial M_0} = 1 \\ &\frac{\partial M}{\partial V} = R\sin\theta \\ &\frac{\partial M}{\partial H_1} = -R(1-\cos\theta) \end{aligned} \tag{A.4}$$

For the left half of the ring similar expressions for the moment M are:

$0\langle\theta\langle\alpha$

$$M = M_0 - VR\sin\theta - H_2R(1-\cos\theta) \tag{A.5a}$$

$\alpha\langle\theta\langle\pi$

$$M = M_0 - VR\sin\theta - H_2R(1-\cos\theta) + N_2R\sin(\theta-\alpha) - F_2R[1-\cos(\theta-\alpha)] \tag{A.5b}$$

with the partial derivatives of

$$\begin{aligned} &\frac{\partial M}{\partial M_0} = 1 \\ &\frac{\partial M}{\partial V} = -R\sin\theta \\ &\frac{\partial M}{\partial H_2} = -R(1-\cos\theta) \end{aligned} \tag{A.6}$$

The above expressions for the moment M and its derivatives can be substituted into eq. (A.2) to calculate the generalized deflections of the bottom section from the right and the left halves of the ring. The following boundary conditions must then be satisfied.

$$\phi_{right} = -\phi_{left} \qquad \left.\frac{\partial U}{\partial M_0}\right|_{right} = -\left.\frac{\partial U}{\partial M_0}\right|_{left} \tag{A.7a}$$

$$\delta_{x\,rightt} + 2\beta R = 0 \qquad \left.\frac{\partial U}{\partial H_1}\right|_{right} + 2\beta R = 0 \tag{A.7b}$$

$$\delta_{x\,left} - 2\beta R = 0 \qquad \left.\frac{\partial U}{\partial H_2}\right|_{left} - 2\beta R = 0 \tag{A.7c}$$

$$\delta_{y\,right} = -\delta_{y\,left} \qquad \left.\frac{\partial U}{\partial V}\right|_{right} = -\left.\frac{\partial U}{\partial V}\right|_{left} \tag{A.7d}$$

where ϕ is the rotation of the cross section while δ_x, and δ_y are the horizontal and the vertical deflections respectively.

The calculation of deflections and rotation of the bottom section with applying the boundary conditions stated in eqs. (A.7) will give the following linear set of equations.

$$\begin{aligned} 2M_0\pi - (H_1 + H_2)\pi R = {} & -N_1 R(1-\cos\alpha) - N_2 R(1+\cos\alpha) - F_1 R(\alpha - \sin\alpha) \\ & + F_2 R(\pi - \alpha - \sin\alpha) \end{aligned} \tag{A.8a}$$

$$\begin{aligned} -M_0\pi + \frac{3}{2}H_1\pi R - 2VR + \frac{2EI}{R}\beta = {} & N_1 R\left(1 - \cos\alpha + \frac{1}{2}\alpha\sin\alpha\right) \\ & - F_1 R\left(\frac{1}{2}\sin\alpha + \frac{1}{2}\alpha\cos\alpha - \alpha\right) \end{aligned} \tag{A.8b}$$

$$\begin{aligned} -M_0\pi + \frac{3}{2}H_2\pi R + 2VR - \frac{2EI}{R}\beta = {} & -N_2 R\left[\frac{1}{2}(\alpha - \pi)\sin\alpha - (1+\cos\alpha)\right] \\ & + F_2 R\left[\alpha - \pi + \frac{1}{2}\sin\alpha - \frac{1}{2}(\pi - \alpha)\cos\alpha\right] \end{aligned} \tag{A.8c}$$

$$\begin{aligned}2(H_2 - H_1)R + \pi VR = &-N_1R\left(\frac{1}{2}\sin\alpha - \frac{1}{2}\alpha\cos\alpha\right) - F_1R\left(1-\cos\alpha - \frac{1}{2}\alpha\sin\alpha\right)\\ &+ N_2R\left[\frac{1}{2}\sin\alpha + \frac{1}{2}(\pi-\alpha)\cos\alpha\right]\\ &- F_2R\left[(1+\cos\alpha) - \frac{1}{2}(\pi-\alpha)\sin\alpha\right]\end{aligned} \tag{A.8d}$$

Also from the free body diagram of an infinitesimal portion of the ring at the bottom shown in Figure A.3 one can write

$$H_1 = H_2 + P_2 \tag{A.9}$$

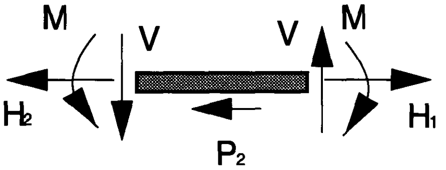

Figure A.3 Free body diagram of an infinitesimal section of the bottom of the ring.

Solving the above set of equations one can find the internal loads at section A can be found as:

$$\begin{aligned}M_0 &= \frac{1}{4\pi}(3C_1 + C_2)\\ RH_1 &= \frac{1}{4\pi}(C_1 + C_2) + \frac{1}{2}RP_2\\ RH_2 &= \frac{1}{4\pi}(C_1 + C_2) - \frac{1}{2}RP_2\\ RV &= \frac{1}{\pi}C_3\end{aligned} \tag{A.10}$$

where

$$C_1 = -N_1R(1-\cos\alpha) - N_2R(1+\cos\alpha) - F_1R(\alpha - \sin\alpha) + F_2R(\pi - \alpha - \sin\alpha) \tag{A.11a}$$

$$C_2 = N_1R\left(1-\cos\alpha+\frac{1}{2}\alpha\sin\alpha\right)-F_1R\left(\frac{1}{2}\sin\alpha+\frac{1}{2}\alpha\cos\alpha-\alpha\right)$$
$$-N_2R\left[\frac{1}{2}(\alpha-\pi)\sin\alpha-(1+\cos\alpha)\right] \tag{A.11b}$$
$$+F_2R\left[\alpha-\pi+\frac{1}{2}\sin\alpha-\frac{1}{2}(\pi-\alpha)\cos\alpha\right]$$

$$C_3 = -N_1R\left(\frac{1}{2}\sin\alpha-\frac{1}{2}\alpha\cos\alpha\right)-F_1R\left(1-\cos\alpha-\frac{1}{2}\alpha\sin\alpha\right)$$
$$+N_2R\left[\frac{1}{2}\sin\alpha+\frac{1}{2}(\pi-\alpha)\cos\alpha\right]-F_2R\left[(1+\cos\alpha)-\frac{1}{2}(\pi-\alpha)\sin\alpha\right] \tag{A.11c}$$
$$+2P_2R$$

Now the bending moments at point A and B can be determined by setting $\theta = \pi - \gamma$ in eq. (A.3a) and $\theta = \gamma$ in eq. (A.5b). A special case is when $\gamma = \pi/2$ which was the position that strain gages were installed in the experimental work carried out in chapter 3. The bending moments then can be expressed as:

$$M_{\gamma=90} = \frac{1}{2\pi}C_1+\frac{1}{\pi}C_3-\frac{1}{2}P_2R \tag{A.12a}$$

$$M_{\gamma=270} = \frac{1}{2\pi}C_1-\frac{1}{\pi}C_3+\frac{1}{2}P_2R+N_2R\cos\alpha-F_2R(1-\sin\alpha) \tag{A.12b}$$

The magnitude of the maximum bending strains at points A and B on the ring is related to the bending moments at the cross sections and can be given

$$\varepsilon_A = \frac{6M_A}{Ebt^2} \tag{A.13a}$$

$$\varepsilon_B = \frac{6M_B}{Ebt^2} \tag{A13.b}$$

where b and t are the width and the thickness of the cross section of the ring, while E is the modulus of the ring material.

Appendix B

Conventional Roughness Characterization

B.1 Roughness parameters

The roughness of a surface is often characterized by the average roughness, the root mean square roughness, and the pick to valley roughness. These parameters were automatically calculated when the DekTak 3000 profilometer was used for the surface roughness analysis. The average roughness (R_a), which is also known as CLA, is the arithmetic average deviation from the mean line. The root mean square roughness (R_q) defined as the standard deviation of the asperity height from the mean line.

$$R_a = \frac{1}{L}\int_0^L |z| dx \qquad \text{(B.1)}$$

$$R_q = \left(\frac{1}{L}\int_0^L z^2 dx\right)^{\frac{1}{2}} \qquad \text{(B.2)}$$

where z is the distance from the mean line and L is the characteristic length of the surface (Figure B.1). Also is the maximum pick to valley height of the asperity along the characteristic length L is defined as

$$R_t = R_p + R_v \qquad \text{(B.3)}$$

where R_p and R_v are the highest peak and the lowest depth of the profile roughness within the assessment length. as shown in Figure B.1.

Another parameter which is characterized as a step height parameter is the maximum peak to valley length. This parameter as shown in Fig. B1 is defined as the maximum vertical distance between a peak and a valley and shown as $P-V$.

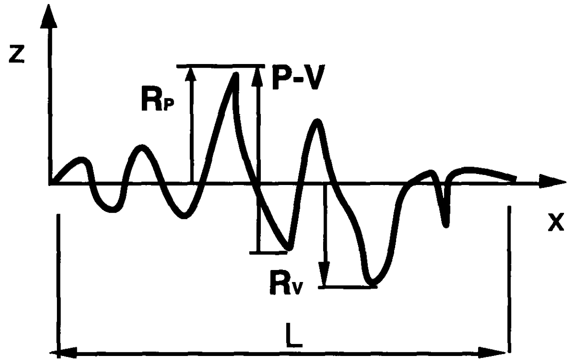

Figure B.1 Typical profile of a surface showing the roughness parameters.

B.2 Waviness parameters

In addition to small scale irregularities of a surface, i.e. roughness, periodic surface undulations are important features of a surface when the characteristic length is large. Waviness parameters are means to characterize such periodic waves. The arithmetic average of waviness (W_a) and the root mean square of waviness (W_q) are defined as:

$$W_a = \frac{1}{L^*}\int_0^L |v| dx \tag{B.3}$$

$$W_q = \left(\frac{1}{L^*}\int_0^L v^2 dx\right)^{\frac{1}{2}} \tag{B.4}$$

where v is the height of each point from the mean line and L^* is the characteristic length as shown in Figure B.2. Generally L^* is much larger than the characteristics length used for the roughness analysis. Similar to the peak to valley roughness, however, the maximum peak to valley of waviness is defined as:

$$W_t = W_p + W_v \tag{B.5}$$

where W_p and W_v are the maximum peak above the mean line and the maximum valley of waviness below the mean line within the assessment length.

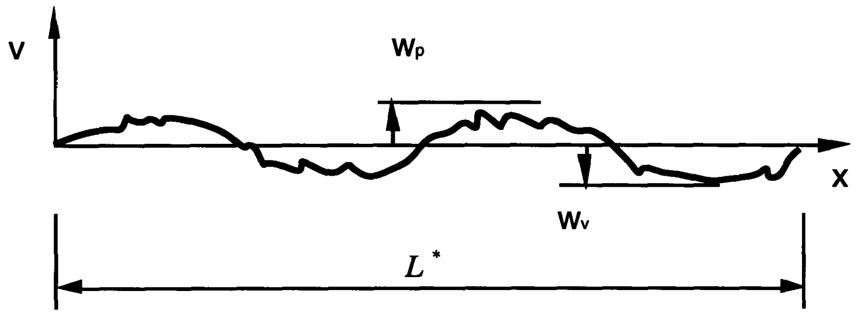

Figure B.2 Profile of a surface with a large characteristic length showing the periodic waves.